

Voxel-Based Iterative Registration Method using Phase Correlations for Three-Dimensional Cone-
Beam Computed Tomography Acquired Images

by

Nicholas Herbert Dietrich

A thesis submitted in partial fulfillment of the requirements for the degree of

Master of Science

Department of Mechanical Engineering
University of Alberta

© Nicholas Herbert Dietrich, 2016

Abstract

In orthodontics superimposition is an important technique allowing for accurate diagnosis and treatment planning. Lower radiation, three-dimensional, cone-beam computed tomography allows for acquisition of three-dimensional patient scans. New superimposition methods are used compared to the traditional methods used for two-dimensional scans. A new superimposition method is designed in this thesis.

A review of the current methods of superimposition used in orthodontics was performed. The review found that voxel-based, surface-based, and point-based superimposition methods are used. The most commonly used superimposition method is maximization of mutual information.

A cone-beam computed tomography machine is tested to find any inherent machine properties that may influence superimposition. The testing found that cone-beam computed tomography preserves and allows for highly accurate linear measurements. When greyscale values are viewed on a global scale there is not much change between scans. An issue arises when greyscale values are only viewed and compared between scans for a very small region of interest. Voxel-based superimposition methods must ensure they use a large enough region for the superimposition.

A full mathematical proof is contained within this thesis, outlining the techniques used in the superimposition method as well as the method itself. This includes proofs of the relevant techniques used, such as shift invariance for Fourier transform or finding the shift between two images using phase correlation. The algorithm works by taking two three-dimensional images and converting them to the frequency domain using Fourier

transforms. The Fourier transform removes the translation differences between the two images while preserving any differences due to rotation. The rotational changes are then converted to translations using a coordinate transform from Cartesian to cylindrical coordinates. The translational difference between the two volumes is found using phase correlation. This corresponds to a rotational shift between the two images about a single axis that can then be corrected. The entire process is then iterated through to correct for all rotational differences between the images. A final phase correlation allows for correction of all translations to fully register two images. A simple validation is included.

The algorithm is tested against patient scans. This is done in two manners, finding the registrations ability to register scans with known error, and registering time one and time two scans of real patient data with unknown initial error between the scans. The algorithm is also compared to the 6 point superimposition method found in literature. The new registration algorithm had comparable, or superior, accuracy in 4 out of 10 tests. The new algorithm had a 57% faster runtime compared to the six point method. The new registration algorithm required less user involvement than the six point method, only requiring a rough selection of the cranial base for each patient scan versus measuring multiple points accurately for the six point method.

Preface

This thesis is an original work by Nicholas Dietrich. The research project, of which this thesis is a part, received research ethics approval from the University of Alberta Research Ethics Board, “Analysis of Skeletal and Dental Changes obtained from a traditional Tooth-Borne Maxillary Expansion Appliance compared to the Damon system assessed through Digital Volumetric Imaging”, No. Pro00013379

*To my wife
for putting up with all the late nights*

Acknowledgements

I would like to thank my research supervisors for all of their help with the production of this Thesis over the length of my degree. My supervisors Dr. Jason Carey, Dr. Manuel Lagravère, and Dr. Marc Secanell provided much needed support and guidance. They were always able to steer me in the right direction and keep my research on track and moving forward. Available to answer questions at any time, and always willing lend a helping hand, their combined experience was an invaluable asset.

I would also like to thank my parents and my loving wife for all of their support and help over the previous years.

Author

Nicholas Dietrich

CONTENTS

1	Introduction.....	1
1.1	Motivation.....	1
1.2	Thesis Objectives.....	3
1.3	Thesis Scope.....	3
1.4	Thesis Outline.....	4
1.5	References.....	5
2	Methods of Superimposition for Orthodontic Images: A Review	7
2.1	Introduction.....	7
2.2	Materials and Methods	9
2.3	Results	10
2.3.1	Voxel-Based Methods.....	14
2.3.2	Surface-Based Methods.....	17
2.3.3	Point-Based Methods.....	18
2.4	Discussion.....	19
2.5	Conclusion.....	21
2.6	References.....	23
3	Assessment of CBCT Imaging Capabilities on Superimposition and Registration Techniques 27	
3.1	Introduction.....	27
3.2	Materials and Methods	29
3.3	Results	37
3.3.1	Method 1- Distance Measurements	37
3.3.2	Method 2 – Global Voxel Greyscale Measurement.....	38

3.3.3	Method 3 – Local Voxel Greyscale Measurement	40
3.4	Discussion.....	42
3.4.1	Distance Measurements	42
3.4.2	Global Greyscale Measurements	44
3.4.3	Local Greyscale Values	45
3.5	Conclusion.....	48
3.6	References.....	49
4	Development of a registration algorithm for 3D CBCT image superimposition.....	53
4.1	The Fourier Transform	54
4.1.1	Fourier Transform Composition	55
4.1.2	Fourier Transform Definition	57
4.2	Properties and Techniques Using Fourier Transforms	58
4.2.1	Translational Invariance	58
4.2.2	Rotation Preservation.....	61
4.2.3	Phase Correlation Method for Comparing Two Images.....	62
4.3	Registration Implementation	65
4.3.1	Fourier Transform of 3D Volumes	69
4.3.2	Conversion to Cylindrical Space	69
4.3.3	Phase Correlation.....	71
4.3.4	Compensate for Rotation	72
4.3.5	Repetition of the Rotations	72
4.3.6	Phase correlation to find Translation Differences	72
4.3.7	Apply Translation Matrix to g	73
4.4	Techniques for Improving Phase Correlation.....	73

4.4.1	Filtering.....	73
4.4.2	Windowing	76
4.4.3	Thresholding.....	79
4.5	Registration Validation using a Standard Shape.....	80
4.5.1	Gold-Standard and the image to be registered.....	80
4.5.2	The 1 st iteration	82
4.5.3	The 2 nd iteration	85
4.5.4	Third iteration and Translation correction	87
4.6	Conclusion	88
4.7	References.....	89
5	Assessment of Superimpositon Algorithm: Patient Case Studies.....	90
5.1	Introduction.....	90
5.2	Materials and Methods	91
5.2.1	Finding the Optimal Parameters	92
5.2.2	Testing on Patient Scans: Introduction of Random Error.....	93
5.2.3	Registering T1 and T2 Patient Data.....	94
5.3	Results	96
5.3.1	Optimal Registration Parameters	96
5.3.2	Testing on Cranial Bases with Known Error	99
5.3.3	Registration of Patient T1 and T2 Data	100
5.4	Discussion.....	116
5.4.1	Testing on Cranial Bases with Known Error	116
5.4.2	Testing on Patient T1 and T2 Data	117
5.5	Conclusion	120

5.6	References.....	121
6	Conclusions and Future Work	123
6.1	Conclusion.....	123
6.2	Future Work.....	124

List of Figures

Figure 2-1. The Venn diagram shows the search terms that are used in the PubMed database. The intersection of the circles coloured black is the successful search results. The * operator, known as a wildcard, allows for Three and Dimensional to separate with either a space or dash..... 9

Figure 2-2. Flow chart showing the process of assessing publications for the review 11

Figure 2-3. A simple image is shown in A, the simple image is then translated a small amount in B. C shows the two images overlapped with the original image A appearing green and the shifted image appearing pink. The area bordered in red is where the green image has voxel value of 160 and the pink image has voxel value of 100. 450 voxels fall within this square meaning that pixel (160,100), marked by an arrow, in the feature space image D has a value of 450. 16

Figure 3-1: Dry skull placed within container with water compartment to simulate tissue in the iCAT machine..... 30

Figure 3-2: Locations landmarked to test for repeatability of linear measurements. All days used the same landmarks, the right temporal screw tip and the tip of the screw for attaching the cranial dome. 32

Figure 3-3: a) Close-up view of the left Foramen Ovale within the dry skull's cranial base. b) Close-up view of the Right Foramen Ovale. The circles show the pointed tip being used for landmark placement..... 33

Figure 3-4: a) Axial view of the skull dry skull, the section of cranial base within the sphere is shown opaque b) Sagittal view of the skull with the bone within the sphere shown as opaque..... 34

Figure 3-5: Left 3rd molar showing the 125 voxel cube used for computing location greyscale average. The three views are a) Axial plane, b) Sagittal plane, c) Coronal plane. The same voxel is the center of the black box in all 3 views. 36

Figure 3-6: Boxplot of linear distances for each day, notches represent the 95% confidence interval for each day; + represent outliers greater than ± 1.5 IQR from the upper or lower quartile, respectively. Dotted lines represent the data max/min and average values. 37

Figure 3-7: Greyscale average of a sphere of 3cm radius centered on the midpoint of the left and right foramen ovale. Tapered regions represent the 95% confidence interval for each day; + represent outliers greater than ± 1.5 IQR from the upper or lower quartile, respectively. Dotted lines represent the data max/min and average values..... 38

Figure 3-8: Greyscale average values of 125 voxel-cube of left third molar, left canine, right canine, right third molar dentin for each day. All teeth are in maxillary arch. Dotted lines represent max/min and average values whiles + represent outliers greater than ± 1.5 IQR from the upper or lower quartile, respectively..... 41

Figure 3-9: The anterior clinoid process (outlined in black) is the tips of bone that is raised above the rest of the cranial base. These pieces of bone are likely to small to be used as the only ROI in a greyscale based superimposition. 47

Figure 4-1. This composite shows a periodic signal in the time domain (a) being represented as a sum of trigonometric functions (b) in order to convert the image to the frequency domain (d). This means that sub-figure a and d are actually the same signal just represented in the spatial versus frequency domain. Adapted from [1]. 54

Figure 4-2. Frequency plot resulting from a Fourier transform on the signal in Figure 4-1a. Only the positive frequency is shown. Note that the plot is continuous..... 55

Figure 4-3. (A) Original image, (B) magnitude information, and (C) phase information. The frequency range of an axis is from $-N/2$ to $N/2$ where N is the size of the images axis. 56

Figure 4-4. The Fourier transform of an image compared to Fourier transform of same image with translation. A2 is the Fourier transform of A1, likewise for B. A2 and B2 are identical. 60

Figure 4-5. Since sub-figure A is rotated CCW by 20° the Fourier transform of the image is also rotated CCW by 20° 62

Figure 4-6. (A) “Gold-standard” image, images (B) and (C) are ideal candidates for phase correlation registration. The cropping of an image does not affect phase correlation as long as it fits uniquely in the “gold standard” image. 62

Figure 4-7. Sub-figure A and B are identical except for a shifting of -200 pixels in sub-figure B. Figure C is a zoomed in view of the resulting cross correlation produced using equation 23. The

white dot corresponds to location (201,201) meaning sub-figure B lags (is behind) sub-figure A by 200 pixels in each direction. Note the location is (201,201) since the cross correlation was produced using Matlab which indexes from 1, i.e. a location of (1, 1) would mean a shift of 0 pixels in both dimensions). In sub-figures A and B the upper left corner of the image is the origin, in sub-figure C the upper left corner is location (175,175) and the lower right corner is location (225,225). 65

Figure 4-8. Superimposition of the cylindrical coordinate system over the Cartesian coordinate system. The z-axis is the same for both coordinate systems. Adapted from [7]..... 70

Figure 4-9. The top set of images are the Cartesian (left) and polar representation of the same image (x-axis represents phi and y-axis represents rho). The image is then rotated in the spatial domain 45°, resulting in a translation in the cylindrical representation (phi axis shift). The red line shows the shift between the images. 71

Figure 4-10. The top images are the results of running a(n) (in order left to right): no filter (A), ideal low-pass filter (B), ideal high-pass filter (C), and ideal band-pass filter (D). The bottom image is the corresponding magnitude of the Fourier Transform for each image. There are ringing artifacts visible in C and D around the high frequency areas. 74

Figure 4-11. Image A is the Gaussian high-pass filtered of the original image in Figure 4-9. Notice that the ringing artifacts (appearing as halos) around the high frequency sections of the image are removed. Image B is the Gaussian filtered Fourier transform. The center bright dot has been removed without causing a large section of the image center being reduced to 0..... 75

Figure 4-12. This figure shows the change in the response of the Gaussian high-pass filter with changing σ value. The sigma values (A) 20, (B) 50, and (C) 100. 76

Figure 4-13. The periodic nature of the Fourier transform means the edges of the image are assumed to lead into the next image. 77

Figure 4-14. The periodic nature of the Fourier transform means the edges of the image are assumed to lead into the next image. A windowing function changes the edges of the image so that discontinuities do not occur at the image edges. Image A is an ideal window with the image edges converted to black and image B is the cranial base image with a hamming window. 78

Figure 4-15. The Otsu thresholding method was able to separate the light and dark material pixels in the original image (A) to create thresholded image (B). 79

Figure 4-16. The red volume is the gold standard and the blue volume is the volume to be registered. The amount of error is given in Table 4-1	81
Figure 4-17. The blue volume has undergone a rotation about the z-axis of 5.76° after the first rotation of the first iteration.	82
Figure 4-18. The blue volume has now undergone a rotation in the y axis of 15.84° . It may appear that the rotation is causing increasing error and this is correct. This optimization will sometimes increase the error and it will then be corrected for with the next iteration.	83
Figure 4-19. The blue volume has now undergone a 11.52° rotation in the x axis. With this rotation the first iteration of the algorithm has been completed.....	84
Figure 4-20. The rotation about the z-axis for the second iteration is -2.88°	85
Figure 4-21. The x-axis rotation for the second iteration is -21.6° . This rotation bring the volumes into rotational alignment.	86
Figure 4-22. The fully corrected volumes are shown. The red and blue volumes are overlapped to be nearly indistinguishable.	87
Figure 5-1. View of the transverse plane of cranial base from patient #1, used to find the parameters of the registration algorithm. The view is looking in the inferior direction with the anterior direction being towards the bottom of the page.....	92
Figure 5-2 View of the transverse plane of cranial base from patient #2, used to find the parameters of the registration algorithm. The view is looking in the inferior direction with the anterior direction being towards the bottom of the page.....	93
Figure 5-3. Figures A, B, and C are the remaining cranial bases from patients #3, #4 and #5, respectively.....	94
Figure 5-4. (A) An anterior view of the images to be registered. (B) A Superior view of the images to be registered. The red image is registered into the gray image. The gray image is T1 and the red image is T2. The reason the T2 image appears smaller in Figure 5-4B is due to perspective as it is located farther into the page in the global coordinate system.....	95

Figure 5-5. The L2-norm values of each of the cranial base tests, excluding tests that involved thresholding. Figure 5-5B has the results for sigma values of 1 and 21 removed. Windowing on means the hamming window is applied to the cranial base during registration, windowing off means the hamming window is not applied during the registration process. 98

Figure 5-6. The normalized L2-norm results of the cranial base test sets. Each test set consists of 10 trials. The data is normalized with respect to the largest L2-norm value found using the Monte Carlo Analysis. The * shows there was an outlier resulting from non-ideal convergence, resulting in a normalized L2 Error greater than 2. Test set 1 had 1 outlier, while test set 4 had 2 outliers..... 100

Figure 5-7 Histogram showing the L2-Norm error in registration for the patient 1 time 1 and time 2 scans using the 6-point registration method and the new method. 102

Figure 5-8 Histogram showing the L2-Norm error in registration for the patient 2 time 1 and time 2 scans using the 6-point registration method and the new method. 103

Figure 5-9 Histogram showing the L2-Norm error in registration for the patient 3 time 1 and time 2 scans using the 6-point registration method and the new method. 104

Figure 5-10 Histogram showing the L2-Norm error in registration for the patient 4 time 1 and time 2 scans using the 6-point registration method and the new method. 105

Figure 5-11 Histogram showing the L2-Norm error in registration for the patient 5 time 1 and time 2 scans using the 6-point registration method and the new method. 106

Figure 5-12 Histogram showing the L2-Norm error in registration for the patient 6 time 1 and time 2 scans using the 6-point registration method and the new method. 107

Figure 5-13 Histogram showing the L2-Norm error in registration for the patient 7 time 1 and time 2 scans using the 6-point registration method and the new method. 108

Figure 5-14 Histogram showing the L2-Norm error in registration for the patient 8 time 1 and time 2 scans using the 6-point registration method and the new method. 109

Figure 5-15 Histogram showing the L2-Norm error in registration for the patient 9 time 1 and time 2 scans using the 6-point registration method and the new method. 110

Figure 5-16 Histogram showing the L2-Norm error in registration for the patient 10 time 1 and time 2 scans using the 6-point registration method and the new method. 111

Figure 5-17. The cranial base from T2 (red) was successfully aligned with the cranial base (grey) from T1. 112

Figure 5-18. A superior view of the registration. The cranial bases have a small error in registration that is visible in this view as a rotation (imposed black lines). 113

Figure 5-19. The registration is shown on the full patient scans. This scan is thresholded to identify changes in the facial proportions. 114

Figure 5-20. The registration is shown on the full patient scans. This scan is thresholded to identify changes in the position and skull changes as a result of growth. 115

List of Tables

Table 2-1. Studies included in the literature review. Any specific software that is used is stated. . .	12
Table 2-2. Simplified comparison of the current techniques used in orthodontics.....	21
Table 3-1 Standard deviation (SD) and descriptive metrics of sphere averages for each day.....	39
Table 3-2: Mean and standard deviation (SD) of each tooth scan for each day. The largest change within a single day for each tooth is also shown. All values are in greyscale units. All teeth are in maxillary arch.....	40
Table 3-3: Comparison of tooth greyscale values for within days and comparing days. The largest change between days and statistically significant P values are bolded.	41
Table 4-1. The initial error in rotation and translation between the gold-standard and registering image.	80
Table 5-1. L2-norm values of parametric test for cranial base one, the settings are the strength of the Gaussian filter (σ), windowing being turned on or off and thresholding being turned on or off	97
Table 5-2. L2-norm values of parametric test for cranial base two, the settings are the strength of the Gaussian filter (σ), windowing being turned on or off and thresholding being turned on or off	97
Table 5-3. The maximum and median values of the Monte Carlo analysis for the 5 cranial bases images. The normalized median is normalized with respect to the corresponding Monte Carlo maximum. The Monte Carlo Maximum becomes the max allowable error for future tests using the corresponding cranial base model.....	99
Table 5-4. The median L2-norms of the registered images are used to compare between the new method and the six-point method. The bolded value is the lower of the two methods for the scan. If both values are bolded the results are within 10%.....	101
Table 5-5. Comparison of the 6-point registration and the new registration algorithm.....	119

List of Abbreviations

2D	Two-Dimensional
3D	Three-Dimensional
CBCT	Cone-Beam Computed Tomography
CT	Computed Tomography
DICOM	Digital Imaging and Communications in Medicine
FFT or fft	Fast Fourier Transform
FOV	Field of View
FT	Fourier Transform
ICP	Iterative Closest Point
IQR	Inter-quartile Range
kV	Kilovolts
mA	Milliamps
mm	Millimetre
MMI	Maximization of Mutual Information
RAM	Random Access Memory
ROI	Region of Interest
T1	Time One
T2	Time Two

1 INTRODUCTION

1.1 MOTIVATION

Proper dental care has become an integral part of Canadian society. In 2009, almost 13 billion dollars were spent on dental care within Canada [1]. In 2010, it was reported that almost 20% of Canadians currently receive or have received orthodontic treatment, with 18% of adolescents currently receiving treatment [1]. In order to assess individual patient needs when creating treatment plans, x-rays are commonly used in orthodontic clinics. With the increasing usage of orthodontics treatment more advanced x-ray equipment is coming into use in Canada. One such device is Cone-Beam Computed Tomography (CBCT). CBCT allows for orthodontists to acquire volumetric data, similar to a medical CT. This allows orthodontists to overcome the innate problems of 2D x-ray scans, mainly image magnification, patient positioning, and measurement error [2], [3]. A 3D scan allows orthodontists to overcome some of these problems by offering 1-to-1 scaled images that can have measurements taken in all planes. Three dimensional (3D) imaging also allows for more information to be gathered all three anatomical planes (axial, sagittal, coronal) can be recreated from one CBCT scan [4]. Switching to 3D x-ray scans from traditional 2D scans may increase radiation. However, recent advances in CBCT has lowered the radiation dosage but affected the quality of the images, though still good enough quality for many clinical purposes, images with radiation dosage comparable to 2D panoramic X-ray scans [5]. Many authors consider the introduction of CBCT for craniofacial imaging to be a large change with far reaching consequences [6]–[8].

One technique that uses the x-rays acquired in the orthodontic clinic is superimposition. Superimposition means to overlap the before, during, and after treatment scans in order to assess changes with treatment and growth. This allows the orthodontist to make better informed decisions, including changes to the treatment plan. An issue that has arisen with the advent of 3D medical imaging for maxillofacial imaging is that new techniques are needed for full analysis of the 3D data.

In 2D, cephalometric measurements and comparisons between scans are done by projecting the three dimensional skull onto a two dimensional plane [3]. 3D scans do not have these projections and different methods must be used for image superimposition and measurement. Research in recent years has studied the use of superimposition based off of foramen in the human skull, which present themselves as holes in the skull through which veins, arteries, and nerves travel [9]. Though this method is functional, it is not as reliable in finding effectiveness of treatment between a reference time (normally start of treatment), time 1 (T1) and a later time when treatment effectiveness is being determined time 2 (T2) due to both a mixture of patient growth and clinician error in selecting landmarks. In orthodontics a tooth movement of only a single millimeter may be clinically significant. For some commonly used landmarks, inter-examiner error may be a millimetre or greater [9], [10]. With clinician landmark placement error being potentially as large as the tooth movement needed this can lead to erroneous treatment prognosis and effectiveness.

Current problems with 3D superimposition relate too many of the issues known in medical superimposition (or registration). Issues include time required for superimposition, user input to the scan, in terms of time required and expertise required, and accuracy of the final superimposition. All of these factors must be balanced in creating an easily accepted superimposition technique. If a superimposition technique is slow it will see limited use in the fast pace of a clinic, where the clinician has to interpret changes and make treatment decisions in a single patient visit. If the method is not accurate enough it will not be useful for quantifying changes within the patient's bone structures, and if the method is not user friendly it will not be adopted by orthodontists who wish to use it as a tool to enhance their practice. If all the requirements can be balanced however the ability to superimpose 3D maxillofacial images in an orthodontic clinic will increase the ability of the orthodontist to diagnose, give prognosis, and develop patient treatment plans. Even with the difficulty of 3D superimposition it is still a highly desirable technique.

1.2 THESIS OBJECTIVES

The objective of this thesis is to design a new technique of superimposing (registering) two 3D scans taken at different times acquired using a CBCT device. An automated method of superimposing T1 and T2 images will allow for easy quantification of patient tooth and jaw changes without clinician landmarking error and bias. The image quality and modality of CBCT will be tested and taken into account during this process. The technique developed should work for any volumetric data acquired using CBCT regardless of the CBCT machine used. The method will be tested using previously acquired patient data.

1.3 THESIS SCOPE

The scope of this thesis is limited to 2 elements:

- A) Develop and assess a superimposition technique, including testing a CBCT machine to investigate its imaging capabilities.
- B) Assess technique using an artificial system as well as real patient data.

Factors that will affect the success of the superimposition technique will be:

1. Accuracy of the superimposition. If superimposition is not accurate the orthodontist will not be able to measure the changes in tooth movement accurately. This will increase the difficulty of treatment planning.
2. Time required to superimpose two scans. After an orthodontist in a clinic takes a patient scan they will often have limited time to perform the superimposition and quantify changes before needing to make decisions regarding a patient's treatment.
3. Researcher and clinician involvement. If a technique requires multiple steps or has a steep learning curve it will not be as easily adopted into an orthodontic clinic.

1.4 THESIS OUTLINE

This thesis is divided into 6 chapters and 2 appendices. In Chapter 2, a critical literature review of the current superimposition methods used clinically in orthodontics is presented. In Chapter 3, testing of a CBCT machine is performed to determine which inherent machine properties will influence superimposition techniques. The new superimposition method is introduced in Chapter 4; a thorough mathematical proof of the method is given. Testing of the superimposition method on actual patient data and the quantification of test results are shown in Chapter 5. Finally, in Chapter 6 general conclusions and future work are provided.

The two appendices are separated as follows. Appendix A contains supplementary results from testing the superimposition method on patient data. Appendix B contains code for the method using the Matlab programming language.

1.5 REFERENCES

- [1] Canadian Dental, “Dental Health Services in Canada. Facts and Figures 2010.,” 2010.
- [2] H. S. Duterloo and P.-G. Planche, *Handbook of Cephalometric Superimposition*. Hanover Park, IL: Quintessence Publishing Co., 2011.
- [3] J. L. Prince and J. M. Links, *Medical Imaging Signals and Systems*, 2nd ed. Upper Saddle River, NJ: Pearson Education Inc., 2015.
- [4] B. F. Gribel, M. N. Gribel, D. C. Frazão, J. a. McNamara, and F. R. Manzi, “Accuracy and reliability of craniometric measurements on lateral cephalometry and 3D measurements on CBCT scans.,” *Angle Orthod.*, vol. 81, no. 1, pp. 26–35, 2011.
- [5] J. B. Ludlow and C. Walker, “Assessment of phantom dosimetry and image quality of i-CAT FLX cone-beam computed tomography.,” *Am. J. Orthod. Dentofac. Orthop. Off. Publ. Am. Assoc. Orthod. Its Const. Soc. Am. Board Orthod.*, vol. 144, no. 6, pp. 802–17, Dec. 2013.
- [6] S. L. Hechler, “Cone-beam CT: applications in orthodontics.,” *Dent. Clin. North Am.*, vol. 52, no. 4, pp. 809–23, vii, Oct. 2008.
- [7] W. C. Scarfe, Z. Li, W. Aboelmaaty, S. a. Scott, and a. G. Farman, “Maxillofacial cone beam computed tomography: essence, elements and steps to interpretation.,” *Aust. Dent. J.*, vol. 57 Suppl 1, pp. 46–60, 2012.
- [8] J. Makdissi, “Cone beam CT in orthodontics: The current picture,” *Int. Orthod.*, vol. 11, no. 1, pp. 1–20, Mar. 2013.
- [9] M. O. Lagravère, J. M. Gordon, C. Flores-Mir, J. Carey, G. Heo, and P. W. Major, “Cranial base foramen location accuracy and reliability in cone-beam computerized

tomography.,” *Am. J. Orthod. Dentofac. Orthop. Off. Publ. Am. Assoc. Orthod. Its Const. Soc. Am. Board Orthod.*, vol. 139, no. 3, pp. e203–10, Mar. 2011.

- [10] P. Naji, N. A. Alsufyani, and M. O. Lagravère, “Reliability of anatomic structures as landmarks in three-dimensional cephalometric analysis using CBCT,” Dec. 2013.

2 METHODS OF SUPERIMPOSITION FOR ORTHODONTIC IMAGES: A REVIEW

There are a number of current methods used in literature for retrospective superimposition in orthodontics. Herein, the different methods are discussed, which, includes a brief descriptions of how the most common techniques work. The benefits and drawbacks of the different techniques are also compared and contrasted. Finally, any gaps in the literature where new techniques may be useful are also highlighted. Prior to this chapter being submitted to a peer reviewed journal the methods laid out will be applied to additional databases to find any missed publications. The chapter in its current format gives a solid background and overview of the retrospective superimposition methods currently used in orthodontics.

2.1 INTRODUCTION

Superimposition, also known as registration, or fusion, is a technique used in orthodontics to assess changes in patient morphology with growth, development, and treatment. Traditionally superimposition was performed on two-dimensional (2D) radiographs (cephalograms) [1]. Cone Beam Computed Tomography (CBCT) allows for low radiation dosage, three-dimensional (3D) radiographs. CBCT has a radiation dose multiple times higher than traditional 2D cephalography, comparable to panoramic x-rays depending on machine settings, while providing more information than both scans combined [2], [3]. Due to the moderate dosage, and increased information per scan, CBCT is increasing in use in orthodontics. The increase of 3D scans means that new methods of using these images for diagnosis and treatment planning, among them superimposition, need to be explored.

Superimposition for orthodontics is unique compared to many applications. Scans are often taken intermittently during treatment, months, or potentially even years apart. Most orthodontic treatments occur during adolescence, when the skull is still changing with patient growth, and all the permanent teeth are present in the mouth. CBCT outputs scans with moderate image noise, which will only increase as the industry seeks to provide lower

radiation dose imaging [4]. The result of orthodontics being such a unique imaging modality is that superimposition methods that work for other applications cannot be assumed adequate for orthodontics. Accurate superimposition in orthodontics will help improve patient diagnosis and treatment selection, and treatment assessment.

Superimposition can be done following three general methods, (a) voxel-based, (b) point-based, and (c) surface-based. Voxel-based methods work by comparing the intensity value of voxels in a first image, taken at time 1 (T1) to a second image, taken at time 2 (T2). The most popular voxel-based registration method is maximization of mutual information (MMI) [5]. Point-based methods work through aligning a series of points to try to get corresponding points as close as possible. The most common point based method is minimizing the least square errors of the corresponding points between T1 and T2. Surface-based methods work by creating a surface from a similar region in both T1 and T2 images, these surfaces are then registered. The most common surface based method is iterative closest point (ICP) [6]. Regardless of the superimposition method used, a rigid registration (rotation and translation) needs six degrees of freedom (three rotations and three translations). If scaling or deformation of an image is required for the registration, the degrees of freedom will increase.

This study is a literature review for retrospective superimposition methods of 3D CBCT scans. In registration the term retrospective means that nothing can be added to the scan (fiducial markers) ahead of time to assist in the superimposition. The reason for this is methods requiring fiducial markers must be planned before the scan is taken, and depending on patient growth, may not be easily placed in stable regions. Introspective methods also can be adopted into any clinic at any time and used with all previously acquired scans. If registration methods requiring fiducial markers are used, then older scans without the markers present cannot be registered. Registration using fiducial markers is most appropriate for short term testing, where a device placed on the patient can be considered stable. This study is also restricted to solely registration used with CBCT, registration techniques for other imaging modalities such as magnetic resonance imaging (MRI) or medical CT are not included. CBCT is a unique imaging modality though many of the techniques shown can be adapted to other imaging modalities.

2.2 MATERIALS AND METHODS

The systematic literature review was completed using the PubMed database on Oct 1/ 2015. An additional review of the database was performed on March 25/ 2016. The database was searched using the terms [Superimposition OR registration AND (Orthodontic OR Orthognathic) AND (3D OR three*dimensional)]. The * operator, known as a wildcard, allows for Three and Dimensional to separate with either a space or dash. Figure 2-1 illustrates the Venn diagram of the search terms. The results were then restricted to only contain results from the past 10 years. This was considered appropriate as CBCT started seeing frequent use in orthodontic clinics approximately 10 years ago. Since CBCT is a newer technology this is was deemed acceptable. The results were also restricted to include English language results only.

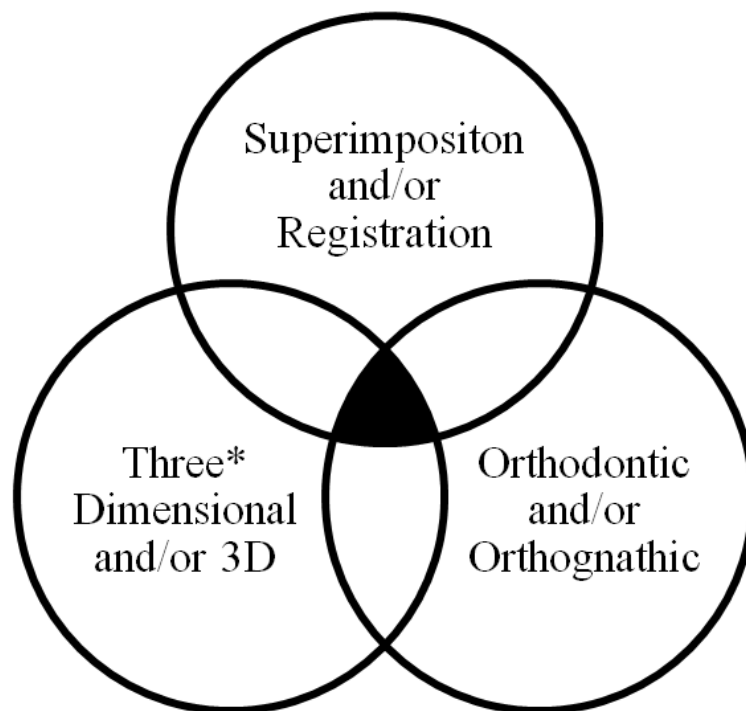


Figure 2-1. The Venn diagram shows the search terms that are used in the PubMed database. The intersection of the circles coloured black is the successful search results. The * operator, known as a wildcard, allows for Three and Dimensional to separate with either a space or dash.

After the papers were retrieved from the PubMed database the abstracts were read for relevancy. In order for the abstract to pass to the next stage of reading it had to mention that superimposition was performed. Once all the papers had their abstracts reviewed the papers were then read to determine relevancy. For a paper to be considered relevant it must pass 3 main criteria:

- (1) Have superimposition of two CBCT scans
- (2) Mention the distinct technique used for superimposition or at minimum, the software suite used if done using proprietary software
- (3) The superimposition is retrospective, i.e., does not use fiducial markers

2.3 RESULTS

The search terms of the PubMed database returned 83 results. When the documents were filtered to the past 10 years 73 papers were deemed appropriate. When the results were filtered to English language papers a total of 68 papers were retrieved.

Forty-four papers were deemed relevant to the literature review after they were screened by abstract. Eight papers were excluded due to using fiducial markers, 9 were excluded as the focuses on superimposition of a CBCT scan with laser scanned plaster models. Two publications were excluded for superimposing a CBCT scan with a wax bite, meaning a single CBCT scan was registered with a single wax bite to allow for increased detail of the bite surface. Two publications were excluded for focusing on superimposition of 2D images with a 3D CBCT scan, 2 papers were excluded for not stating the superimposition method or software, 1 article was excluded for only describing potential landmarks to use in superimposition, and lastly, 1 article was excluded for having the superimposition done by hand. Of the forty-four retrieved papers 17 were included in the literature review. The review of the database on March 25/2016 to check for new publications found one additional paper that was deemed appropriate, bringing the total number of papers to 18. This process is illustrated in Figure 2-2.

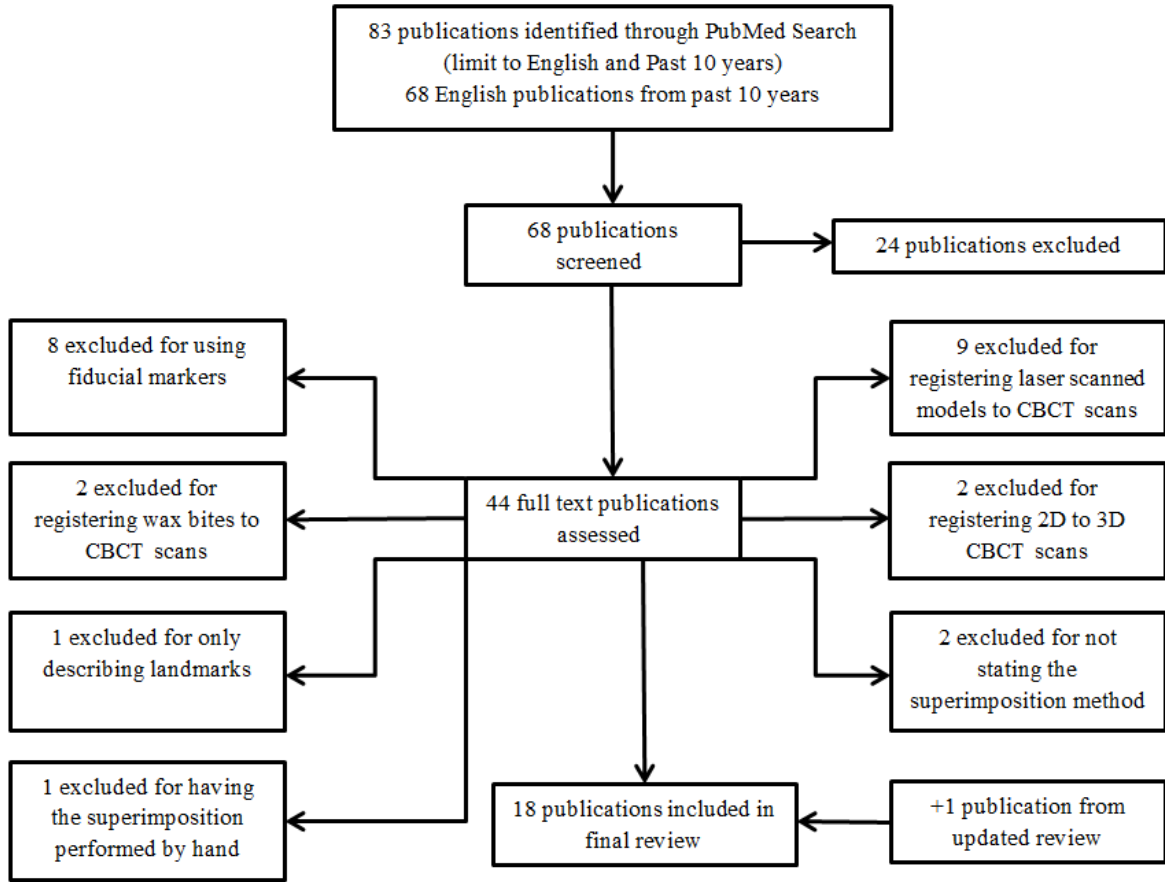


Figure 2-2. Flow chart showing the process of assessing publications for the review

The relevant information is the superimposition method used, error in the superimposition, section of the skull used for superimposition. The papers that passed the screening requirements are shown in Table 2-1. Baan *et al.*[7] also used a surface-based method, although the actual method used was not stated and is not included in Table 2-1.

Table 2-1. Studies included in the literature review. Any specific software that is used is stated.

Author (year)	Superimposition Method Used	Superimposition Error	Section of skull used
Baan F (2016) [7]	Maxilim Software (MMI)	-	Maxilla, mandible
Weissheimer A (2015) [8]	OnDemand3D Software (voxel based)	0.5mm	cranial base
Gkantidis N (2015) [9]	Geomagic Qualify 1012 for Windows Software: Three Point Registration	75 th percentile error value of 1.66mm	Three Points: Most superior point of the infraorbital foramen on left and right side and lowest point on mastoid process
	Geomagic Qualify 1012 for Windows Software: automated registration (surface, "best fit alignment")	Maximum 75 th percentile 1.16mm	Anterior Cranial Base
		Maximum 75 th percentile 0.17mm	Anterior cranial base & foramen magnum
		Maximum 75 th percentile 1.50mm	Both zygomatic arches
	Maximum 75 th percentile 2.32mm	Single zygomatic arch	
Nadjmi N (2014) [10]	MMI	-	area between infraorbital rim and scanned viscerocranium
Lemieux G (2014) [11]	4 Point Plane Method	0.5-0.6mm	Nasion, Right and Left Infraorbitals, Incisive Foramen
Hwang JJ (2014) [12]	OnDemand3D Software, Reorientation function (4 Point Plane)	1mm	Nasion, Sella Turcica, Basion, MLWS
Brunetto DP (2014) [13]	MMI	-	cranial base

Alsufyani NA (2014) [14]	6-Point Superimposition Method	1.5mm	Tip of nasal bone, tip of clivus, right and left foramen spinosum, left and right foramen ovale
Almukhtar A (2014) [15]	Maxilim Software(MMI)	0.050mm (voxel)	anterior cranial base
	VRMesh Software (ICP)	0.047mm (surface)	
Magnusson A (2013) [16]	normalized mutual information	-	anterior cranial base
Magnusson A (2012) [17]	normalized mutual information	-	anterior cranial base
Rino Neto J (2012) [18]	Meshlab Software(voxel- based coarse done on STL, then fine ICP)	meaningless to compare as they are assessing the image artifacts	entire FOV
Alhadidi A (2011) [19]	Imagine Software(MMI)	-	cranial base
Park SB (2012) [20]	OnDemand3D Software, fusion module (voxel)	-	cranial base
Cevitanes LH (2011) [21]	Imagine Software (MMI)	considered within 0.5mm	cranial base
Swennen GR (2009) [22]	Imagine Software (MMI)	0.08mm	Mandible
Cevitanes LH (2007) [23]	MIRIT Software (MMI)	less than 0.6mm	cranial base
Cevitanes LH (2005) [24]	MIRIT Software (MMI)	less than 0.6mm	cranial base

The results can be separated by three superimposition techniques: voxel-based, surface-based, or point-based. When categorised as such, 14 articles test voxel-based techniques, 2 articles test surface-based techniques, 4 articles test point-based techniques, 1 article advocates using a combination of techniques.

2.3.1 VOXEL-BASED METHODS

Fourteen of the eighteen papers used voxel-based registration methods. Maximization of mutual information (MMI) was the only method that was explicitly stated. This is not a surprising result since MMI is considered one of the most popular voxel-based registration techniques [25].

Only 3 of the papers that used voxel based methods did not explicitly use MMI, instead using proprietary software. Weissheimer *et al.* [8] and Park *et al.* [20] used the proprietary software OnDemand3D (Cybermed Inc., Korea), specifically the fusion module. Rino Neto *et al.* [18] used the software Meshlab (developed at the Computer Science Department of the University of Pisa, Italy), though it is unclear if it actually used a voxel-based method and a surface-based method or if only surface-based methods were used. Rino Neto claimed to have used a voxel-based method; however, all the registrations were performed on STL file formats of the scan (STL is a file format for saving solid models and lends itself well to surface-based registration methods).

MMI will be briefly described here since it is a common technique. Full descriptions of MMI can be found in Viola and Wells [5], and, Pluim *et al.* [25]. MMI works through measuring and comparing the entropy of two images. Entropy can be interpreted as the *information* the image contains. Entropy is restricted to be linearly related to the size of the image. For example, if a number can be made up of 6 random digits it would have half the entropy of a number made up of 12 random digits. Hartley [26] defined entropy as

$$H = \log s^n \quad (2-1)$$

where H is the entropy, s is the possible number of symbols (26 for the English alphabet, 256 for an 8 bit greyscale image, etc.), and n is the length of the message, e.g., if a message can be made up of the digits 0-9, a message 4 digits long would have a total entropy of

$$H = \log 10^4 = 4 \quad (2-2)$$

This definition of entropy can be viewed as a measure of uncertainty, e.g., if only one symbol is allowed ($s = 1$) then the entropy is zero ($\log 1 = 0$) since the message can be

known with absolute certainty. If a message can only contain the digit 1 and is 4 digits long it has entropy of 0, there is no uncertainty in the message [1111].

In practice there are many different forms of entropy; one commonly used measure is Shannon entropy [27]. Shannon entropy has the improvement of dealing with the probability different messages will occur, e.g., even though a child's first word can be any English word in the dictionary the word has an extremely high probability of being from a small subset, such as mom, dad, cat, or dog, knowing with high probability it will be those certain words, results in a low Shannon entropy. In the same example, the Hartley entropy would be extremely high since there are a large number of possibilities that are all considered equally probable. This is a simplified example and more information can be found in [25], [27]. When entropy is discussed in terms of an image, the message becomes the distribution of the greyscale values. This rudimentary introduction to entropy will assist in providing a meaningful description of MMI.

The last component of MMI is *feature space*. Feature space is a method of comparing T1 and T2. The axes of a feature space image are the **possible** greyscale values for T1 on axis 1 and the **possible** greyscale values of T2 on axis 2 (for an 8-bit image this would be 0-255). The pixel at any location (x,y) has an intensity representing the number of pixels with greyscale value x in T1 and a greyscale value y in T2 at the same pixel location. For example, the value of pixel (3,4) in the function space is the number of times that T1 has a greyscale value of 3 in the same location that T2 has a greyscale value of 4. This is shown for a simple image in Figure 2-3. Assuming that a feature in an image will have the relatively consistent greyscale values, then when features match up in two images it will appear as very bright clusters in feature space. It is not necessary that the greyscale value is consistent between images, only that it is consistent within an image.

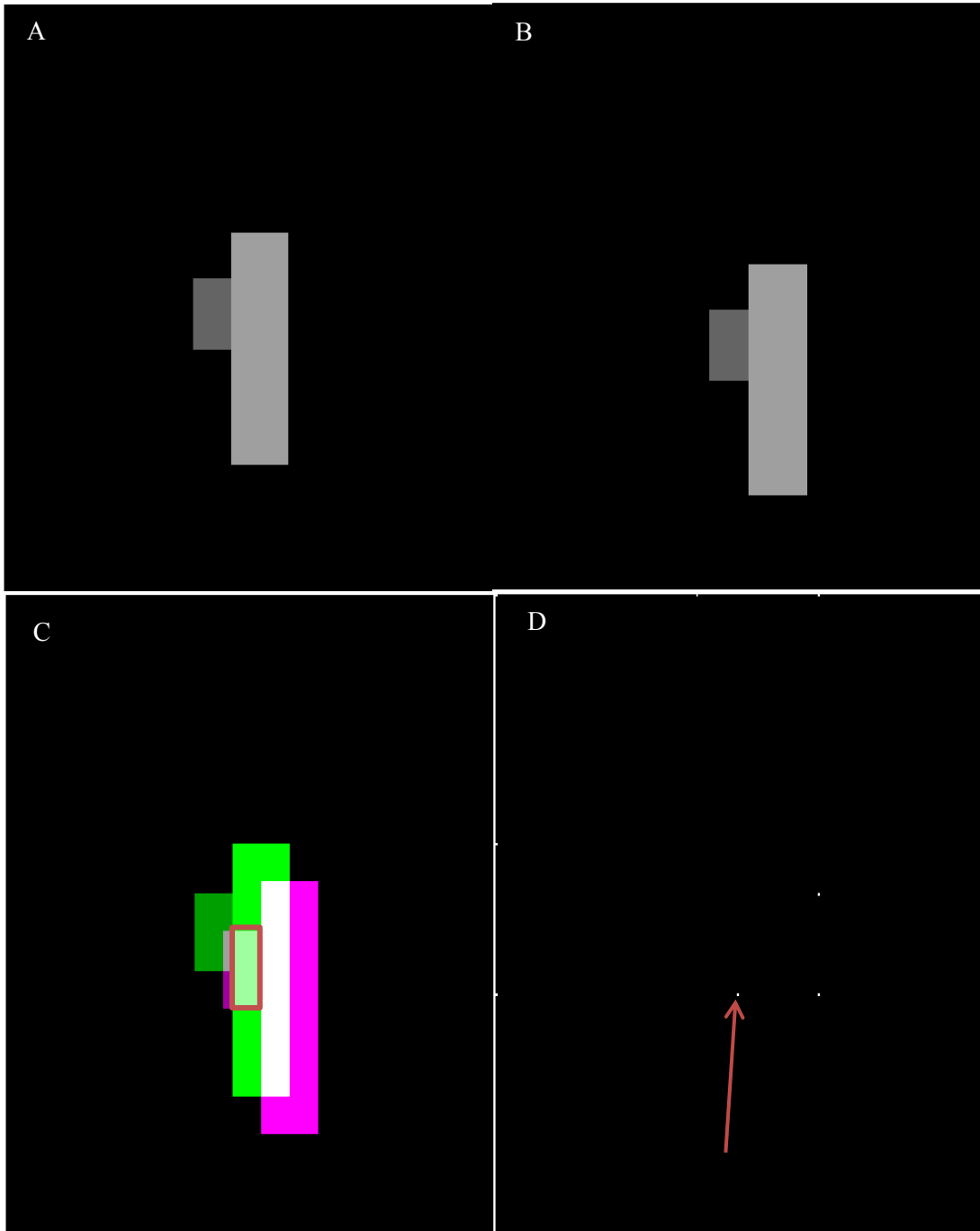


Figure 2-3. A simple image is shown in A, the simple image is then translated a small amount in B. C shows the two images overlapped with the original image A appearing green and the shifted image appearing pink. The area bordered in red is where the green image has voxel value of 160 and the pink image has voxel value of 100. 450 voxels fall within this square meaning that pixel (160,100), marked by an arrow, in the feature space image D has a value of 450.

The *mutual information* of an image can now be fully defined as¹

$$I(A, B) = H(A) + H(B) - H(A, B) \quad (2-3)$$

were H finds the entropy of an image as defined in (2-1), A is the T1 image, B is the T2 image, and $H(A, B)$ refers to the joint entropy or the entropy of the feature space. For 3D scans the method remains the same and the feature space is still a 2D histogram, the only difference being that T2 must be iterated in 6 degrees of freedom to find the maximum. Since I needs to be maximized for ideal registration, $H(A, B)$ needs to be minimized. $H(A, B)$ is minimized when there are few very distinct bright clusters and the rest of the function space is a consistent low value. Nearly any optimization technique can be used to find the maximum possible I value, though robustness to local maxima is important to find the global maximum. Theoretically T1 and T2 can be interchanged using this method; in practice this will cause some differences in the final solution.

2.3.2 SURFACE-BASED METHODS

Two of the papers retrieved used surface-based methods. One of the papers use the software VRMesh (VirtualGrid, Bellevue, WA, USA) to perform an iterative closest point (ICP) analysis, the other paper uses the GeoMagic (Rock Hill, SC, USA) software, with a setting of “best-fit alignment”.

Iterative closest point is the most successful surface-based registration method. ICP was originally outlined by Besl and McKay in 1992 [6]. The method works by taking two surfaces then assuming the closest points are the correct corresponding points. The second image is then moved to get all of the points as close as possible, minimizing a mean squared error function. It is possible that the corresponding points were not actual corresponding points so a new set of points is selected and it is again assumed the closest points correspond to each other. The image is then moved again in order to reduce the distances between the points. This is iterated through until convergence is reached. This technique is conceptually simple, however the mathematics are more complex than would

¹ There are multiple ways to define mutual information and in-depth look at the definitions that use Shannon entropy can be found in [25]

be relevant for this review. The mathematical workings of the method can be found in [6]. There are additional variants of the ICP algorithm that can be found in [28].

A benefit of the ICP method is that it is guaranteed to converge with a good initial guess. The main drawbacks of the ICP method are similar to the MMI method in that it may not find the global optimum and it requires a good starting pose. Another drawback of the ICP method is that the surfaces need to be delineated.

2.3.3 POINT-BASED METHODS

Four of the papers used point based-methods. Gkantidis *et al.* [9] and Hwang *et al.* [12] use point-based methods from the software GeoMagic and OnDemand3D respectively. Lemieux *et al.* [11] uses the 4 point method introduced by Lagravere *et al* [29]. Alsufyani *et al.* [14] uses the 6 point method introduced by DeCesare *et al* [30].

Point-based methods are rather simple and only get complex when the number of defined points increases. Gkantidis *et al.* [9] uses a three point method which simply sets one image to translate and rotate to overlap corresponding. There is no optimization or method of reducing error when using three points. The error of the method is directly related to the error in selecting the points. The 4 point method outlined by Lagravere *et al.* [29] is similar in that the error is related to the error in selecting the points used in the superimposition. Compared to the three point method used by Gkantidis *et al.* [9] the 4 point method used by Lagravere *et al.* [29] changes both images to a standardized coordinate system.

The 6 point method by DeCesare *et al.* [30] is more complex and allows for some landmarking error to be potentially reduced. The technique works by setting two types of points, main points and secondary points. The main points are the same 4 that are used to define the coordinate system in Lagravere *et al* [29]. T1 is then taken as a gold standard image, and T2 is allowed to change the location of three of the four main points (the origin cannot move). This is done by comparing the distances between the three points that can move with respect to each other, the origin, and two secondary points in T1 and T2. This is also done for the angles between all of the points. T2 is then allowed to move its three main points to try and best replicate the pattern (distance and angles) in the gold-standard image by minimizing the difference in distances and angles between T1 and T2. There is

also a weighting of importance between the main points and the secondary points. The mathematical development of the method is outside of the scope of this review but can be found in DeCesare *et al* [30]. The 6 point registration method is the only technique that is naturally non-rigid registration.

2.4 DISCUSSION

A review of the methods currently used for superimposition (also known as registration or fusion) in orthodontics was performed. This allows for a comparison of the multiple techniques currently suggested in literature. The three main categories of superimposition techniques are voxel-based methods, surface-based methods, and point-based methods.

The only voxel-based method used in literature is maximization of mutual information (MMI). As with any registration method there are benefits and drawbacks to its use. The main benefit of MMI is that it uses intensity values, meaning no landmark selection or surface delineation occurs. The drawback of MMI is that it is not guaranteed to find the global maximum; rather it can find local maxima depending on the robustness of the implemented solver. This results in the drawback that MMI requires a good starting pose (the images must be roughly registered) [5].

The only clearly stated surface-based method used in literature is iterative closest point (ICP) [6]. The main benefit of the ICP method is that it is guaranteed to converge with a good initial guess. The main drawbacks of the ICP method are similar to the MMI method in that it may not find the global optimum and it requires a good starting point. Another drawback of the ICP method is that the surfaces need to be delineated.

The point-based methods fall into two categories, techniques that do not perform any correction to the landmark selection and a technique that attempts to correct for the error in the landmark selection. Point-based methods can have variable benefits and detriments depending on the complexity used. The methods used in [9], [12], [29] do not require any iteration resulting in very fast registration. The 6-point method in [30] does require iteration to solve so it will have increased run time, though the trade-off will be a reduced superimposition error.

When comparing between the methods it is important to take into account the methods drawbacks as well as benefits. The different methods had varying levels of error, the greatest error was 2.32mm for a surface-based method [9]. This error is large enough to be considered not clinically acceptable, depending on the application, though the registration method used a very small surface for registration, the same method with a larger surface used reduced the error significantly [9]. The voxel-based and surface-based methods had an error that was deemed acceptable; normally the error was considered to be sub-voxel. An issue with point-based superimposition methods is that the overall error is difficult to quantify. Even though control patients and landmark reliability can be used as in [14], the error can only be known with reference to the measured points which will have unknown landmark error.

Due to the potential of patients undergoing growth during treatment most superimposition methods use a stable structure as the basis of their alignment. The anterior cranial base is often used as this stable structure. Gkantidis *et al.* [9] specifically compared a three point registration method to a surface based method using different structures within the skull. The smallest error they reported was for a surface based superimposition using the anterior cranial base with dorsal foramen magnum, while the largest error reported was for a surface based superimposition using just a single zygomatic arch as the reference structure. The fact that the 3 point method had an error between these two extremes is interesting and shows that if the reference structure gets too small it can become preferable to use a simpler point-based method. Almukhtar *et al.* [15] compared using MMI versus ICP. It was found that even though the mean errors were comparable the voxel-based MMI was preferred as it offered a smaller standard deviation of the superimposition results.

Reviewing Table 2-2 it can be seen that it would be beneficial to have additional tools for superimposition. Specifically, if a method that was able to converge to the best global solution could be implemented; it would fill a current gap in the available techniques that met all listed criteria. The point-based methods include iterative [30] and non-iterative methods [29].

Table 2-2. Simplified comparison of the current techniques used in orthodontics

	Guaranteed to Converge	Best Global Solution	Limited Pre-Processing	Iterative
Voxel-Based (MMI)	NO	NO	YES	YES
Surface-Based (ICP)	YES with good initial guess	NO	NO	YES
Point-Based	YES	NO	NO	Method-Dependant

In lay terms if all three methods were applied to the same image set they would all have different, yet comparable results. Both the voxel- and surface-based methods, and the 6-point method would have the lowest error, with all the other point-based methods having higher error. The simpler point-based methods would run much faster. The point-based methods also do not require having the entire patient scans, only a list of points if visualization is not required.

2.5 CONCLUSION

A systematic literature review of the PubMed database was performed. The topic of interest was retrospective superimposition of 3D CBCT scans for use in orthodontics and orthognathics. Superimposition techniques fall into 3 general categories, voxel-based techniques, surface-based techniques, and point-based techniques. Eighteen papers passed the review process. Fourteen of the seventeen papers used a voxel-based method, four of the papers used a point-based superimposition method, and two papers utilized a surface-based superimposition method. Some of the journal articles compared techniques or combined two different techniques. The final result of the review is that voxel-based

methods, specifically MMI is the most popular technique; however there is still room for improvement or introduction of new superimposition techniques.

2.6 REFERENCES

- [1] J. Huggare, “The handbook of cephalometric superimposition (2011),” *Eur. J. Orthod.*, vol. 34, no. 3, pp. 396–397, Jun. 2012.
- [2] J. B. Ludlow and C. Walker, “Assessment of phantom dosimetry and image quality of i-CAT FLX cone-beam computed tomography,” *Am. J. Orthod. Dentofacial Orthop.*, vol. 144, no. 6, pp. 802–817, Dec. 2013.
- [3] G. Li, “Patient radiation dose and protection from cone-beam computed tomography,” *Imaging Sci. Dent.*, vol. 43, no. 2, pp. 63–69, Jun. 2013.
- [4] J. L. Prince and J. M. Links, *Medical Imaging Signals and Systems*. Pearson Education, 2014.
- [5] P. Viola and W. M. Wells, “Alignment by maximization of mutual information,” in *Fifth International Conference on Computer Vision, 1995. Proceedings, 1995*, pp. 16–23.
- [6] P. J. Besl and H. D. McKay, “A method for registration of 3-D shapes,” *IEEE Trans. Pattern Anal. Mach. Intell.*, vol. 14, no. 2, pp. 239–256, Feb. 1992.
- [7] F. Baan, J. Liebrechts, T. Xi, R. Schreurs, M. de Koning, S. Bergé, and T. Maal, “A New 3D Tool for Assessing the Accuracy of Bimaxillary Surgery: The OrthoGnathicAnalyser,” *PLoS ONE*, vol. 11, no. 2, Feb. 2016.
- [8] A. Weissheimer, L. M. Menezes, L. Koerich, J. Pham, and L. H. S. Cevidanes, “Fast three-dimensional superimposition of cone beam computed tomography for orthopaedics and orthognathic surgery evaluation,” *Int. J. Oral Maxillofac. Surg.*, vol. 44, no. 9, pp. 1188–1196, Sep. 2015.
- [9] N. Gkantidis, M. Schauseil, P. Pazera, B. Zorkun, C. Katsaros, and B. Ludwig, “Evaluation of 3-Dimensional Superimposition Techniques on Various Skeletal Structures of the Head Using Surface Models,” *PLoS ONE*, vol. 10, no. 2, Feb. 2015.

- [10] N. Nadjmi, E. Defrancq, W. Mollemans, G. V. Hemelen, and S. Bergé, “Quantitative validation of a computer-aided maxillofacial planning system, focusing on soft tissue deformations,” *Ann. Maxillofac. Surg.*, vol. 4, no. 2, pp. 171–175, 2014.
- [11] G. Lemieux, J. P. Carey, C. Flores-Mir, M. Secanell, A. Hart, N. Dietrich, and M. O. Lagravère-Vich, “Three-dimensional cephalometric superimposition of the nasomaxillary complex,” *Am. J. Orthod. Dentofacial Orthop.*, vol. 146, no. 6, pp. 758–764, Dec. 2014.
- [12] J. J. Hwang, K.-D. Kim, H. Park, C. S. Park, and H.-G. Jeong, “Factors Influencing Superimposition Error of 3D Cephalometric Landmarks by Plane Orientation Method Using 4 Reference Points: 4 Point Superimposition Error Regression Model,” *PLoS ONE*, vol. 9, no. 11, p. e110665, Nov. 2014.
- [13] D. P. Brunetto, L. Velasco, L. Koerich, and M. T. de S. Araújo, “Prediction of 3-dimensional pharyngeal airway changes after orthognathic surgery: A preliminary study,” *Am. J. Orthod. Dentofacial Orthop.*, vol. 146, no. 3, pp. 299–309, Sep. 2014.
- [14] N. A. Alsufyani, N. H. Dietrich, M. O. Lagravère, J. P. Carey, and P. W. Major, “Cone beam computed tomography registration for 3-D airway analysis based on anatomic landmarks,” *Oral Surg. Oral Med. Oral Pathol. Oral Radiol.*, vol. 118, no. 3, pp. 371–383, Sep. 2014.
- [15] A. Almukhtar, X. Ju, B. Khambay, J. McDonald, and A. Ayoub, “Comparison of the Accuracy of Voxel Based Registration and Surface Based Registration for 3D Assessment of Surgical Change following Orthognathic Surgery,” *PLoS ONE*, vol. 9, no. 4, p. e93402, Apr. 2014.
- [16] A. Magnusson, K. Bjerklin, H. Kim, P. Nilsson, and A. Marcusson, “Three-dimensional computed tomographic analysis of changes to the external features of the nose after surgically assisted rapid maxillary expansion and orthodontic treatment: A prospective longitudinal study,” *Am. J. Orthod. Dentofacial Orthop.*, vol. 144, no. 3, pp. 404–413, Sep. 2013.

- [17] A. Magnusson, K. Bjerklin, H. Kim, P. Nilsson, and A. Marcusson, “Three-dimensional assessment of transverse skeletal changes after surgically assisted rapid maxillary expansion and orthodontic treatment: A prospective computerized tomography study,” *Am. J. Orthod. Dentofacial Orthop.*, vol. 142, no. 6, pp. 825–833, Dec. 2012.
- [18] J. Rino Neto, F. P. L. da Silva, I. Chilvarquer, J. B. de Paiva, and A. M. Hernandez, “Hausdorff Distance evaluation of orthodontic accessories’ streaking artifacts in 3D model superimposition,” *Braz. Oral Res.*, vol. 26, no. 5, pp. 450–456, Oct. 2012.
- [19] A. AlHadidi, L. H. Cevidanes, B. Paniagua, R. Cook, F. Festy, and D. Tyndall, “3D quantification of mandibular asymmetry using the SPHARM-PDM tool box,” *Int. J. Comput. Assist. Radiol. Surg.*, vol. 7, no. 2, pp. 265–271, Nov. 2011.
- [20] T.-J. Park, S.-H. Lee, and K.-S. Lee, “A method for mandibular dental arch superimposition using 3D cone beam CT and orthodontic 3D digital model,” *Korean J. Orthod.*, vol. 42, no. 4, pp. 169–181, Aug. 2012.
- [21] L. H. S. Cevidanes, A. Alhadidi, B. Paniagua, M. Styner, J. Ludlow, A. Mol, T. Turvey, W. R. Proffit, and P. E. Rossouw, “3D Quantification of Mandibular Asymmetry through Cone Beam Computed Tomography,” *Oral Surg. Oral Med. Oral Pathol. Oral Radiol. Endod.*, vol. 111, no. 6, pp. 757–770, Jun. 2011.
- [22] G. R. J. Swennen, W. Mollemans, C. De Clercq, J. Abeloos, P. Lamoral, F. Lippens, N. Neyt, J. Casselman, and F. Schutyser, “A Cone-Beam Computed Tomography Triple Scan Procedure to Obtain a Three-Dimensional Augmented Virtual Skull Model Appropriate for Orthognathic Surgery Planning:,” *J. Craniofac. Surg.*, vol. 20, no. 2, pp. 297–307, Mar. 2009.
- [23] L. H. S. Cevidanes, L. J. Bailey, S. F. Tucker, M. A. Styner, A. Mol, C. L. Phillips, W. R. Proffit, and T. Turvey, “Three-dimensional cone-beam computed tomography for assessment of mandibular changes after orthognathic surgery,” *Am. J. Orthod. Dentofac. Orthop. Off. Publ. Am. Assoc. Orthod. Its Const. Soc. Am. Board Orthod.*, vol. 131, no. 1, pp. 44–50, Jan. 2007.

- [24] L. Cevidanes, L. Bailey, G. Tucker, M. Styner, A. Mol, C. Phillips, W. Proffit, and T. Turvey, "Superimposition of 3D cone-beam CT models of orthognathic surgery patients," *Dento Maxillo Facial Radiol.*, vol. 34, no. 6, pp. 369–375, Nov. 2005.
- [25] J. P. W. Pluim, J. B. A. Maintz, and M. A. Viergever, "Mutual-information-based registration of medical images: a survey," *IEEE Trans. Med. Imaging*, vol. 22, no. 8, pp. 986–1004, Aug. 2003.
- [26] R. V. Hartley, "Transmission of Information," *Bell Syst. Tech. J.*, vol. 7.3, pp. 535–563, 1928.
- [27] C. E. Shannon, "A Mathematical Theory of Communication," *SIGMOBILE Mob Comput Commun Rev*, vol. 5, no. 1, pp. 3–55, Jan. 2001.
- [28] S. Rusinkiewicz and M. Levoy, "Efficient variants of the ICP algorithm," in *Third International Conference on 3-D Digital Imaging and Modeling, 2001. Proceedings, 2001*, pp. 145–152.
- [29] M. O. Lagravère, P. W. Major, and J. Carey, "Sensitivity analysis for plane orientation in three-dimensional cephalometric analysis based on superimposition of serial cone beam computed tomography images," *Dentomaxillofacial Radiol.*, vol. 39, no. 7, pp. 400–408, Oct. 2010.
- [30] A. DeCesare, M. Secanell, M. O. Lagravère, and J. Carey, "Multiobjective optimization framework for landmark measurement error correction in three-dimensional cephalometric tomography," *Dento Maxillo Facial Radiol.*, vol. 42, no. 7, p. 20130035, 2013.

3 ASSESSMENT OF CBCT IMAGING CAPABILITIES ON SUPERIMPOSITION AND REGISTRATION TECHNIQUES

3.1 INTRODUCTION

Cone-beam computed tomography (CBCT) is an imaging tool commonly used in the field of orthodontics and orthognathics for skeletal analysis, tooth localization, tooth inclination calculations, and assessment of nasomaxillary structural changes after treatments [1–3]. CBCT allows 3D analysis and 2D reconstructions of the sagittal, coronal, and axial planes, and provides a lower radiation alternative to computed tomography (CT), and can be justified when imaging is a necessary part of diagnosis and treatment planning [1], [2], [4], [5]. With appropriate software, the scan images can be secondarily reconstructed into traditional 2D radiographic images including the lateral cephalogram and panoramic X-ray [5]. Research has demonstrated that CBCT distance measurements are highly reproducible, accurate, and they do not show systematic differences with landmarking on conventional 2D radiographs on dried skulls [4], [5]. Segmentation of anatomic structures from imaging data, which is common with medical computed tomography (CT), is also available with CBCT. This allows quantification of structures and spaces, e.g. volume and area, a feature not possible with two-dimensional techniques [6].

It is known that variations in greyscale voxel values, spatial measurements, and image quality occur in CBCT depending on the machine used [7]. These variations exist in addition to traditional noise as seen in all X-ray imaging modalities due to the statistical randomness of X-ray creation and absorption [8]. Many studies attempt to test a single CBCT machine or compare multiple machines for useful metrics, while using the often unstated assumption that greyscale variation is negligible [9]–[11]. As CBCT scanners push radiation dosage lower, in order to be adopted for more standard clinical use, variations in voxel greyscale values will likely increase and image quality will decrease [8], [12].

Calibration is intended to increase repeatability of a machines scans by compensating for unavoidable hardware and software changes the machine has undergone over time. This will affect the machines repeatability in scanning. If calibration does have an effect on greyscale values, it will only compound the accuracy of greyscale based superimposition. It is also prudent to determine if calibration has an equal impact on all sections of a scan or if changes are localized. It has not currently been studied to find if machine calibration affect the results of a CBCT scan's greyscale profile.

Changes in voxel greyscale values and spatial measurements between otherwise identical scans could impact the use of CBCT for superimposition. There are three main non-invasive methods of superimposition (a) voxel-value based [13], [14], (b) shape based [15], [16], and (c) point-based superimpositions [17], [18]. In the literature the most common methods for superimposition of CBCT data in orthodontics are the maximization of mutual information (MMI) method (voxel-based) [19], [20] and point-based superimposition [15], [18], [21], [22]. One of the point-based methods, known colloquially as the 6-point method, reduces clinician landmark placement bias and error [18]. Other point-based methods are used, though are simplistic and simply overlap corresponding points with no correction for error [15], [21], [22]. Although all methods present reliable applications each method is affected by variations in CBCT scans. Distance based methods utilizing landmark location and landmark patterns are highly reliant on the accuracy of linear measurement [15], [17], [18], [21]–[24]. If distances are not consistent between repeated scans landmark location superimposition methods will have increased error regardless of researcher accuracy. Section 2.3.3 discusses the 6-point method in depth including its benefits and drawbacks. Voxel-based methods are reliant on a repeatability of greyscale values. Most voxel-based methods are resilient to some noise; however, if the CBCT machine noise is extremely large or has an odd distribution, it will impact voxel-based superimposition. Section 2.3.1 discusses maximization of mutual information and the pros and cons in depth. In shape-based methods a section of the scan is isolated and is then superimposed over the same region in a second scan. Depending on the size of the surface used localized errors in greyscale will not only influence surface selection (delineation), but also the superimposition of the regions. The most common surface-based registration, iterative closest point (ICP), is discussed in section 2.3.2. The accuracy of superimposition

methods will have some dependency on the quality and repeatability of scans from CBCT machines.

The effects of machine noise, de-calibration, and re-calibration could result in error in superimposition. The objective of this study is to determine if changes in local and global greyscale or linear distances will be a hindrance to any of the three superimposition types. This is important as the machine used for scanning could have a dominating impact on the usefulness of CBCT scans for superimposition.

3.2 MATERIALS AND METHODS

Scan data was collected using a clinical iCAT CBCT model 17-19 (Imaging Sciences International; Hatfield, PA USA) at the University of Alberta. Image reconstruction and conversion to the DICOM format was performed with the built in iCAT Vision software (Imaging Sciences International; Hatfield, PA U.S.A). Voxel size was 0.3mm with a 16cm x 13cm field of view (FOV). This created 420 slices of 512x512 voxels over a scan time of 8.9 seconds. The iCAT machine acquires the scan at 14 bit shade depth which is then converted to 16 bit shade depth. The machine was set to a 120 kV scan with 5 mA tube current.

Calibration of the iCAT machine was performed each morning prior to testing. Calibration is an automated function carried out by the technician. Both the Collimator and Detector Panel are calibrated in the standard calibration procedure. In an e-mail conversation with iCAT on more in-depth information of the calibration procedure, the authors were informed iCAT did not wish to have that information published.

A dry skull was placed in a container with a compartment surrounding it filled with water to simulate soft tissue. This technique has been used successfully by previous authors while working with CBCT [9], [25], [26]. The skull was placed and aligned in the machine using the laser alignment guides to position it adequately to obtain all necessary structures (Figure 3-1). A preview scan was also taken to ensure proper placement of the skull in the FOV. Scanning was performed 5 separate days, with calibration at the start of each day. Each day consisted of 7 scans taken 1 hour apart for a total of 35 scans.



Figure 3-1: Dry skull placed within container with water compartment to simulate tissue in the iCAT machine

During testing, the machine with the dry skull and water container was kept isolated to limit possible location based error [26]. Even kept in isolation, the skull underwent small movements due to machine vibrations while scanning. This imitates unavoidable patient movement during scanning due to patient breathing and machine vibration [27].

In this study, three different methods were used to test the repeatability, accuracy and calibration effects of the iCAT machine. These methods tested for:

- 1) Any change in distance measurement of set points on the skull between images within a day. This was to ensure linear measurements are consistent between scans. This is important for superimposition methods involving landmark patterns [15], [17], [18], [22].

- 2) The change in average global greyscale value. Since image noise is random this will give a strong indicator of any total net change, due to the large number of voxels involved. This will have an impact on superimposition methods that use large sections of an images greyscale [19], [20].
- 3) The change in local greyscale value of four distinct points in the maxillary arch in all the images: left and right 3rd molar, and left and right canine. This will assess if any significant de-calibration effects are location dependant as well as what are the calibration effects between days. This will affect the viability of superimposition techniques using only small areas of greyscale information.

Method 1 – Distance Measurement

To evaluate the distance between set points in all scans, two locations were chosen in each image and the distance between these points was measured in each scan. The locations chosen were the tips of metal screws in the dry skull which were landmarked with high precision, as shown in Figure 3-2. This choice of locations for measurement points allows the measured line to see change in all 3 planes (axial, coronal, and sagittal) as opposed to standard CBCT line measurement tests that only measure in the axial plane. Distances were measured using the built in distance tool in AVIZO. Distances were measured from 3D volume rendered images set to high quality. Distances were measured to the hundredth of a millimeter. Each scan was measured five times to reduce error, giving a total of 175 measurements over all 5 days.

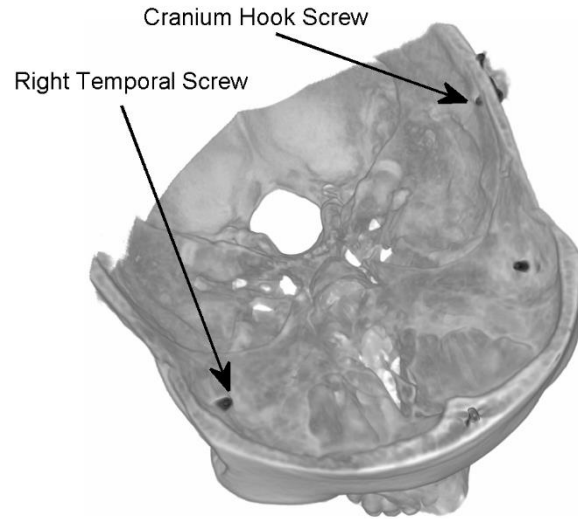


Figure 3-2: Locations landmarked to test for repeatability of linear measurements. All days used the same landmarks, the right temporal screw tip and the tip of the screw for attaching the cranial dome.

An ANOVA was run to find if statistically significant differences occur for measurements between days. Data was checked for normality using Q-Q plots. ANOVA is robust to minor violations of normality and the large number of samples validates the central limit theorem.

Method 2 – Global Voxel Greyscale Measurement

Method 2 tests for global greyscale, which is defined as a volume that sufficiently large enough to balance out the machine noise that is inherent to all x-ray modalities. The method to compare greyscales uses a sphere centered using 2 easily identifiable landmarks. After the sphere s is centered on the midpoint of the two chosen landmarks, the greyscale value of every voxel with its center lying in the sphere is averaged.

The landmarks used were the right and left foramen ovale. These landmarks were chosen due to their distinct shape allowing for highly reproducible landmarks as shown in Figure 3-3. Each scan was tested 100 times with a mild variation of 0.8mm imposed in landmark location. This repeated testing of the scans allows landmarking error to be effectively accounted for. This value of 0.8mm was chosen as this is approximately the intraexaminer reliability of selecting the ovale landmarks, previously found by Lagravere *et al.* to range from 0.26mm to 0.87mm [24]. With each scan being run 100 times a total of 700 greyscale measurements per day and 3500 greyscale measurements overall were acquired.

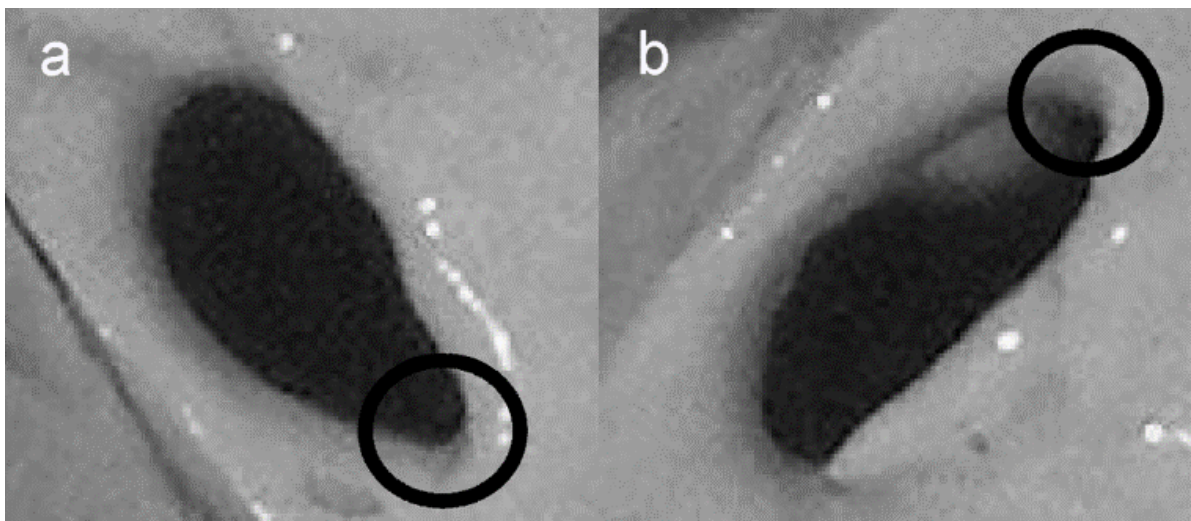


Figure 3-3: a) Close-up view of the left Foramen Ovale within the dry skull's cranial base. b) Close-up view of the Right Foramen Ovale. The circles show the pointed tip being used for landmark placement.

The sphere radius was set to 30mm. This allowed the entire cranial base to be included while excluding sections of the skull that may have fallen outside the FOV of some scans, such as the posterior edge of the dorsum foramen magnum. Figure 3-4, a and b, show the dry skull with the sphere inscribed. It should be noted that air values (~ -1000) are included in the sphere and the average greyscale calculations.

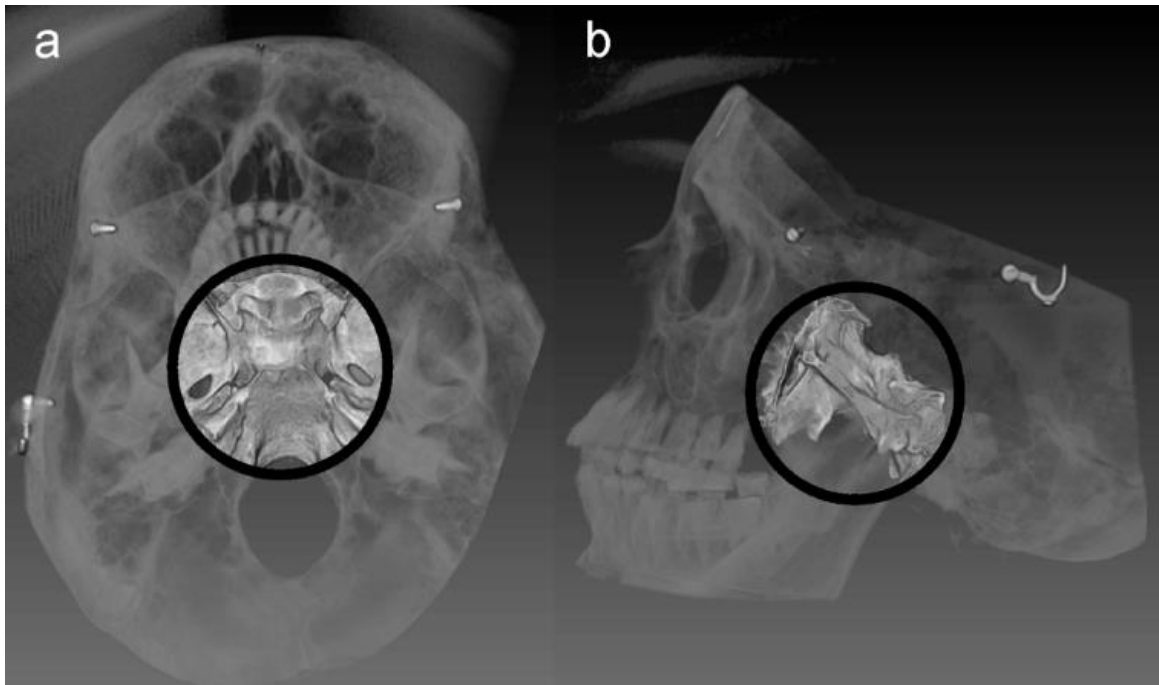


Figure 3-4: a) Axial view of the skull dry skull, the section of cranial base within the sphere is shown opaque b) Sagittal view of the skull with the bone within the sphere shown as opaque

Equations (3-1) and (3-2) are used for computing bone-normalized error and range-normalized error. These are used as metrics to determine how large a change is in meaningful terms. To find if change between calibration cycles is significant a repeated measures ANOVA is ran on the greyscale values of each day.

$$Error_{BONE} = \frac{\Delta x}{R_{BONE}} \quad (3-1)$$

$$Error_{RANGE} = \frac{\Delta x}{R_{MACHINE}} \quad (3-2)$$

In equation (3-1) and (3-2), Δx is the change in greyscale of interest, R_{BONE} is the greyscale range of bone within the image. This value is approximately $2500 - (-600) = 3100$ greyscale units for all the scans, obtained through thresholding from the low end when bone starts to be removed to the high end when enamel is barely thresholded out. This value was found through inspecting all the scans and was kept as the fixed value of 3100 for the entire analysis. In equation (3-2), $R_{MACHINE}$ is the operating greyscale range of the machine; i.e. 16,384 greyscale units.

Method 3 – Local Voxel Greyscale Measurement

To assess the change in greyscale values at a set location within an image, four teeth were chosen to give a symmetric view about the sagittal plane of the mouth. The four teeth are the left and right canines, and the left and right 3rd molars on the maxillary arch. A volume of dentin within the tooth was landmarked manually using 3 perpendicular views in AVIZO to limit any influence of root cavity or enamel. The tooth area was chosen as it is an easy to locate object with discernable borders to other materials (i.e. the material does not change gradually but has very distinct borders at the enamel and root pulp). Dentin can also be considered to be relatively consistent density, meaning greyscale variations due to the change in material density are limited. It was visually confirmed that the ROI did not include the root cavity or enamel in any of the scans. This orthogonal view system allowed for a single voxel to be located in all three planes using perpendicular axis aligned with the x, y, z directions of the DICOM scan. Orthogonal views of the left 3rd molar for day 1, scan 3, is shown in Figure 3-5 to illustrate this process (axes not shown). This process ensured that only dentin greyscale values would be compared with minimal influence of the pulp cavity or enamel layer. When a voxel was chosen as the point of interest, a cube of 5 by 5 by 5 voxels was constructed with the chosen voxel being the center. The greyscale average was taken of this larger 125-voxel cube for comparison. This compensated for change of greyscale between adjacent voxels of dentin greyscale values within a single tooth. The standard deviation of the 125-voxel cube, given for each scan, was computed using MATLAB statistical analysis toolbox. (Mathworks Inc., Natick, MA)

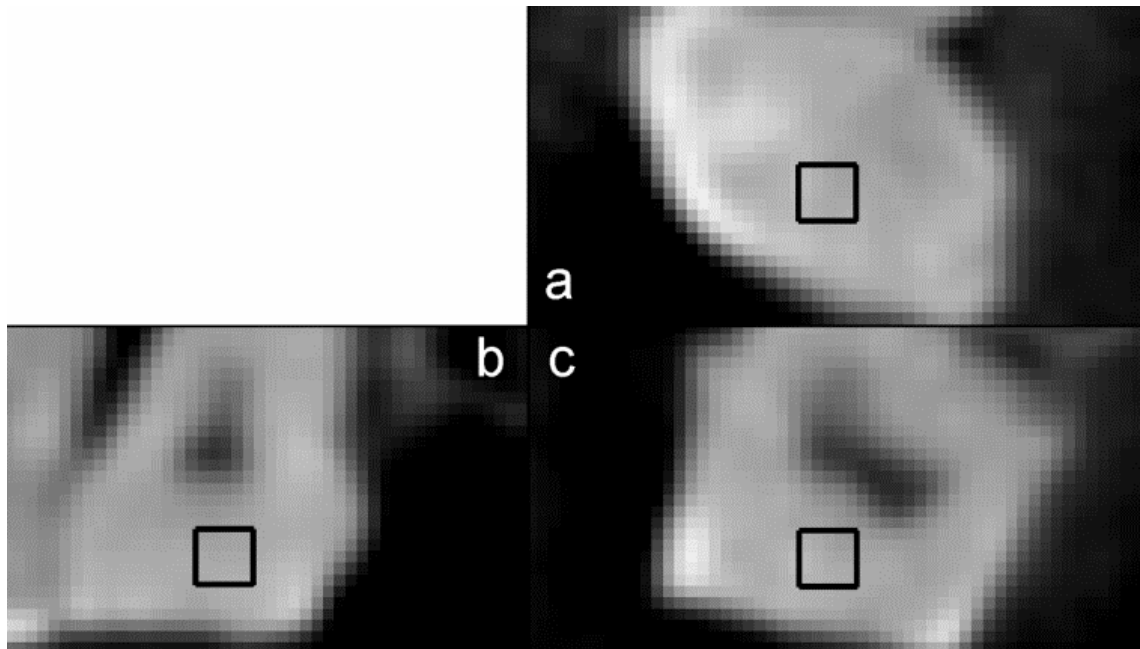


Figure 3-5: Left 3rd molar showing the 125 voxel cube used for computing location greyscale average. The three views are a) Axial plane, b) Sagittal plane, c) Coronal plane. The same voxel is the center of the black box in all 3 views.

A comparison was performed with the average of the 125-voxel cubes computed for each of the four teeth at each time step. A Friedman Analysis of Variance by-Ranks Test was used to assess change independently at each location as assumption of normality could not be met due to the small sample size of only 7 data points per day; this was confirmed by the Q-Q plots not showing normality.

All image calculations were performed using MATLAB's (Mathworks Inc., Natick, MA, USA) built in dicomread command. Visualization, thresholding limits, landmarking, and distance measurements were performed using AVIZO's (AVIZO 8.1, Visualisation Sciences Group, Burlington, MA) orthoviews, landmark, isosurface, volume render, and distance functions.

All statistical tests were performed using SPSS version 22 software (IBM, Armonk, NY, USA), unless otherwise noted.

3.3 RESULTS

3.3.1 METHOD 1- DISTANCE MEASUREMENTS

The results of method 1 are shown in Figure 3-6 using Tukey boxplots. The tapered region on each box represents the 95% confidence interval for the median for each day's measurement. The maximum change in distance measurement is 0.32mm, which is slightly greater than 1 voxel. The average distance measurement is 109.91mm. Outliers are determined by being greater than or less than 1.5 inter-quartile range (IQR) from the upper or lower quartile respectively.

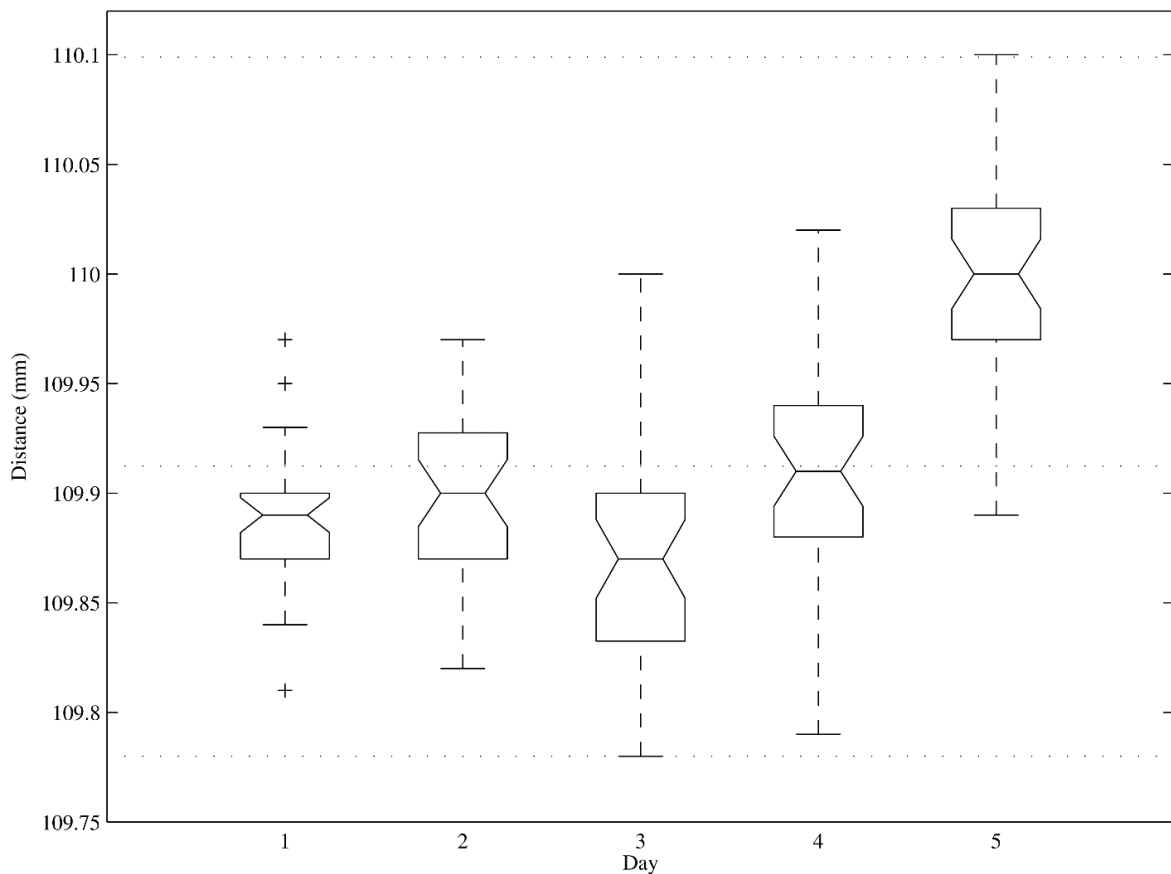


Figure 3-6: Boxplot of linear distances for each day, notches represent the 95% confidence interval for each day; + represent outliers greater than ± 1.5 IQR from the upper or lower quartile, respectively. Dotted lines represent the data max/min and average values.

As is shown in the boxplot by the 95% confidence interval notches, the changes between days is statistically significant. This is due to the results of day 5 measurements, which has its 95% confidence interval above the other days inter-quartile ranges. A repeated measures

ANOVA with Greenhouse-Geisser correction confirms this result ($P < 0.0005$). The grand estimated marginal mean is 109.912mm with 95% confidence interval bounds of [109.905,109.919].

3.3.2 METHOD 2 – GLOBAL VOXEL GREYSCALE MEASUREMENT

Plots for sphere averages for each day are shown in Figure 3-7 using Tukey boxplots.

Range normalized and bone normalized metrics for each day are shown in Table 3-1. **Standard deviation (SD) and descriptive metrics of sphere averages for each .** The largest difference in greyscale is 9.8 greyscale units. Using equations 1 and 2 this is 0.06% of machine range and 0.3% of the range of bone greyscale values. Repeated measures ANOVA show that there are statistically significant changes between the days results ($P < 0.0005$).

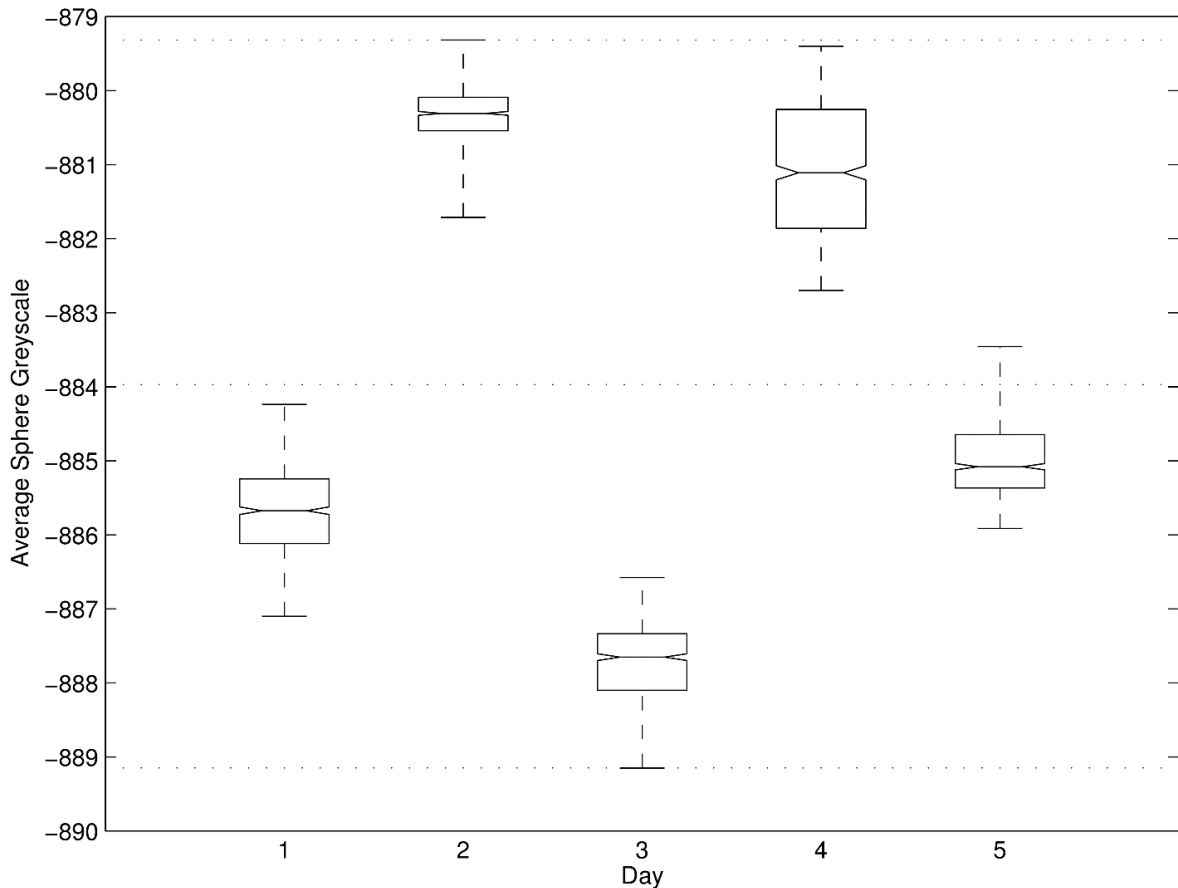


Figure 3-7: Greyscale average of a sphere of 3cm radius centered on the midpoint of the left and right foramen ovale. Tapered regions represent the 95% confidence interval for each day; + represent outliers greater than ± 1.5 IQR from the upper or lower quartile, respectively. Dotted lines represent the data max/min and average values.

Table 3-1 Standard deviation (SD) and descriptive metrics of sphere averages for each day

	SD (Greyscale)	Bone Normalized Max Variation (%)	Machine Normalized Max Variation (%)
Day 1	0.61	0.09	0.02
Day 2	0.46	0.08	0.01
Day 3	0.54	0.08	0.02
Day 4	0.85	0.10	0.02
Day 5	0.52	0.08	0.01

3.3.3 METHOD 3 – LOCAL VOXEL GREYSCALE MEASUREMENT

Figure 3-8 plots the greyscale value for each tooth separately, using Tukey boxplots. The largest standard deviation for the 125-voxel cubes is 157 greyscale units with an average standard deviation over all days of 85 greyscale units. The 125-voxel cube standard deviation, mean, and confidence interval were calculated using MATLAB statistical toolbox. (Mathworks Inc., Natick, MA) There does not appear to be any strong correlation between day of scans and greyscale value between the teeth, i.e. the effect of which day scans are taken, on the greyscale values of the teeth, is not consistent between teeth. Mean, standard deviation, and max range for each day are shown in Table 3-2.

Table 3-2: Mean and standard deviation (SD) of each tooth scan for each day. The largest change within a single day for each tooth is also shown. All values are in greyscale units. All teeth are in maxillary arch.

Tooth	Day 1	Day 2	Day 3	Day 4	Day 5	Max Range (Day)
	Mean (SD)	Mean (SD)	Mean (SD)	Mean (SD)	Mean (SD)	
Left 3 rd Molar	1017 (12.8)	918 (14.9)	841 (43.7)	881 (20.0)	858 (44.5)	133 (Day 5)
Left Canine	820 (20.4)	804 (55.2)	792 (77.2)	844 (63.8)	838 (38.0)	219 (Day 3)
Right Canine	820 (19.7)	795 (15.4)	769 (44.8)	862 (19.7)	851 (39.7)	122 (Day 3)
Right 3 rd Molar	1101 (27.3)	1057 (15.4)	972 (17.7)	983 (35.0)	960 (27.1)	97 (Day 4)

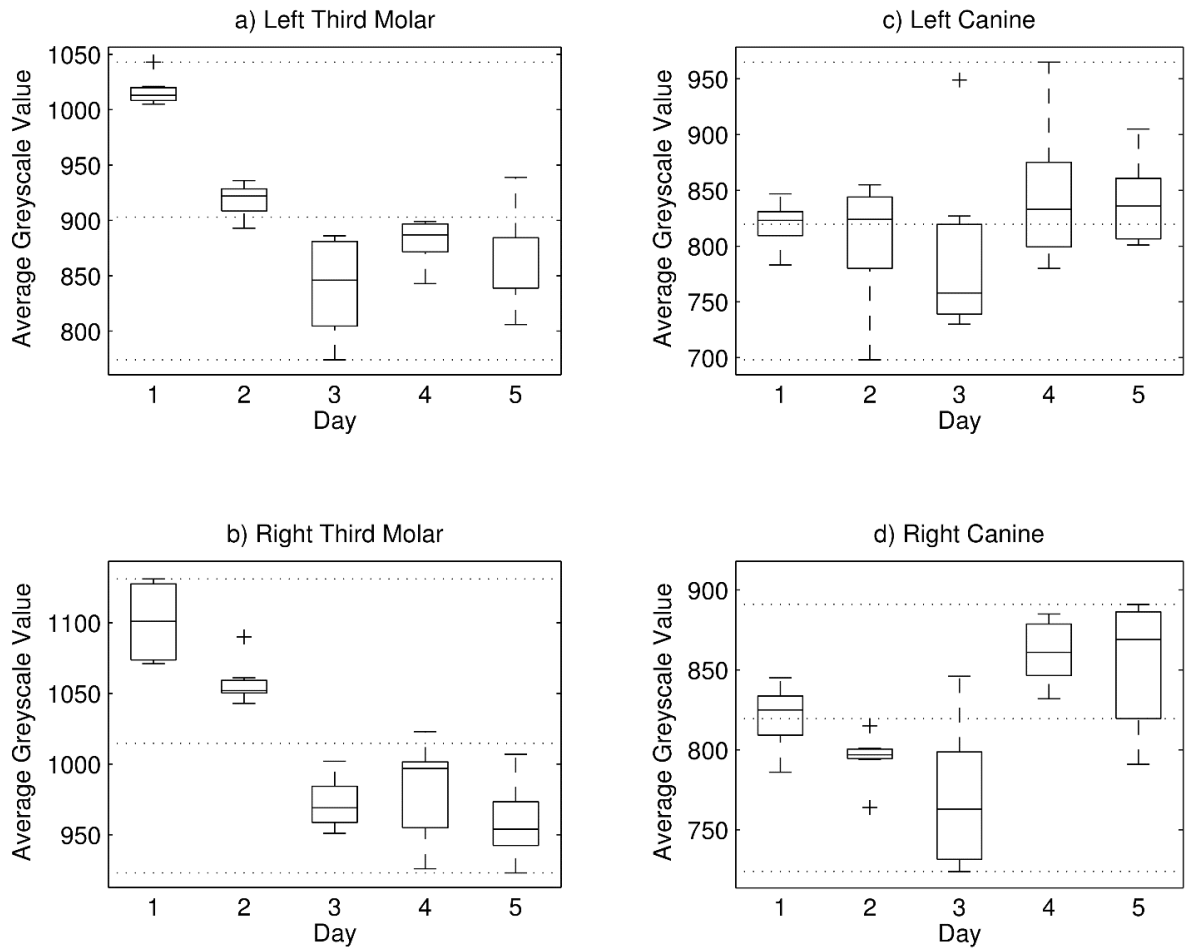


Figure 3-8: Greyscale average values of 125 voxel-cube of left third molar, left canine, right canine, right third molar dentin for each day. All teeth are in maxillary arch. Dotted lines represent max/min and average values while + represent outliers greater than ± 1.5 IQR from the upper or lower quartile, respectively.

Each tooth is compared separately between days using the Friedman Analysis of Variance by-Ranks test; results are provided in Table 3-3.

Table 3-3: Comparison of tooth greyscale values for within days and comparing days. The largest change between days and statistically significant P values are bolded.

Tooth	Largest Change Between Day (Greyscale)	P-value
Left 3 rd Molar	269	<0.0005
Left Canine	267	0.273
Right Canine	167	0.001
Right 3 rd Molar	208	<0.0005

3.4 DISCUSSION

The use of CBCT has unprecedented value in the dental field due to providing geometrically accurate 3D reconstruction with radiation dose comparable to standard panoramic X-rays [12], [28]. CBCT uses a unit of greyscales based on an object's radio-density and a machine's tube voltage and current. It is known that every CBCT machine gives different results [7]. Limited research has been published on the daily greyscale changes within a single machine [29]. No research has been found identifying if significant change in global and local voxel greyscale values is introduced by machine calibration. Changes in greyscale may affect the accuracy of greyscale based superimposition.

Differences in linear measurement and greyscale values between otherwise assumed identical scans (including machine settings such as tube voltage and current) will affect superimposition accuracy. Repeatability of linear measurements is paramount for image superimposition based on landmark locations and patterns, including those suggested by DeCesare *et al.* [18] and Lagravere *et al* [17]. If changes in local voxel greyscale values occur as well this will affect the suitability of intensity based superimposition methods, including image thresholding to automatically extract image features for later use in thresholding and measurement. This study tested the differences in scans for linear measurements, global greyscale values, and local greyscale voxel values.

3.4.1 DISTANCE MEASUREMENTS

The first method tested the repeatability and difference in distance measurements for each day. The distance between two metal screws was measured 5 times per scan for a total of 175 distance measurements. The variation in distance measurement within a day was found to be approximately a single voxel in size. When a comparison was done between the same points under the same conditions between days, statistically significant differences were found.

It is not possible to determine any unique cause of the differences seen between days. A highly likely scenario is a combination of many different errors that reduce measurement accuracy. One error is the vibrations the machine undergoes, which lead to movement in the container and skull. These vibrations will cause a blurring effect that will affect the

spatial resolution and any linear measurements taken. A second error source is due to the partial volume effect, the effect where in a voxel there may be multiple materials of varying density being represented as a single value, which will affect the accuracy of measuring the same location on an object in each scan and day. This issue applies regardless of measuring off of 2D scans or 3D renders, since this is a problem inherent to digitized X-ray imaging [8]. Error in measurement will also be affected by thresholding of the image for clarity and rendering the image in order to repeatedly locate the metal screw tips. Periago *et al.* found that measurements taken using 3D rendered images may be statistically significant from real life but can be considered clinically accurate [30]. Hassan *et al.* also found that small changes in patient head position do not affect the accuracy of linear measurements on 3D rendered surface models [31]. The radiographic measurements of 3D images are also potentially closer to the physical measurement than measuring off 2D slices and 2D projections [31]. Machine calibration may also introduce a factor which will affect each day differently but be consistent within a single day. This would contribute to the statistically significant results seen. All the other sources of error should have a random effect and would not cause a unique difference between each day.

Even though the change in distance measurements between days is statistically significant, the variation is small enough to be clinically insignificant for linear measurements in repeated scans. As the average error in landmark selection is greater than 0.6mm, as shown by Naji *et al.* [32], this intra- and inter-examiner reliability will dominate when landmark positions and distances are computed. There is no clinically significant effect of measurement error in repeated scans when comparing within a calibration cycle or when comparing between scans taken pre- and post-calibration. Landmark location and superimposition based off linear distances has negligible error introduced by the CBCT machine itself. This is expected as CBCT machines are often regarded as having good geometric accuracy [23], [28]. CBCT machinery will have negligible impact on the superimposition of CBCT scans; superimposition accuracy will depend on researcher landmarking ability and consistency.

3.4.2 GLOBAL GREYSCALE MEASUREMENTS

Method two tested the variation in a global average of voxel greyscale values of the cranial base. The iCAT machine keeps relatively constant greyscale values when viewed globally. For all days of testing, the largest change was less than 0.5% of the range of bone greyscale values (9 greyscale units).

The variation between days, while not clinically significant, does show a statistically significant difference ($P < 0.005$). As the sphere was kept the same size for all images, and variation in landmark selection was accounted for by repeating each measurement multiple times while allowing up to 0.8mm variation in landmark placement, this difference between days of global greyscale values comes from changes in the scan itself. This is unlikely due to inherent X-ray noise, which affects all scans equally, as the change in greyscale between days dominates. A more likely scenario dominating these global greyscale value changes between days is a combination of location-based errors, as suggested by Eskandarloo *et al.* [26] and machine calibration. Eskandarloo *et al.* found that for some CBCT machines, variations with movement of a posterior mandibular bone had changes in standard deviation between 31 greyscale units and 59 greyscale units [26]. The iCAT was not considered in their study and prevents direct comparison. However, error due to movement of the dry skull within the scan FOV would be minimized by using a large sphere to carry out an averaging procedure as Eskandarloo *et al.* report both negative and positive changes in greyscale value with change in position [26]. Location based error is unavoidable in a clinical setting as even using chin rests, biteplates, and laser locating systems, a patient's location will never be fully repeatable. This was also found in this study due to machine vibrations being large enough to be visually seen disturbing the water in the container during scanning. Comparison between location error and error introduced through calibration has not yet been studied to determine which one has a dominating impact. The largest variation within a single day, 3.3 greyscale values, occurs during day 4. This change is clinically negligible as differences of a single bone's greyscale values within the same person are greater. This variation is similar to the results of Spin-Neto *et al.* They found a mean greyscale difference with repeated scanning of a dry skull of -2.5 to -0.4 greyscale units using an iCAT CBCT with 30 minutes between scans [29]. As the

skull was kept isolated during each day, change in global greyscale average is not likely due to changes in skull location. Vibrational changes would be less than 1mm.

Since global greyscale values do not have large variation when measured using the same machine, it may be a useful indicator of changes in bone health or structural changes over time. The minimum number of voxels required to achieve a “global” view is unknown. In this study, the volume of the sphere was $1.13 \times 10^5 \text{mm}^3$, which is ~4.2 million voxels.

The proposed method has shown that for this particular machine the global greyscale is highly accurate regardless of calibration. This would be beneficial for research purposes. Contrary to the linear distances results discussed previous this change in global greyscale cannot be generalized to all CBCT machines, and has not been tested as extensively. It is important that machines used for quantitative purposes are tested to ensure consistent results with repeated scanning and calibration.

3.4.3 LOCAL GREYSCALE VALUES

Method 3 calculated the change in greyscale values when looking at a specific region of interest (ROI) within a bone structure. This included looking at the changes between days and within a day. The sample ROI used was the dentin of the canine and 3rd molar of the maxillary arch. The ROI was chosen to ensure that the influence of the pulp cavity and the enamel was minimized.

The difference between days is statistically significant. The largest variation between days is 269 greyscale units. The difference within a day is also statistically significant with the largest variation being 219 greyscale units for the day 3 left Canine, ignoring the outlier in day 3 left Canine, the largest in day variation is 185 greyscale for the day 4 left Canine. These changes in greyscale are important to superimposition as it will not only make a difference to the relative greyscale distribution in an image but algorithms that automate selection of a region of interest in an image. Though the variation is smaller than the variation presented in Spin-Neto *et al.* [29] their reported variation is larger than the entire greyscale range detected in this study. This could be the result of many factors including the phantom used (water to represent human tissue vs acrylic), the machine tube current and voltage settings, and machine differences.

It is prudent to mention that the large changes in greyscale diminish some the usefulness of greyscale values for quantitative diagnostic purposes. An example of this would be comparing the left canine and left 3rd molar, in day 1 the left 3rd molar appears to have the higher greyscale value. When the same teeth are compared by scans taken on a different day (4) the left canine could appear to have a higher greyscale value. Diminishing the usefulness of greyscale based comparison between these teeth.

The change in local greyscale values has ramifications regarding the size of an area used for superimposition. In greyscale based superimposition the cranial base is often used as the ROI as this region is stable during patient growth and treatment including rapid maxillary expansion. The apparent variability in greyscale values at a small spatial scale means that using an area smaller than the cranial base could have increased errors in superimposition. This is especially true as the average greyscale value did not undergo large change. This means an equal amount of change must occur else-where in the image to balance the global greyscale value. As an example, it would not be prudent to use only the area of the anterior clinoid process (Figure 3-9) as even though it is a unique structure the greyscale changes could cause superimposition errors.

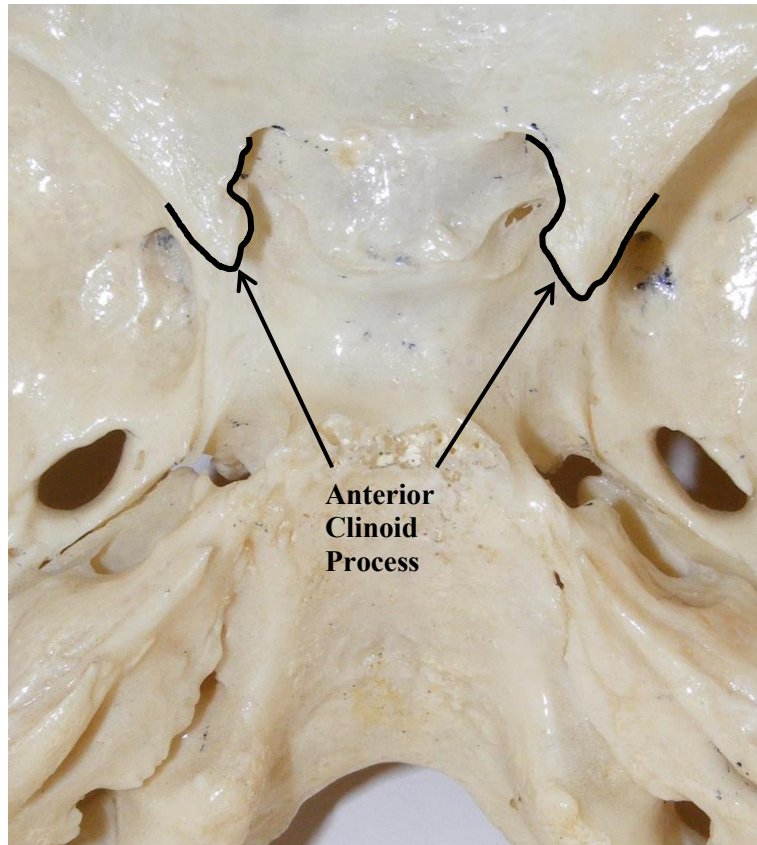


Figure 3-9: The anterior clinoid process (outlined in black) is the tips of bone that is raised above the rest of the cranial base. These pieces of bone are likely to small to be used as the only ROI in a greyscale based superimposition.

One way of avoiding the impact of the greyscale changes would be to threshold an image before a superimposition is performed. This could impact the suitability of some superimposition techniques however as the gradient of greyscale values within bone is removed. Caution is required though as if a large shift in greyscale happens around the threshold limit it could result areas of bone being interpreted as air and vice-versa. The ideal way to not have the local greyscale changes influence superimposition is to use a large area for the image superimposition; finding the minimum size for the superimposition area was outside the scope of this work.

3.5 CONCLUSION

Reliability and repeatability of relative greyscale values and distance measurements affect the accuracy of different superimposition methods. This study found that for an iCAT 17-19 CBCT machine that distances are accurate and reliable, global greyscale is accurate and reliable, and local greyscale is not reliable. The ramification of this is superimposition methods that rely on greyscale for either automated extraction of a surface or use direct greyscale information must ensure they use a large enough ROI. This paper makes no attempt to define the “large enough” requirement for the ROI. When designing techniques for superimposition it is also important to remember that as radiation dose lowers so does image quality. As lower patient dosage will always be a goal for routine diagnostic tests, techniques must be designed to cope with reduced image quality and increased image noise.

3.6 REFERENCES

- [1] V. Pangrazio-Kulbersh, P. Wine, M. Haughey, B. Pajtas, and R. Kaczynski, "Cone beam computed tomography evaluation of changes in the naso-maxillary complex associated with two types of maxillary expanders," *Angle Orthod.*, vol. 82, no. 3, pp. 448–457, Oct. 2011.
- [2] B. J. Garrett, J. M. Caruso, K. Rungcharassaeng, J. R. Farrage, J. S. Kim, and G. D. Taylor, "Editor's Summary, Q & A, Reviewer's Critique: Skeletal effects to the maxilla after rapid maxillary expansion assessed with cone-beam computed tomography," *Am. J. Orthod. Dentofacial Orthop.*, vol. 134, no. 1, pp. 8–9, Jul. 2008.
- [3] S. A. Rogers, N. Drage, and P. Durning, "Incidental findings arising with cone beam computed tomography imaging of the orthodontic patient," *Angle Orthod.*, vol. 81, no. 2, pp. 350–355, Jan. 2011.
- [4] D. Grauer, L. S. H. Cevidanes, M. A. Styner, I. Heulfe, E. T. Harmon, H. Zhu, and W. R. Proffit, "Accuracy and Landmark Error Calculation Using Cone-Beam Computed Tomography–Generated Cephalograms," *Angle Orthod.*, vol. 80, no. 2, pp. 286–294, Nov. 2009.
- [5] B. F. Gribel, M. N. Gribel, D. C. Frazão, J. A. McNamara, and F. R. Manzi, "Accuracy and reliability of craniometric measurements on lateral cephalometry and 3D measurements on CBCT scans," *Angle Orthod.*, vol. 81, no. 1, pp. 26–35, Oct. 2010.
- [6] Y. Liu, R. Olszewski, E. S. Alexandroni, R. Enciso, T. Xu, and J. K. Mah, "The Validity of In Vivo Tooth Volume Determinations From Cone-Beam Computed Tomography," *Angle Orthod.*, vol. 80, no. 1, pp. 160–166, Oct. 2009.
- [7] K. Kamburoglu, S. Murat, E. Kolsuz, H. Kurt, S. Yüksel, and C. Paksoy, "Comparative assessment of subjective image quality of cross-sectional cone-beam computed tomography scans," *J. Oral Sci.*, vol. 53, no. 4, pp. 501–508, 2011.

- [8] J. L. Prince and J. M. Links, *Medical Imaging Signals and Systems*. Pearson Education, 2014.
- [9] M. Lagravère, Y. Fang, J. Carey, R. Toogood, G. Packota, and P. Major, “Density conversion factor determined using a cone-beam computed tomography unit NewTom QR-DVT 9000,” *Dentomaxillofacial Radiol.*, vol. 35, no. 6, pp. 407–409, Nov. 2006.
- [10] P. Mah, T. E. Reeves, and W. D. McDavid, “Deriving Hounsfield units using grey levels in cone beam computed tomography,” *Dentomaxillofacial Radiol.*, vol. 39, no. 6, pp. 323–335, Sep. 2010.
- [11] T. Reeves, P. Mah, and W. McDavid, “Deriving Hounsfield units using grey levels in cone beam CT: a clinical application,” *Dentomaxillofacial Radiol.*, vol. 41, no. 6, pp. 500–508, Sep. 2012.
- [12] J. B. Ludlow and C. Walker, “Assessment of phantom dosimetry and image quality of i-CAT FLX cone-beam computed tomography,” *Am. J. Orthod. Dentofacial Orthop.*, vol. 144, no. 6, pp. 802–817, Dec. 2013.
- [13] L. Cevidanes, L. Bailey, G. Tucker, M. Styner, A. Mol, C. Phillips, W. Proffit, and T. Turvey, “Superimposition of 3D cone-beam CT models of orthognathic surgery patients,” *Dentomaxillofacial Radiol.*, vol. 34, no. 6, pp. 369–375, Nov. 2005.
- [14] A. AlHadidi, L. H. Cevidanes, B. Paniagua, R. Cook, F. Festy, and D. Tyndall, “3D quantification of mandibular asymmetry using the SPHARM-PDM tool box,” *Int. J. Comput. Assist. Radiol. Surg.*, vol. 7, no. 2, pp. 265–271, Nov. 2011.
- [15] N. Gkantidis, M. Schauseil, P. Pazera, B. Zorkun, C. Katsaros, and B. Ludwig, “Evaluation of 3-Dimensional Superimposition Techniques on Various Skeletal Structures of the Head Using Surface Models,” *PLoS ONE*, vol. 10, no. 2, Feb. 2015.
- [16] A. Almukhtar, X. Ju, B. Khambay, J. McDonald, and A. Ayoub, “Comparison of the Accuracy of Voxel Based Registration and Surface Based Registration for 3D

- Assessment of Surgical Change following Orthognathic Surgery,” *PLoS ONE*, vol. 9, no. 4, p. e93402, Apr. 2014.
- [17] M. O. Lagravère, P. W. Major, and J. Carey, “Sensitivity analysis for plane orientation in three-dimensional cephalometric analysis based on superimposition of serial cone beam computed tomography images,” *Dentomaxillofacial Radiol.*, vol. 39, no. 7, pp. 400–408, Oct. 2010.
- [18] A. DeCesare, M. Secanell, M. O. Lagravère, and J. Carey, “Multiobjective optimization framework for landmark measurement error correction in three-dimensional cephalometric tomography,” *Dento Maxillo Facial Radiol.*, vol. 42, no. 7, p. 20130035, 2013.
- [19] P. Viola and W. M. Wells, “Alignment by maximization of mutual information,” in , *Fifth International Conference on Computer Vision, 1995. Proceedings, 1995*, pp. 16–23.
- [20] J. P. W. Pluim, J. B. A. Maintz, and M. A. Viergever, “Mutual-information-based registration of medical images: a survey,” *IEEE Trans. Med. Imaging*, vol. 22, no. 8, pp. 986–1004, Aug. 2003.
- [21] G. Lemieux, J. P. Carey, C. Flores-Mir, M. Secanell, A. Hart, N. Dietrich, and M. O. Lagravère-Vich, “Three-dimensional cephalometric superimposition of the nasomaxillary complex,” *Am. J. Orthod. Dentofacial Orthop.*, vol. 146, no. 6, pp. 758–764, Dec. 2014.
- [22] J. J. Hwang, K.-D. Kim, H. Park, C. S. Park, and H.-G. Jeong, “Factors Influencing Superimposition Error of 3D Cephalometric Landmarks by Plane Orientation Method Using 4 Reference Points: 4 Point Superimposition Error Regression Model,” *PLoS ONE*, vol. 9, no. 11, p. e110665, Nov. 2014.
- [23] M. O. Lagravère, J. Carey, R. W. Toogood, and P. W. Major, “Three-dimensional accuracy of measurements made with software on cone-beam computed tomography images,” *Am. J. Orthod. Dentofacial Orthop.*, vol. 134, no. 1, pp. 112–116, Jul. 2008.

- [24] M. O. Lagravère, J. M. Gordon, C. Flores-Mir, J. Carey, G. Heo, and P. W. Major, "Cranial base foramen location accuracy and reliability in cone-beam computerized tomography," *Am. J. Orthod. Dentofacial Orthop.*, vol. 139, no. 3, pp. e203–e210, Mar. 2011.
- [25] M. O. Lagravère, J. Carey, M. Ben-Zvi, G. V. Packota, and P. W. Major, "Effect of object location on the density measurement and Hounsfield conversion in a NewTom 3G cone beam computed tomography unit," *Dentomaxillofacial Radiol.*, vol. 37, no. 6, pp. 305–308, Sep. 2008.
- [26] A. Eskandarloo, M. Abdinian, F. Salemi, Z. Hashemzadeh, and M. Safaei, "Effect of object location on the density measurement in cone-beam computed tomography versus multislice computed tomography," *Dent. Res. J.*, vol. 9, no. Suppl 1, p. S81, 2012.
- [27] T. Hanzelka, J. Dusek, F. Ocasek, J. Kucera, J. Sedy, J. Benes, G. Pavlikova, and R. Foltan, "Movement of the patient and the cone beam computed tomography scanner: objectives and possible solutions," *Oral Surg. Oral Med. Oral Pathol. Oral Radiol.*, vol. 116, no. 6, pp. 769–773, Dec. 2013.
- [28] W. C. Scarfe and A. G. Farman, "What is Cone-Beam CT and How Does it Work?," *Dent. Clin. North Am.*, vol. 52, no. 4, pp. 707–730, Oct. 2008.
- [29] R. Spin-Neto, E. Gotfredsen, and A. Wenzel, "Variation in voxel value distribution and effect of time between exposures in six CBCT units," *Dentomaxillofacial Radiol.*, vol. 43, no. 4, p. 20130376, Feb. 2014.
- [30] D. R. Periago, W. C. Scarfe, M. Moshiri, J. P. Scheetz, A. M. Silveira, and A. G. Farman, "Linear Accuracy and Reliability of Cone Beam CT Derived 3-Dimensional Images Constructed Using an Orthodontic Volumetric Rendering Program," *Angle Orthod.*, vol. 78, no. 3, pp. 387–395, May 2008.
- [31] B. Hassan, P. van der Stelt, and G. Sanderink, "Accuracy of three-dimensional measurements obtained from cone beam computed tomography surface-rendered

images for cephalometric analysis: influence of patient scanning position,” *Eur. J. Orthod.*, vol. 31, no. 2, pp. 129–134, Apr. 2009.

- [32] P. Naji, N. A. Alsufyani, and M. O. Lagravère, “Reliability of anatomic structures as landmarks in three-dimensional cephalometric analysis using CBCT,” *Angle Orthod.*, vol. 84, no. 5, pp. 762–772, Sep. 2014.

4 DEVELOPMENT OF A REGISTRATION ALGORITHM FOR 3D CBCT IMAGE SUPERIMPOSITION

Registration, or superimposition, overlaps two images so that changes between them are quantifiable. In orthodontics, this is important as it provides an orthodontist with techniques to determine, and visualize, the growth- and treatment-based changes a patient has undergone. Since Cone-Beam Computed Tomography (CBCT) allows for 1:1 scaled, three-dimensional (3D) images, it is seeing increasing use in orthodontic clinics, resulting in 3D registration being required more often.

While there are many different techniques for 3D image superimposition, all of them must take into account, and balance, a multitude of factors. These factors include but are not limited to, the type of scans being registered, the required registration accuracy, the time the registration takes to converge to the final solution, and the difficulty in setting up the registration. In this thesis, the three most important factors affecting superimposition are considered to be:

1. Superimposition accuracy, the superimposition needs to be accurate or measurements between the registered images will have clinically significant error. If error between scans is clinically significant, the wrong conclusions regarding treatment could be made, resulting in extraneous treatment plans.
2. Time required for the superimposition. If a superimposition technique requires a long time to register two images it will see limited use in orthodontic clinics where clinicians are often stressed for time. If a reliable superimposition method registers images fast enough to see regular use in an orthodontic clinic it will allow clinicians to make reliable treatment decisions.
3. Researcher and clinician involvement. If the superimposition technique is technically complex, or has a steep learning curve clinicians will instead use methods they know and are experienced in. Superimposition methods must be easy to use and not require large amounts of set-up or pre-processing.

This chapter outlines the mathematical algorithm used in this thesis for image registration. The first section describes the Fourier transform. The second section focuses on the properties and techniques that are pertinent to the mathematical proof. The third section provides an in-depth proof of the registration method. The fourth section will look at additional techniques to improve phase correlation, such as filtering and thresholding; including tests on patient data to determine the effectiveness of techniques. The fifth section is a visual run through of the method using a simple geometric volume.

For this entire chapter (x, y, z) refers to the spatial domain, (u, v, w) refers to the frequency (Fourier) domain, and (i, j, k) refers to voxel indices in the computer coordinate system, meaning $(i, j, k) \in \mathbb{Z}$.

All Fourier transforms in this chapter are calculated using MATLAB's fast Fourier transform (`fft`) method (Mathworks Inc., Natick, MA, USA).

4.1 THE FOURIER TRANSFORM

The purpose of the Fourier transform is to convert any signal in the spatial (or time) domain to the frequency domain. The most intuitive way to show this is with the similar Fourier Series method. The Fourier series is a method to approximate a periodic function as a sum of discrete terms containing cosine and sin functions as shown in Figure 4-1 [1].

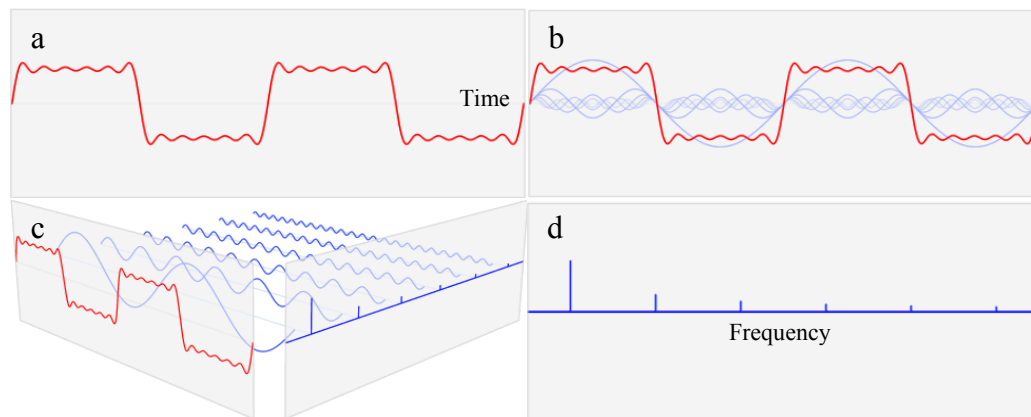


Figure 4-1. This composite shows a periodic signal in the time domain (a) being represented as a sum of trigonometric functions (b) in order to convert the image to the frequency domain (d). This means that sub-figure a and d are actually the same signal just represented in the spatial versus frequency domain. Adapted from [1].

Similar to the Fourier series, the Fourier transform converts a signal to the frequency domain. The difference however is that the Fourier transform is for non-periodic signals on the interval $-\infty$ to ∞ . The Fourier transform also does not create a discrete representation (a sum of terms) but a continuous representation using integration. Figure 4-2 shows the Fourier transform of a single period of the signal in Figure 4-1a.

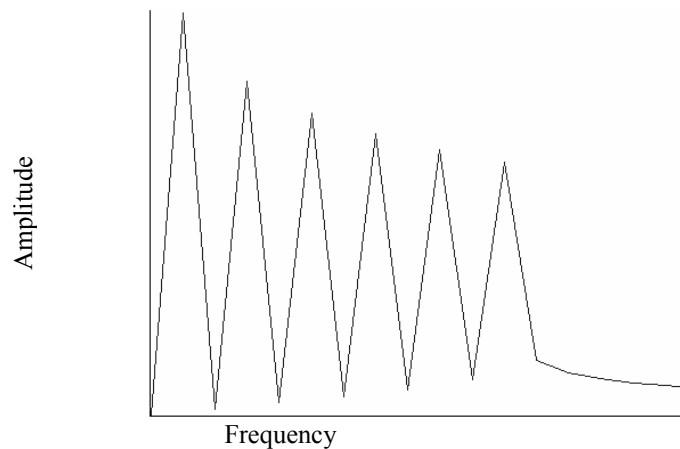


Figure 4-2. Frequency plot resulting from a Fourier transform on the signal in Figure 4-1a. Only the positive frequency is shown. Note that the plot is continuous.

4.1.1 FOURIER TRANSFORM COMPOSITION

The Fourier transform creates a complex representation of the input signal. This means the complex variable can be separated into its magnitude and phase angle. These hold different information in the Fourier transform. Figure 4-3¹ shows an image and then the Fourier transform of the image split into magnitude and phase components. In the Fourier transform figures, the center of the image represents 0 frequency going to higher frequency radially. The horizontal axis of the image corresponds to the horizontal axis of the transform.

The magnitude information, Figure 4-3B, contains information regarding how much of a certain frequency is in an image, with higher intensity pixels representing a more common frequency. As most images are made up of similar value pixels being close to each other (i.e. in Figure 4-3 most of the white pixels are next to other white pixels and likewise for

¹ The image used in Figure 3a, and multiple times throughout this chapter as an example figure, is a representation of an image from the computer game Minecraft [2]. This image was chosen because it is simple but is still unique in 2D space. The image was created using MATLAB.

the black pixels), there is a lot of low frequency information which is represented by the brighter center and dimmer edges of Figure 4-3B.

In order to display the magnitude information graphically, the formula

$$M = \log(|F| + 1) \quad (4-1)$$

is used in order to display all of the information in a meaningful way. M is the magnitude information that we want to display and F is the Fourier transform. A logarithm is used because without the log function the image will appear as simply a white dot on a black screen as the center dot is so much brighter than the rest. The $+ 1$ is used to prevent the log function from getting a 0 input.

The phase information, Figure 4-3C, contains information about where the frequencies lie in the image, literally how much of a phase shift each frequency must undergo. The phase plot is not normally shown when discussing Fourier transforms as it is difficult, if not impossible, to interpret graphically.

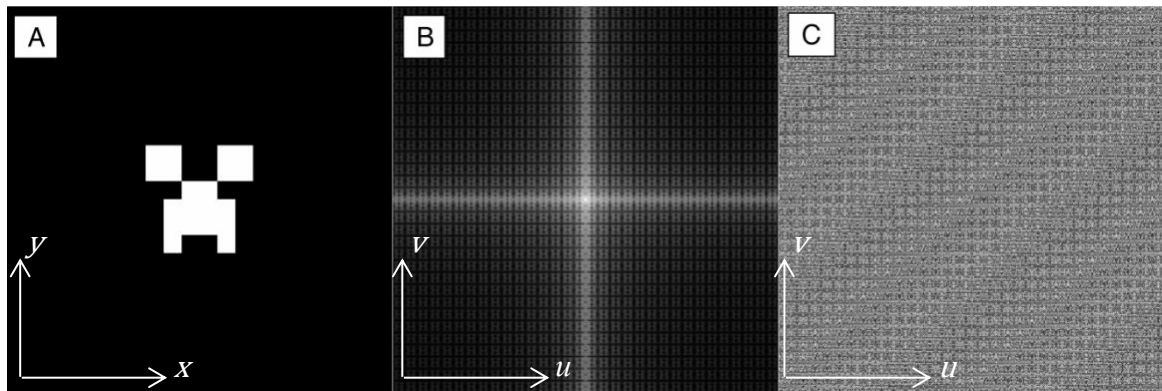


Figure 4-3. (A) Original image, (B) magnitude information, and (C) phase information. The frequency range of an axis is from $-N/2$ to $N/2$ where N is the size of the images axis.

4.1.2 FOURIER TRANSFORM DEFINITION

Consider a function f defined on the real plane \mathbf{R}^n , written as $f(\mathbf{x})$ with \mathbf{x} having components (x_1, x_2, \dots, x_n) . The Fourier transform will then convert the spatial domain \mathbf{x} to the spectral domain $\boldsymbol{\epsilon}$ with components $(\epsilon_1, \epsilon_2, \dots, \epsilon_n)$. Using Einsteinian notation with index n the Fourier transform can be written

$$F(\boldsymbol{\epsilon}) = \int_{\mathbf{R}^n} f(\mathbf{x}) e^{-i2\pi(\boldsymbol{\epsilon}_n \mathbf{x}_n)} d\mathbf{x} \quad (4-2)$$

Notice that the standard version of the Fourier transform is a continuous function over the entire domain.

A discrete version of the Fourier Transform is used for non-continuous functions,

$$F(\boldsymbol{\epsilon}) = \sum_{x_1}^{X_1-1} \sum_{x_2}^{X_2-1} \dots \sum_{x_n}^{X_n-1} f(\mathbf{x}) e^{-i2\pi\left(\frac{1}{X_n} \boldsymbol{\epsilon}_n \mathbf{x}_n\right)} \quad (4-3)$$

where X_i represents the number of discrete points in the i direction. The main difference between continuous and discrete transforms is the summation over the domain instead of integration and division by domain size (X_n) in the exponential function. The discrete version is used in general computing and all the same, properties hold for both the discrete and non-discrete Fourier transform. The continuous and discrete Fourier Transforms are also separable, allowing for a mix of transformed and non-transformed variables in a single domain if desired. The frequency range for the Fourier Transform goes from $-X_n/2$ to $X_n/2$ in the n dimension, where X_n is the number of samples for the n dimension (i.e. an image with 100 pixels in the x_1 direction would have ϵ_1 values ranging from -50 to 50).

Substituting $x_1 = x$, $x_2 = y$, $x_3 = z$ and $\varepsilon_1 = u$, $\varepsilon_2 = v$, $\varepsilon_3 = w$, the 3-D discrete version of the transform is

$$F(u, v, w) = \sum_x^{X-1} \sum_y^{Y-1} \sum_z^{Z-1} f(x, y, z) e^{-i\left(\frac{2\pi}{X}ux + \frac{2\pi}{Y}vy + \frac{2\pi}{Z}wz\right)} \quad (4-4)$$

where $F(u, v, w)$ is the Fourier transform of $f(x, y, z)$, x, y, z are the spatial coordinates of the image and u, v, w are the frequency coordinates of the Fourier domain. The following notation will be used

$$F(u, v, w) = \mathcal{F}_{3D}[f(x, y, z)](u, v, w) \quad (4-5)$$

which states that $F(u, v, w)$ is the 3D Fourier transform of $f(x, y, z)$.

The Fourier transform has multiple useful properties for analysis. Two properties of the Fourier Transform are translational invariance and rotation preservation. Both of these properties are proved to be valid for a 3D case in section 4.2, they will also be shown graphically for a 2D case. A technique that uses Fourier transforms known as phase correlation is also derived in section 4.2. This technique finds the shift in space between an object and a unique piece of the object.

4.2 PROPERTIES AND TECHNIQUES USING FOURIER TRANSFORMS

Many properties of Fourier transforms are useful for image registration. The most relevant properties are translational invariance and rotation preservation. The phase correlation technique takes advantage of Fourier transforms properties to obtain the differences in translation between a piece of an object and the full object.

4.2.1 TRANSLATIONAL INVARIANCE

Translational invariance means that regardless of an object location in the spatial domain, the magnitude of the Fourier transform of the object will be identical. This means that the magnitude of the FT can be used to compare objects regardless of its spatial location.

If $F(u, v, w)$ is the Fourier transform of signal $f(x, y, z)$, and if

$$f_{x_0y_0z_0}(x, y, z) = f(x - x_0, y - y_0, z - z_0) \quad (4-6)$$

Then using the property of Fourier transforms that

$$\mathcal{F}_{3D}[\delta(x - x_0, y - y_0, z - z_0)] = e^{-i2\pi(\frac{ux_0}{X} + \frac{vy_0}{Y} + \frac{wz_0}{Z})} \quad (4-7)$$

It can be determined, using the Fourier Transform shift theorem, that

$$\mathcal{F}_{3D}[f_{x_0y_0z_0}(x, y, z)](u, v, w) = F(u, v, w)e^{-i2\pi(\frac{ux_0}{X} + \frac{vy_0}{Y} + \frac{wz_0}{Z})} \quad (4-8)$$

Using the following identities

$$|ab| = |a||b| \quad (4-9)$$

$$|e^{ig}| = 1 \quad (4-10)$$

where g is any real function. It is straightforward to show that for the magnitude spectrum

$$|\mathcal{F}_{3D}[f_{x_0y_0z_0}(x, y, z)](u, v, w)| = |F(u, v, w)| \quad (4-11)$$

For the phase spectrum

$$\angle \mathcal{F}_{3D}[f_{x_0y_0z_0}(x, y, z)](u, v, w) = \angle F(u, v, w) - 2\pi(\frac{ux_0}{X} + \frac{vy_0}{Y} + \frac{wz_0}{Z}) \quad (4-12)$$

The magnitude spectrum of the 3 dimensional Fourier Transform is therefore unaffected by translational shifts in the spatial domain.

Figure 4-4 shows the change that happens to the magnitude spectrum of an object when it is translated before the Fourier transform is taken.

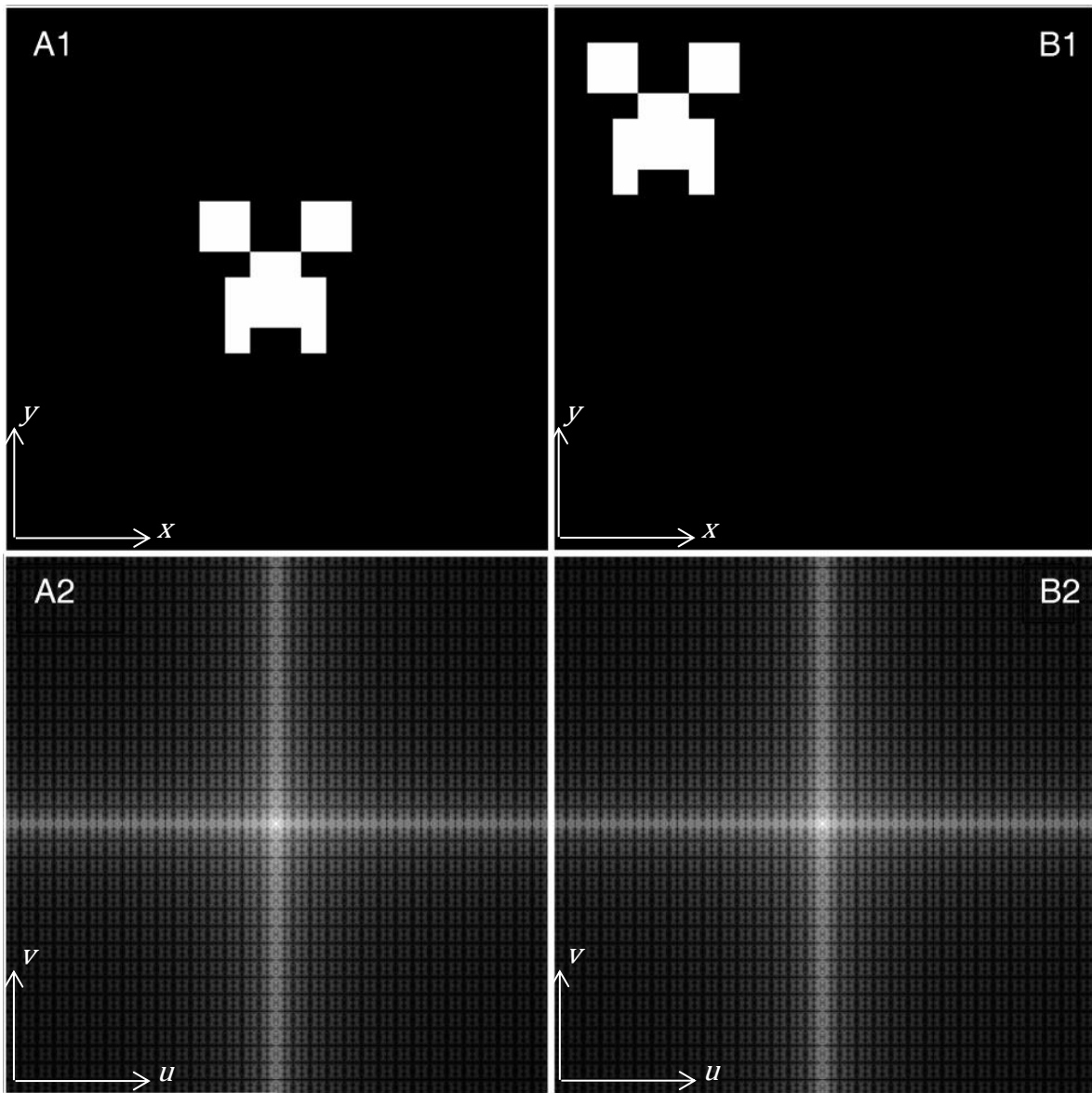


Figure 4-4. The Fourier transform of an image compared to Fourier transform of same image with translation. A2 is the Fourier transform of A1, likewise for B. A2 and B2 are identical.

4.2.2 ROTATION PRESERVATION

A general technique of representing a rotation is to apply a stretch deformation operation to a volume or image. In terms of the Fourier transform a stretch is applied according to the following formula [3]

$$\mathcal{F}_{3D}(f(\mathbf{Ax})) = \frac{1}{|\det \mathbf{A}|} F((\mathbf{A}^{-T}\boldsymbol{\epsilon})) \quad (4-13)$$

where \mathbf{A} is the matrix acting on the Cartesian space \mathbf{x} and $\boldsymbol{\epsilon}$ is the created space in the frequency domain. In the special case that \mathbf{A} is an orthogonal rotation matrix the following properties also hold true

$$\mathbf{AA}^T = \mathbf{I} \quad (4-14)$$

$$\mathbf{A}^{-T} = (\mathbf{A}^{-1})^T = (\mathbf{A}^T)^T = \mathbf{A} \quad (4-15)$$

$$\det \mathbf{A} = \pm 1 \quad (4-16)$$

where \mathbf{A}^T is the transpose of \mathbf{A} , and \mathbf{I} is the identity matrix. These properties simplify equation (4-13) to

$$\mathcal{F}_{3D}(f(\mathbf{Ax})) = F((\mathbf{A}\boldsymbol{\epsilon})) \quad (4-17)$$

Equation (4-17) demonstrates that a rotation of the Cartesian space results in the identical rotation in the frequency domain. This applies regardless of the number of rotations involved as the product of two orthogonal matrices is an orthogonal matrix. The caveat is to remember that matrix multiplication is non-commutative in three (or greater) dimension. Figure 4-5 shows a 20 degree rotation counter-clockwise (CCW) in the spatial domain that results in a 20° CCW rotation in the Fourier magnitude as well.

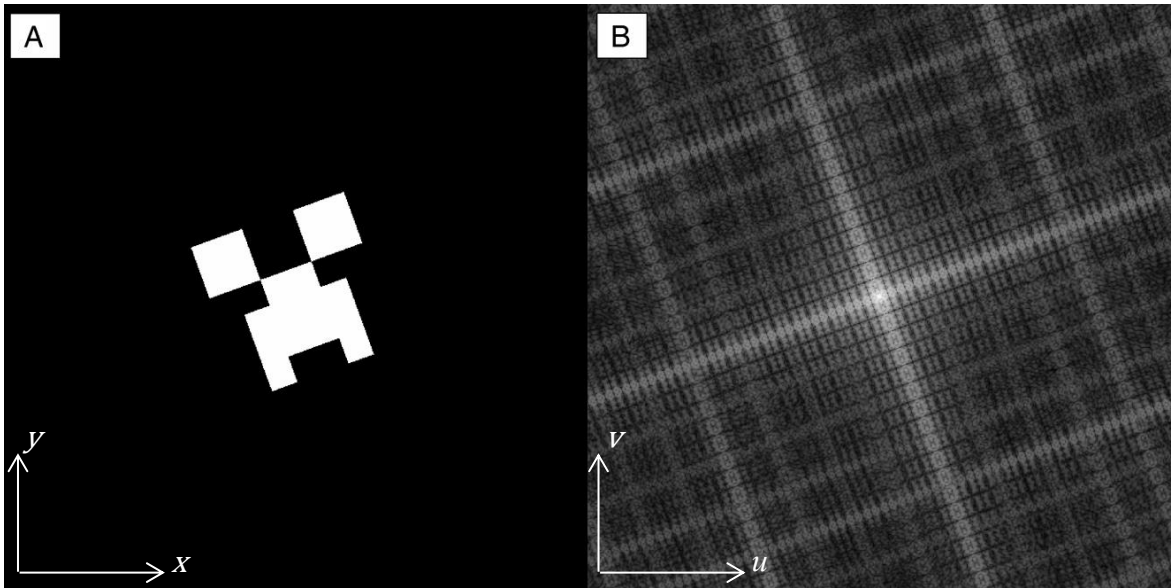


Figure 4-5. Since sub-figure A is rotated CCW by 20° the Fourier transform of the image is also rotated CCW by 20° .

4.2.3 PHASE CORRELATION METHOD FOR COMPARING TWO IMAGES

Phase correlation is a technique for comparing large images by finding differences due to translation. This technique requires two images of the same size, and similar except for a translation and potential cropping as input. Figure 4-6 shows two images that would be ideal for comparing to a “gold standard” (Figure 4-6A).

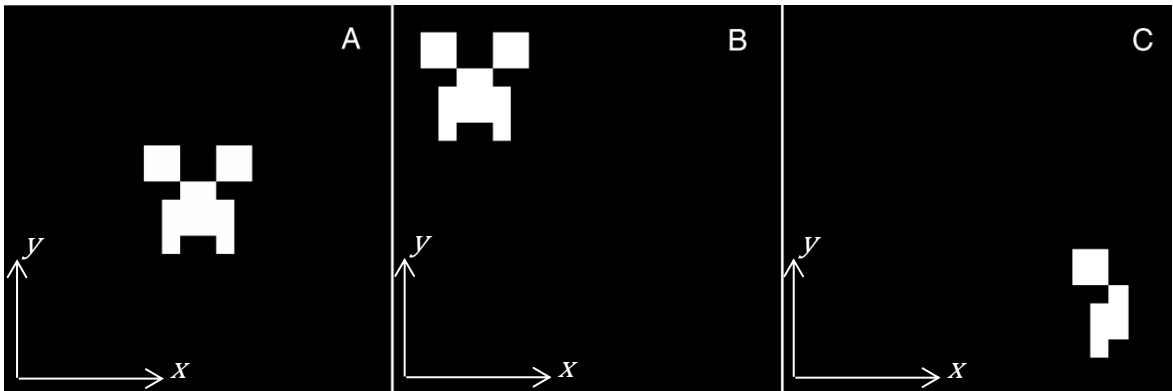


Figure 4-6. (A) “Gold-standard” image, images (B) and (C) are ideal candidates for phase correlation registration. The cropping of an image does not affect phase correlation as long as it fits uniquely in the “gold standard” image.

Define the gold standard image as $f(x, y, z)$ and the shifted image as $f_{\text{shift}}(x, y, z)$. Taking the Fourier Transforms of the two images yields

$$F(u, v, w) = \mathcal{F}_{3D}[f(x, y, z)](u, v, w) \quad (4-18)$$

$$F_{\text{shift}}(u, v, w) = \mathcal{F}_{3D}[f_{\text{shift}}(x, y, z)](u, v, w) \quad (4-19)$$

Phase correlation is then defined as

$$R(u, v, w) \equiv \frac{F(u, v, w) \circ F_{\text{shift}}(u, v, w)^*}{|F(u, v, w) \circ F_{\text{shift}}(u, v, w)^*|} \quad (4-20)$$

where $*$ is the complex conjugate operator and \circ represent the Hadamard product. The Hadamard product (also known as the entrywise product) mathematically is

$$(A \circ B)_{ijk} = A_{ijk} \cdot B_{ijk} \quad (4-21)$$

for any matrices A and B with identical size. Typically, the subscript ijk on the right side of equation (4-21) is not shown. The Hadamard product is not defined for matrices of different sizes.

Recalling from section 4.2.1,

$$F_{\text{shift}}(u, v, w) = F(u, v, w) e^{-i2\pi(\frac{ux_0}{X} + \frac{vy_0}{Y} + \frac{wz_0}{Z})} \quad (4-22)$$

where x_0 , y_0 , and z_0 are the translations in each direction between the two images and $F(u, v, w)$ is the “gold-standard” image. For complex conjugates the same relation holds though the negative sign is removed on the exponential term, i.e.,

$$F_{\text{shift}}(u, v, w)^* = F(u, v, w)^* e^{i2\pi(\frac{ux_0}{X} + \frac{vy_0}{Y} + \frac{wz_0}{Z})} \quad (4-23)$$

Substituting the results of equations (4-22) and (4-23) in equation (4-20) yields

$$R(u, v, w) = \frac{F(u, v, w) \circ F(u, v, w)^* e^{i2\pi(\frac{ux_0}{X} + \frac{vy_0}{Y} + \frac{wz_0}{Z})}}{\left| F(u, v, w) \circ F(u, v, w)^* e^{i2\pi(\frac{ux_0}{X} + \frac{vy_0}{Y} + \frac{wz_0}{Z})} \right|} \quad (4-24)$$

Using the identities in equations (4-9) and (4-10) in section 4.2.2, equation (4-24) is further simplified to

$$R(u, v, w) = \frac{F(u, v, w) \circ F(u, v, w)^* e^{i2\pi(\frac{ux_0}{X} + \frac{vy_0}{Y} + \frac{wz_0}{Z})}}{|F(u, v, w) \circ F(u, v, w)^*|} \quad (4-25)$$

Using the identity

$$|F \circ F^*| = F \circ F^* \quad (4-26)$$

results in

$$R(u, v, w) = e^{i2\pi(\frac{ux_0}{X} + \frac{vy_0}{Y} + \frac{wz_0}{Z})} \quad (4-27)$$

The inverse discrete Fourier transform can then be taken of $R(u, v, w)$. The basic identity of discrete Fourier transforms states that

$$\mathcal{F}^{-1} \left[e^{i2\pi(\frac{ux_0}{X} + \frac{vy_0}{Y} + \frac{wz_0}{Z})} \right] = \delta(x + x_0, y + y_0, z + z_0) \quad (4-28)$$

This means that the equation (4-27) can be inverse Fourier transformed as

$$\begin{aligned} \mathcal{F}_{3D}^{-1}[R(u, v, w)] &= \mathcal{F}_{3D}^{-1} \left[e^{i2\pi(\frac{ux_0}{X} + \frac{vy_0}{Y} + \frac{wz_0}{Z})} \right] = r(x, y, z) \\ &= \delta(x + x_0, y + y_0, z + z_0) \end{aligned} \quad (4-29)$$

where δ is the Kronecker delta translated to have a value of 1 at location (x_0, y_0, z_0) . This results shows that the shift between two images can be obtained by plotting the phase correlation function and finding the value where the function is maximum. Figure 4-7 shows an example of phase correlation on Figure 4-6A and Figure 4-6B. The location of the maximum value of r is the translation required for the best matching between the image to be registered and the “gold-standard”. The proof is applicable to the ideal case where the images are identical except for a shift.

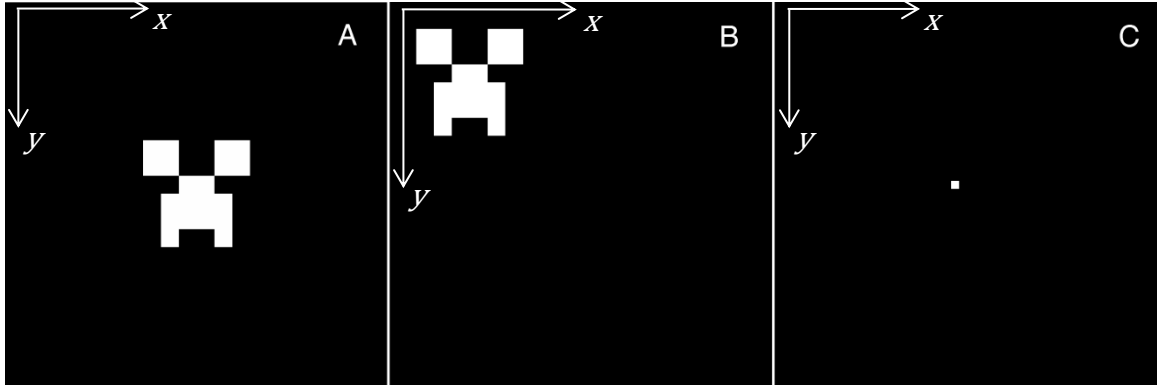


Figure 4-7. Sub-figure A and B are identical except for a shifting of -200 pixels in sub-figure B. Figure C is a zoomed in view of the resulting cross correlation produced using equation 23. The white dot corresponds to location (201,201) meaning sub-figure B lags (is behind) sub-figure A by 200 pixels in each direction. Note the location is (201,201) since the cross correlation was produced using Matlab which indexes from 1, i.e. a location of (1, 1) would mean a shift of 0 pixels in both dimensions). In sub-figures A and B the upper left corner of the image is the origin, in sub-figure C the upper left corner is location (175,175) and the lower right corner is location (225,225).

4.3 REGISTRATION IMPLEMENTATION

Registration is an important technique in medical imaging. The ability to overlap two images allows a researcher or clinician to visually assess changes that may have occurred with time, or treatment. The increasing use of 3D imaging using equipment, such as CBCT, is driving the importance of three-dimensional superimposition. Three-dimensional superimposition is difficult due to having six degrees of freedom (three rotations, three translations). This is contrasted with 2D superimposition only having three degrees of freedom (one rotation and two translations). This section will outline the steps and implementation for a new registration algorithm, using the techniques described in section 4.2.

The registration method introduced here is similar to the 2D registration Fourier-Mellin method [1]. The 2D registration method uses Fourier transforms to remove the translations then converts the image to log-polar coordinates to allow rotation to be found. Since the image is only 2D there is only one rotation to account for. Log-polar is used as the logarithm allows for differences in scale to be found between the images being registered. The new technique presented here also uses the Fourier transform to remove the translation, but then cylindrical coordinates are used to assist in finding rotations. The logarithm is not used since scale does not need to be accounted for in CBCT images. The scale is known when the scan is taken and is saved as metadata attached to the image. If required images can be resampled to the same voxel size prior to registration.

Bican and Flusser, and, Nakamori, Okabayahi and Kawanaka presented similar techniques that use phase correlation and cylindrical transformations [5, 6]. Algorithm 1 is the algorithm for the registration method. This technique is common in 2D systems where only a single rotation axis exists. In section 4.5 a visual example of the registration technique is shown.

Algorithm 4-1. Superimposition of two 3D volumes using phase correlation and cylindrical transformations. Steps shown in [] are optional steps from section 4.4

Read in volume 1 (gold standard);

Read in volume 2 (image to register);

[Threshold both images;]

[Hamming window both images;]

3D Fourier transform both images;

[High-pass filter both images;]

Iteration = 0 and Rotations = (1, 1, 1)

while rotations about (x,y,z) axis \neq (0,0,0)

for $i = 1$ to 3

 Convert the Fourier transform of both images to cylindrical coordinates with axis i as the z-axis

 Calculate the phase correlation of the two images

 Find the location of the maximum of the phase correlation

 Convert the maximum to an angular measure θ

 If $\theta > 180$ then $\theta = \theta - 180$

 Rotate image to be registered about i axis by θ

 Rotation(i) = θ

end

iteration = iteration +1

end

Perform phase correlation on the rotation-corrected image and the gold standard

In this chapter the “gold-standard” image is f and the image to be registered is g . The only difference between the “gold-standard” and registering image are a rotation R and a translation T .

$$g \cong RTf \quad (4-30)$$

where R is an arbitrary orthogonal rotation matrix. A rotation matrix takes the form

$$R = \begin{bmatrix} R_1 & R_2 & R_3 & 0 \\ R_4 & R_5 & R_6 & 0 \\ R_7 & R_8 & R_9 & 0 \\ 0 & 0 & 0 & 1 \end{bmatrix} \quad (4-31)$$

where the values R_{1-9} define a rotation about the origin of a three dimensional volume. Any rotation applied to a volume can then be undone by applying the inverse of the rotation matrix

$$RR^{-1} = I \quad (4-32)$$

T in equation (4-30) is a pure translation matrix. A pure translation matrix is

$$R = \begin{bmatrix} 1 & 0 & 0 & t_x \\ 0 & 1 & 0 & t_y \\ 0 & 0 & 1 & t_z \\ 0 & 0 & 0 & 1 \end{bmatrix} \quad (4-33)$$

where t_x , t_y , and t_z are translations in the $x y z$ directions. Both translation and rotation matrices (M) are applied to an image as

$$\begin{bmatrix} x' \\ y' \\ z' \\ 1 \end{bmatrix} = [M] \begin{bmatrix} x \\ y \\ z \\ 1 \end{bmatrix} \quad (4-34)$$

4.3.1 FOURIER TRANSFORM OF 3D VOLUMES

The first step of the registration method is to take the Fourier transform of the “gold-standard” and image to register, i.e.,

$$\mathbf{F} = \mathcal{F}_{3D}[\mathbf{f}(x, y, z)](u, v, w) \quad (4-35)$$

$$\mathbf{G} = \mathcal{F}_{3D}[\mathbf{g}(x, y, z)](u, v, w) \quad (4-36)$$

Only the magnitude information is of any interest, therefore the phase information is discarded. Translational invariance and rotation preservation properties imply that the magnitudes of \mathbf{F} and \mathbf{G} are related through a rotation matrix, i.e.,

$$|\mathbf{G}| \cong \mathbf{R}|\mathbf{F}| \quad (4-37)$$

4.3.2 CONVERSION TO CYLINDRICAL SPACE

In order to use a phase correlation to recover the desired rotation, the rotation must be converted into a translation. Cylindrical coordinates allows for this to be done. Defining the cylindrical coordinates as shown in Figure 4-8 [7],

$$\begin{bmatrix} \rho \\ \varphi \\ z \end{bmatrix} = \begin{bmatrix} \sqrt{x^2 + y^2} \\ \text{atan2}\left(\frac{y}{x}\right) \\ z \end{bmatrix} \quad (4-38)$$

where atan2 is the inverse tan function defined to always be between $-\pi$ and π . To convert cylindrical coordinates back to Cartesian

$$\begin{bmatrix} x \\ y \\ z \end{bmatrix} = \begin{bmatrix} \rho \cos(\varphi) \\ \rho \sin(\varphi) \\ z \end{bmatrix} \quad (4-39)$$

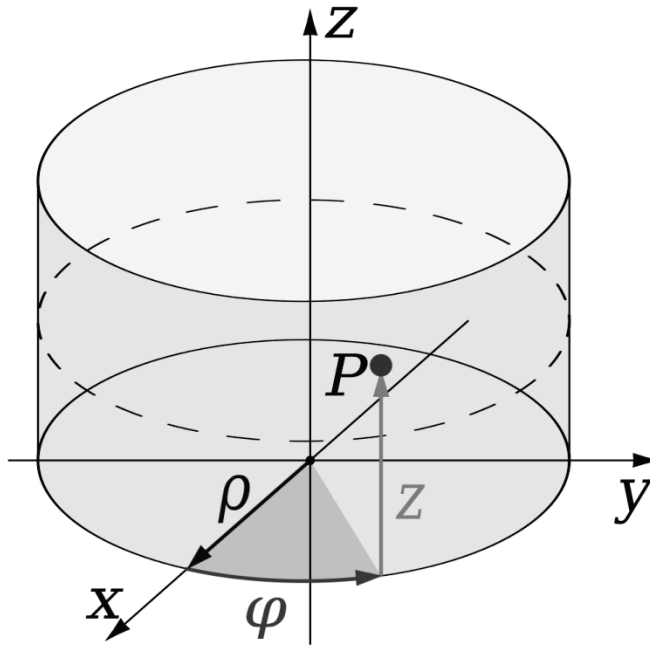


Figure 4-8. Superimposition of the cylindrical coordinate system over the Cartesian coordinate system. The z-axis is the same for both coordinate systems. Adapted from [7].

The images $|\mathbf{G}|$ and $|\mathbf{F}|$ are converted to cylindrical coordinate

$$|\mathbf{F}(\rho, \varphi, z)| = |\mathbf{F}(x(\rho, \varphi, z), y(\rho, \varphi, z), z(\rho, \varphi, z))| \quad (4-40)$$

$$|\mathbf{G}(\rho, \varphi, z)| = |\mathbf{G}(x(\rho, \varphi, z), y(\rho, \varphi, z), z(\rho, \varphi, z))| \quad (4-41)$$

converted using equation (4-38).

By converting to cylindrical space the rotation about a single axis is represented by a translation represented as

$$(x, y, z) \rightarrow (r, \varphi + \Delta\varphi, z) \quad (4-42)$$

Figure 4-9 is a 2D representation of an image in the spatial domain and the conversion into the cylindrical domain. The figure also shows how a rotation in the spatial domain becomes a shift in the cylindrical domain.

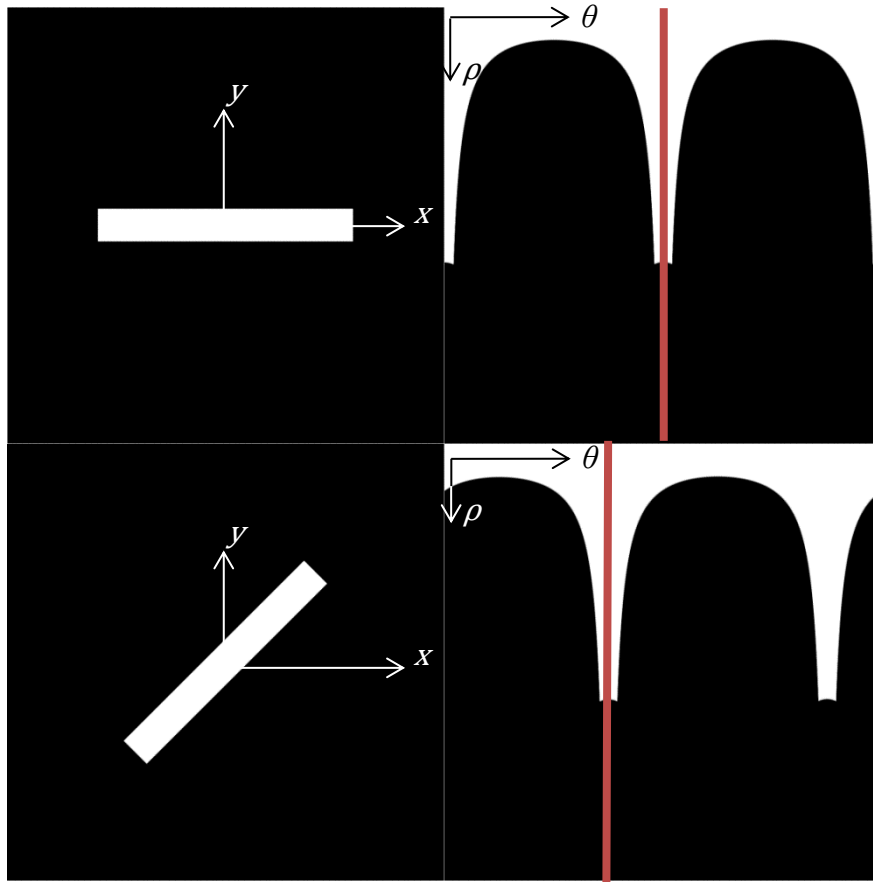


Figure 4-9. The top set of images are the Cartesian (left) and polar representation of the same image (x-axis represents phi and y-axis represents rho). The image is then rotated in the spatial domain 45°, resulting in a translation in the cylindrical representation (phi axis shift). The red line shows the shift between the images.

4.3.3 PHASE CORRELATION

Once the rotation about a single axis of the image has been converted to a translation, phase correlation can be performed. Phase correlation is used to find the shift in the φ axis between $|G|$ and $|F|$ as discussed previously. The phase correlation function finds a shift in the number of voxels to make two images equal. This shift in polar/cylindrical coordinates is then converted to a rotation in the spatial domain using

$$\varphi = (S - 1) \frac{360}{N} \tag{4-43}$$

where N is the number of voxels in the φ direction and S is the shift found using the phase correlation in number of voxels. Equation (4-43) calculates the number of degrees

represented by each voxel of shift, then multiplies it by the shift found (a shift of one voxel corresponds to no shift as Matlab indexes from 1).

4.3.4 COMPENSATE FOR ROTATION

The rotation found in the phase correlation is applied to the original volume \mathbf{g} bringing one plane into alignment with the gold standard image \mathbf{f} . The transformation matrix used is

$$\mathbf{R} = \begin{bmatrix} \cos \Delta\varphi & -\sin \Delta\varphi & 0 & 0 \\ \sin \Delta\varphi & \cos \Delta\varphi & 0 & 0 \\ 0 & 0 & 1 & 0 \\ 0 & 0 & 0 & 1 \end{bmatrix} \quad (4-44)$$

where the axis of rotation corresponds to the z-axis of the cylindrical coordinate, and the corresponding axis in the spatial coordinates.

4.3.5 REPETITION OF THE ROTATIONS

After the first rotation has been performed, steps 4.3.1 to 4.3.5 are repeated two more times with different rotation axis. This first rotation is done about the z-axis in the rotation domain, the second rotation about the x-axis, and the third rotation about the y-axis. All three of these rotations create a single iteration of the registration method.

The iterations described above are repeated until a full iteration containing all rotations of 0° for all dimensions. This results in a rotational alignment of the images in the spatial domain. Symbolically this means

$$\tilde{\mathbf{g}} \cong \mathbf{T}\mathbf{f} \quad (4-45)$$

where $\tilde{\mathbf{g}}$ is the image to be registered after all of the rotations have been performed.

4.3.6 PHASE CORRELATION TO FIND TRANSLATION DIFFERENCES

Since the only difference between the gold-standard and registration image is now a translation, a phase correlation can be performed to obtain the optimal translation. Since the phase correlation is now for a translation, no further image manipulation is required. The steps outlined in section 4.2.4 can therefore be used.

4.3.7 APPLY TRANSLATION MATRIX TO \tilde{g}

Applying the translations found in section 4.3.6 to volume \tilde{g} , the image is fully registered, i.e.,

$$\tilde{g} \cong f \quad (4-46)$$

where \tilde{g} is the final image, after the translation found using the phase correlation is performed. At this point, the registration of the images is complete.

4.4 TECHNIQUES FOR IMPROVING PHASE CORRELATION

There are multiple techniques for improving phase correlation. Many of the techniques are commonly used in 1D signals and 2D images; however, they can be extended to work in three dimensions. Three techniques are discussed in this section: windowing, filtering, and thresholding. All three techniques have an effect on the volumes being superimposed. For this reason, the techniques used for windowing and thresholding are standard methods that are good for most common cases and do not need to be changed. The strength of the filter may need to change depending on the volumes superimposed. Thresholding may not be required or even desirable depending on the types of images being superimposed, this should be tested using sample data before being implemented for a consistent data type (such as the cranial base of a human skull).

4.4.1 FILTERING

Filtering is commonly used with Fourier Transforms. This is because a large amount of pixels in an image will have a similar value, resulting in high amplitudes in the low frequency information of the Fourier transform. There are three types of filters, high-pass, low-pass, and band-pass. A high-pass filter will remove the low frequency information from an image accentuating the areas of large change in voxel value, such as edges. A low pass filter removes the high frequency information including image noise and edge information, making the image appear blurry. Low pass filters are also referred to as smoothing filters. Band pass filters combine a low and a high pass filter preserving a *band* of the frequency information. The different filter types, and the effect of each filter on a 2D static image, are shown below in Figure 4-10. The appearance of extra lines in the high-pass and band-pass filtered images are ringing artifacts caused by the ideal filter.

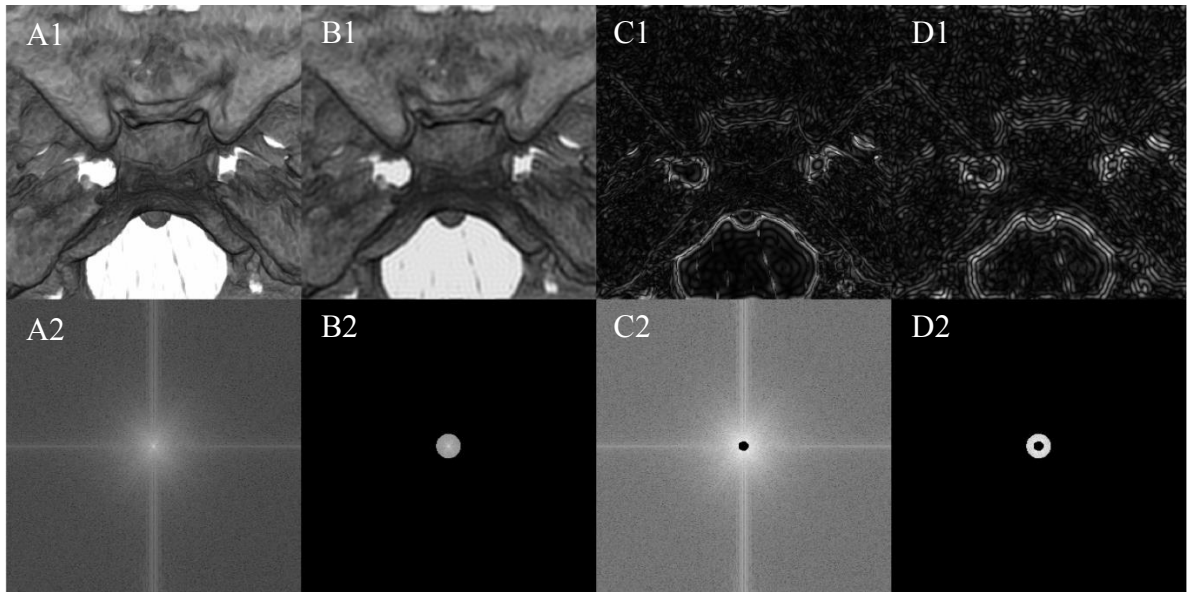


Figure 4-10. The top images are the results of running a(n) (in order left to right): no filter (A), ideal low-pass filter (B), ideal high-pass filter (C), and ideal band-pass filter (D). The bottom image is the corresponding magnitude of the Fourier Transform for each image. There are ringing artifacts visible in C and D around the high frequency areas.

For the superimposition algorithm, a high pass filter will often improve the results of the superimposition because it removes the bright spot at the center of the FTs and increases the effect of edge material on the FT (effectively removing small variations in background air and bone). The bright spot at the center of the Fourier transform creates a secondary peak in the phase correlation after the cylindrical transform is used, increasing the error of the phase correlation [8].

For the registration method a Gaussian high-pass filter is used. A Gaussian high-pass filter applies a Gaussian curve over the image with a value of 0 at the center of the image going to a value of 1 at the edges. Figure 4-11 shows the Gaussian high-pass filter applied to the original image in Figure 4-10. When the filtered image is viewed the ringing artifacts found in Figure 4-10 no longer exist.

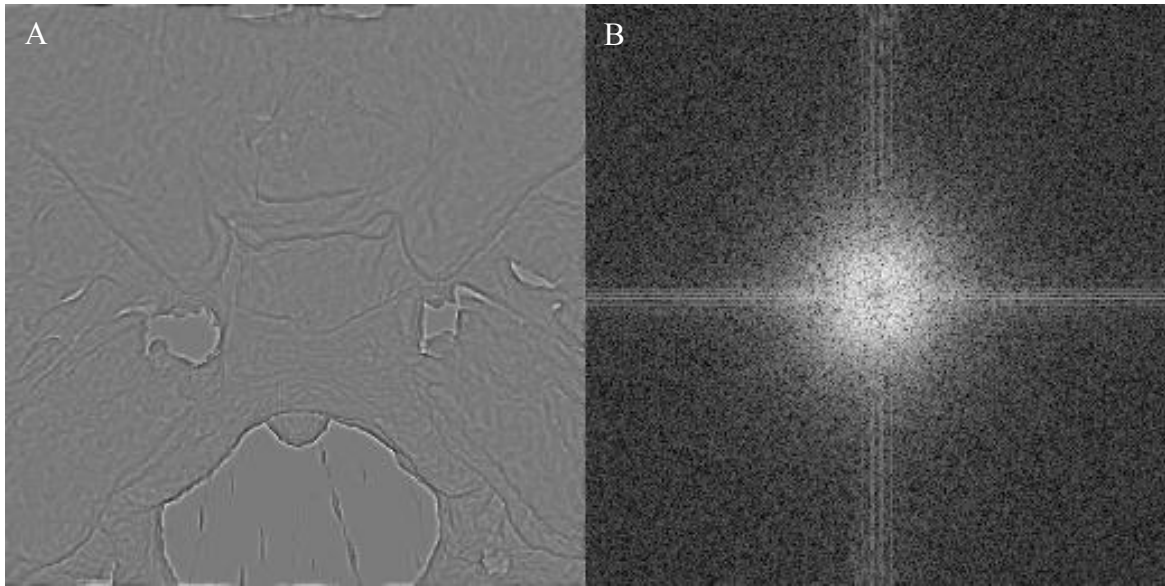


Figure 4-11. Image A is the Gaussian high-pass filtered of the original image in Figure 4-9. Notice that the ringing artifacts (appearing as halos) around the high frequency sections of the image are removed. Image B is the Gaussian filtered Fourier transform. The center bright dot has been removed without causing a large section of the image center being reduced to 0.

A standard 3-D Gaussian filter in the frequency domain is given by

$$H(u, v, w) = 1 - e^{\frac{-(u^2+v^2+w^2)}{2\sigma^2}} \quad (4-47)$$

where u , v , w are the frequency variables in the Fourier domain, and σ defines the standard deviation of the Gaussian curve. To show the effect of σ on the filter, Figure 4-12 shows the Gaussian filter for different σ values in the frequency domain. This version of the filter is applied in the frequency domain using the Hadamard product (defined by equation (4-21) in section 4.2.3).

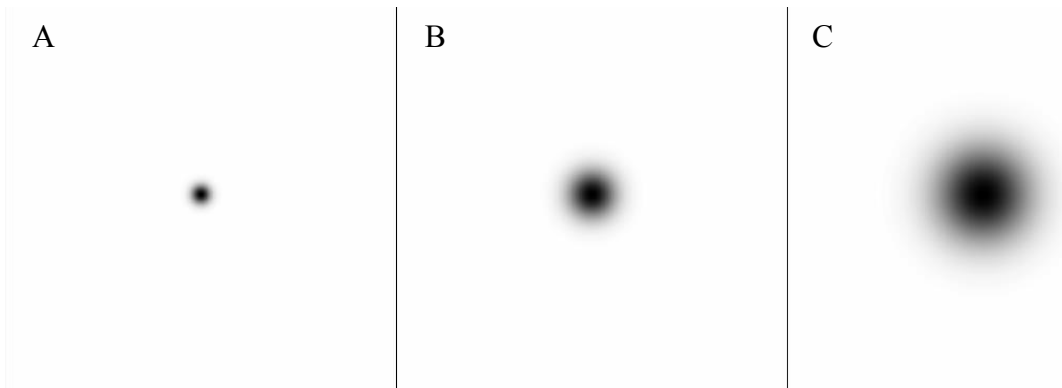


Figure 4-12. This figure shows the change in the response of the Gaussian high-pass filter with changing σ value. The sigma values (A) 20, (B) 50, and (C) 100.

For the registration method a Gaussian filter is used with a σ value of 80. This value was found to be optimal by experimentally testing the algorithm until it converged reliably.

4.4.2 *WINDOWING*

Windowing is a technique where a signal is eventually turned to zero outside a given interval. This technique is important in Fourier analysis since it prevents discontinuities. Discontinuities occur since a Fourier transform assumes a periodic domain, as shown in Figure 4-13. Since the image is assumed to be repeated, the edges of the image will have discontinuities and be interpreted as an area of very high frequency. This high frequency information will reduce the accuracy of the Fourier transform. A window function can be applied in the spatial domain using the Hadamard product to correct for this.

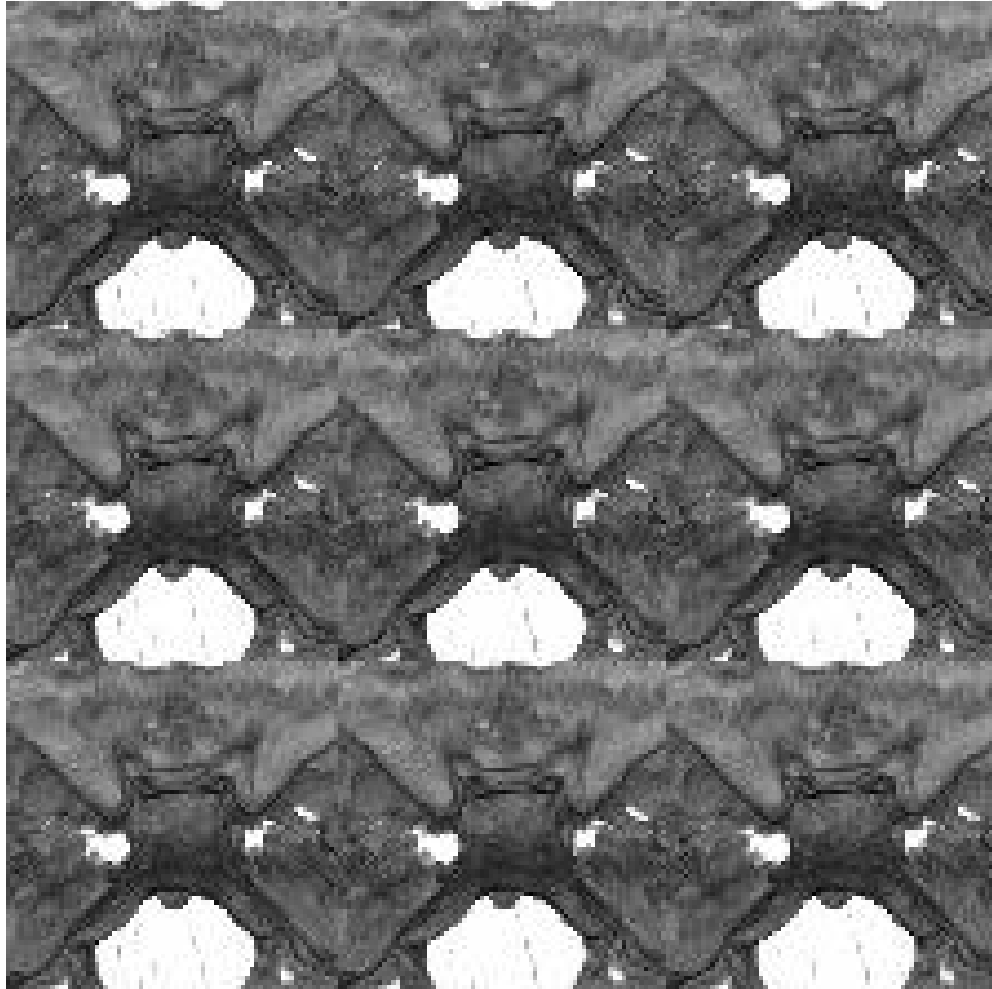


Figure 4-13. The periodic nature of the Fourier transform means the edges of the image are assumed to lead into the next image.

There are many types of window functions though they all serve the same purpose. The ideal window function is a rectangular window, shown in Figure 4-14 for 2 dimensions. An ideal window is not a good choice for image analysis though as the abrupt change in voxel value at the window changes the resulting Fourier transform. Instead, a much better choice of windowing function is the Hamming window. The ideal and Hamming windows are shown for 2D in Figure 4-14A and B. The Hamming window changes the voxel values slowly on the edges in order to limit any errors in the Fourier transform.

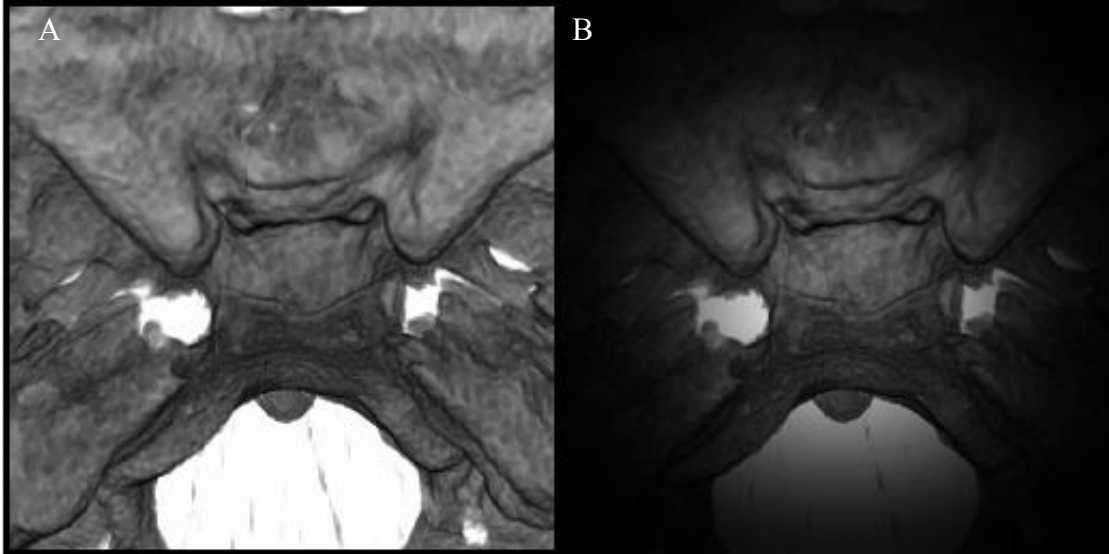


Figure 4-14. The periodic nature of the Fourier transform means the edges of the image are assumed to lead into the next image. A windowing function changes the edges of the image so that discontinuities do not occur at the image edges. Image A is an ideal window with the image edges converted to black and image B is the cranial base image with a hamming window.

The Hamming window is a separable function, so it is defined for a single dimension then applied to each dimension separately. The mathematical representation of the hamming window is

$$w(n) = \alpha - \beta \cos\left(\frac{2\pi n}{N-1}\right) \quad (4-48)$$

where N is the number of voxels in the image direction, n is the specific voxel that w is being computed for ($n = 0$ occurs as the origin, normally in the corner, of the image), and α and β are constants defined as

$$\alpha = 0.53836 \quad (4-49)$$

$$\beta = 0.46164 \quad (4-50)$$

4.4.3 THRESHOLDING

Thresholding is the technique of binarizing an image to remove image noise. A side effect of thresholding is that some image information will be lost. An example of thresholding is shown in Figure 4-15. There are many thresholding techniques. The technique used in this case is the Otsu method [9]. This was chosen for being a method with easy implementation that is available in many software suites.

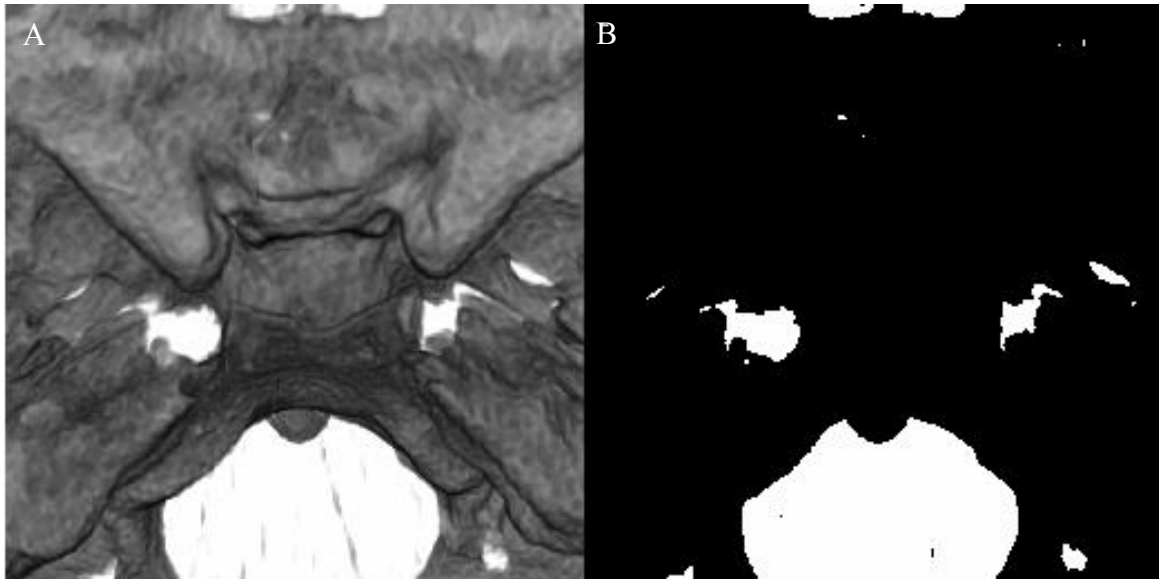


Figure 4-15. The Otsu thresholding method was able to separate the light and dark material pixels in the original image (A) to create thresholded image (B).

The Otsu method works by assuming a mainly bi-modal histogram of background values and foreground values. It then calculates the optimum threshold separating the two classes so that the intra-class variance is minimized. An in-depth description at the mathematics behind the Otsu method can be found in reference [8].

The Otsu method works well for this implementation as the foreground material is distinct from the background material and the image is truly bi-modal (background air material and foreground bone material).

4.5 REGISTRATION VALIDATION USING A STANDARD SHAPE

This section contains a full set of figures illustrating a full run through of the superimposition method.

4.5.1 GOLD-STANDARD AND THE IMAGE TO BE REGISTERED

Figure 4-16 shows the images before any registration occurs. The red volume is the “gold-standard” volume and the blue volume is the volume to be registered. The difference between the images is a combination of rotations and translations, shown in Table 4-1.

Table 4-1. The initial error in rotation and translation between the gold-standard and registering image.

	x	y	z
Rotations about axis (°)	-12.6	13.9	8.8
Translations in dimension (voxel)	-9	-12	10

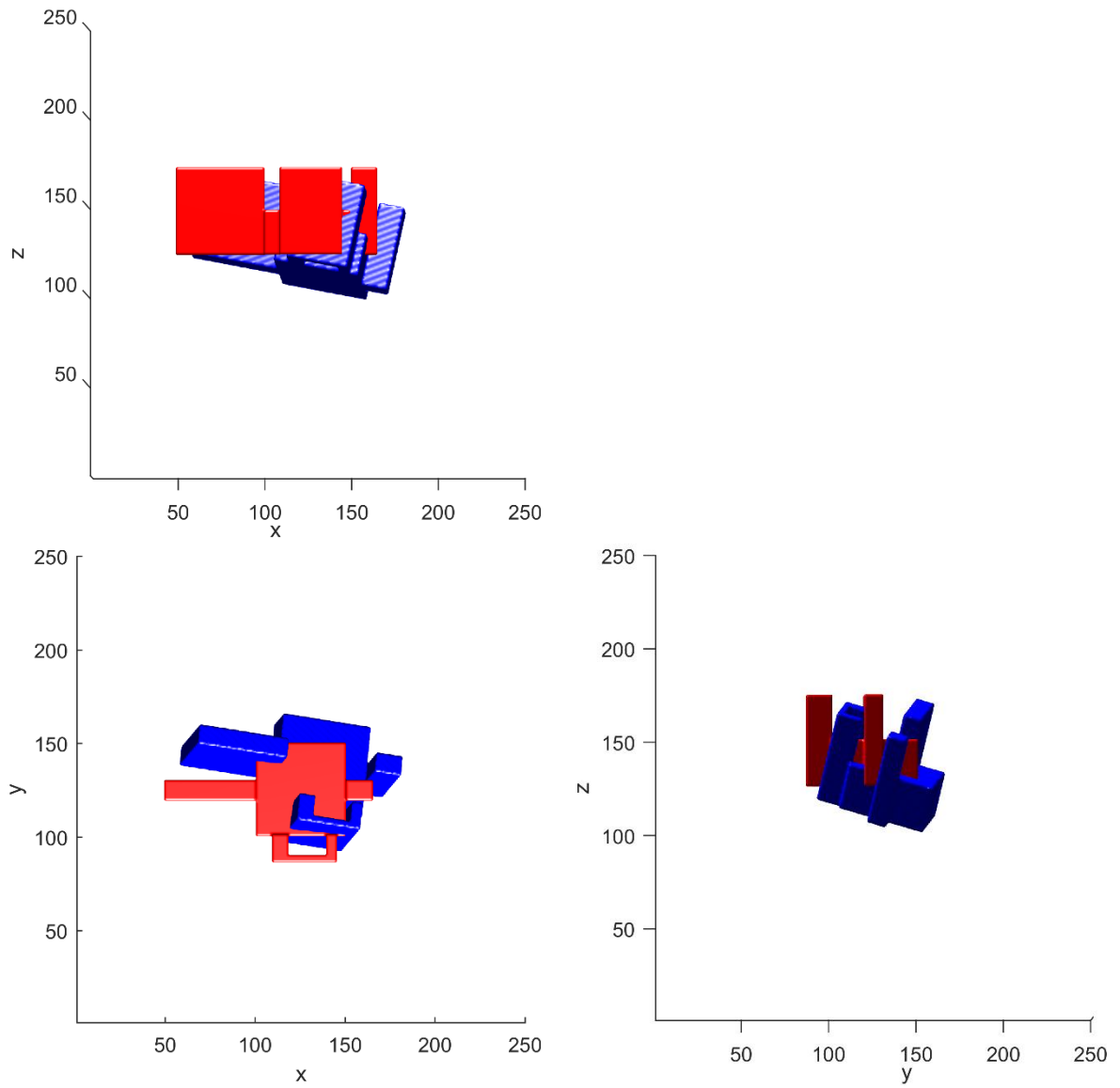


Figure 4-16. The red volume is the gold standard and the blue volume is the volume to be registered. The amount of error is given in Table 4-1

4.5.2 THE 1ST ITERATION

The raw images are first read into the algorithm. Then, the first iteration performed. The order the rotations is first the z-axis, then y-axis, and finally x-axis. Figures 4-17 to 4-19 show the result on the two volumes after each rotation.

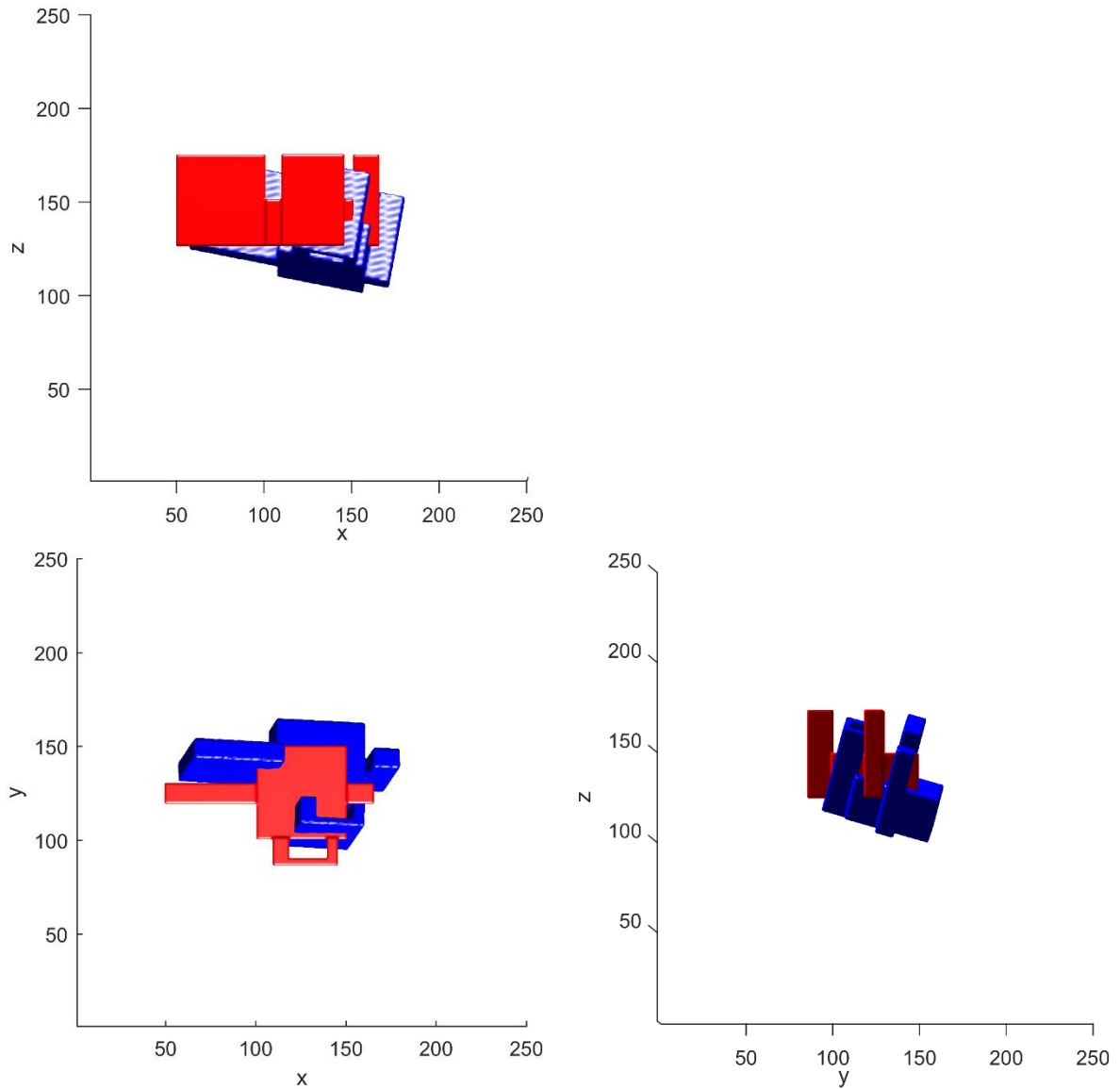


Figure 4-17. The blue volume has undergone a rotation about the z-axis of 5.76° after the first rotation of the first iteration.

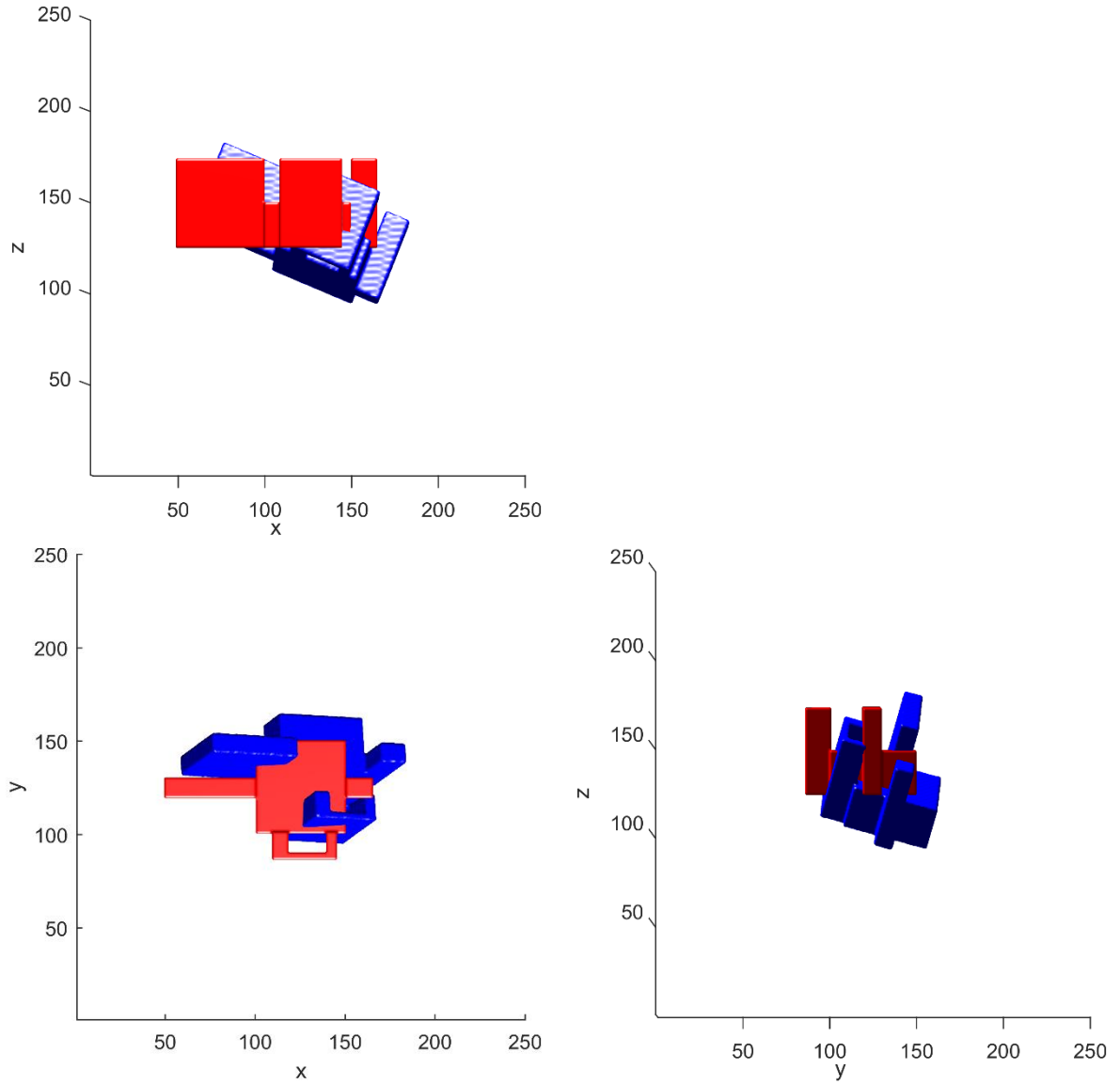


Figure 4-18. The blue volume has now undergone a rotation in the y axis of 15.84° . It may appear that the rotation is causing increasing error and this is correct. This optimization will sometimes increase the error and it will then be corrected for with the next iteration.

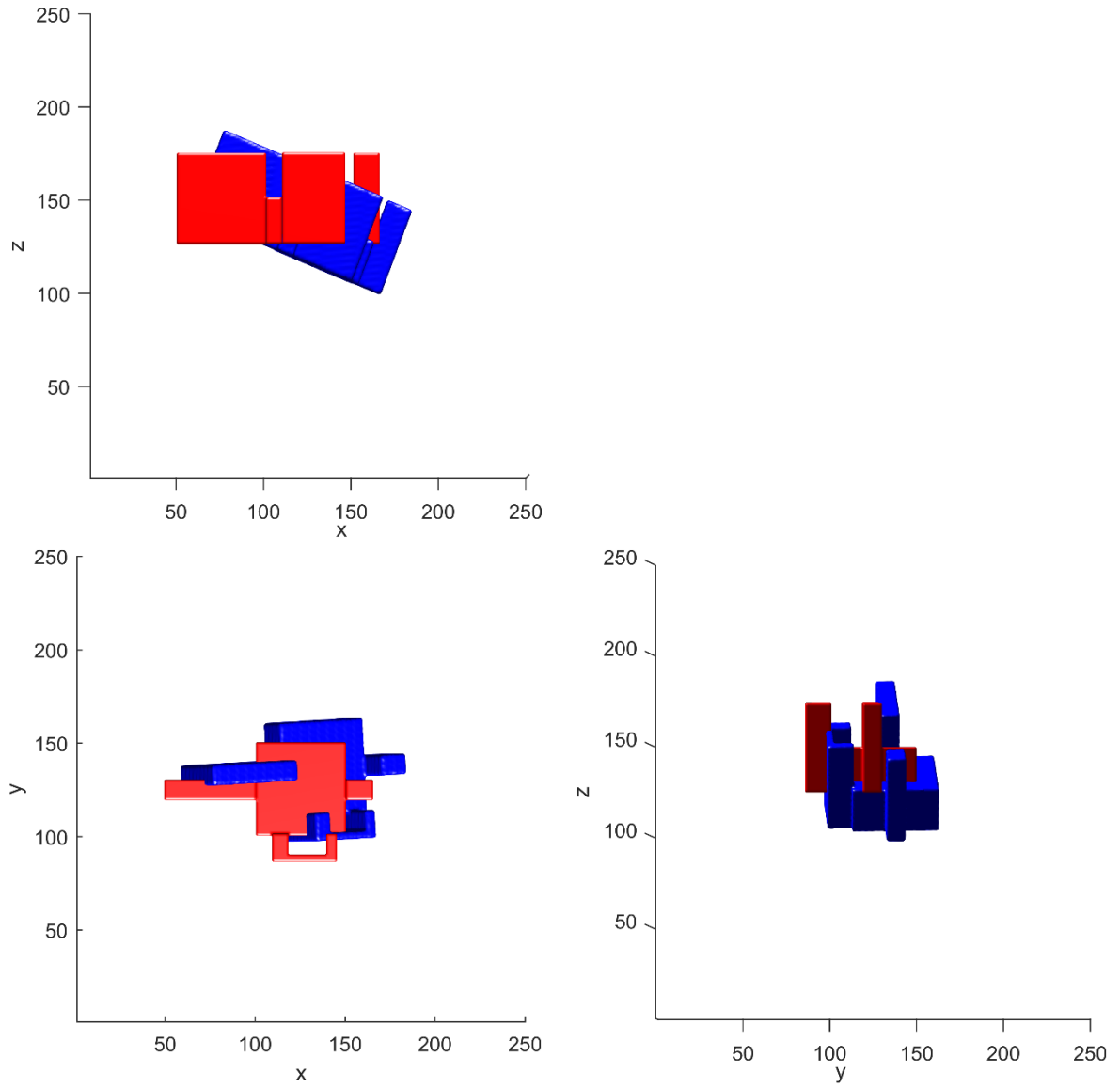


Figure 4-19. The blue volume has now undergone a 11.52° rotation in the x axis. With this rotation the first iteration of the algorithm has been completed.

4.5.3 THE 2ND ITERATION

Similar to the first iteration the rotations are performed in the order of z-axis, y-axis, and then x-axis. These rotations begin to correct the blue volume to the red volume. Figures 4-20 and 4-21 show the rotations performed. The rotation about the y-axis on the second iteration was 0° and is not shown.

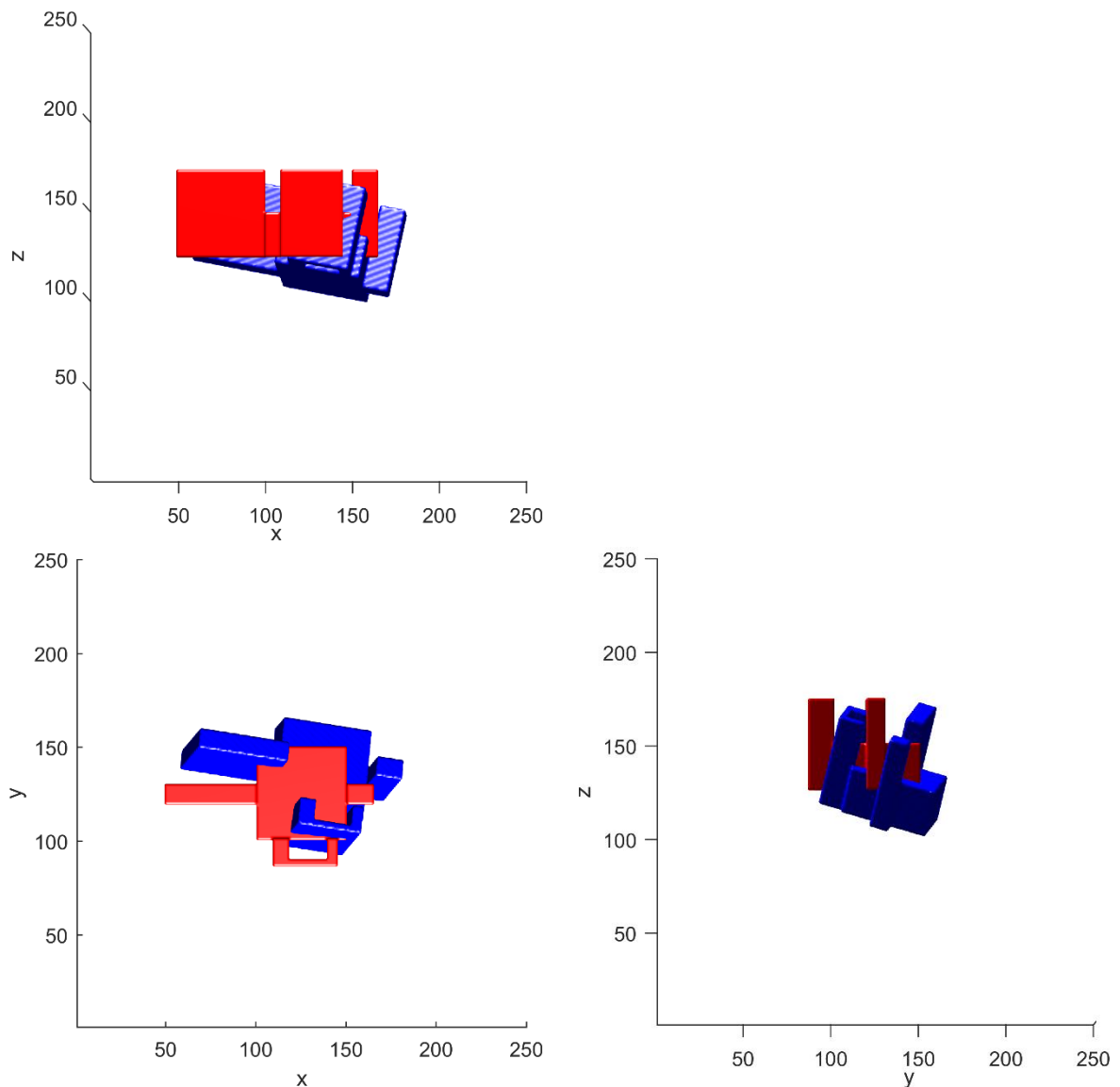


Figure 4-20. The rotation about the z-axis for the second iteration is -2.88° .

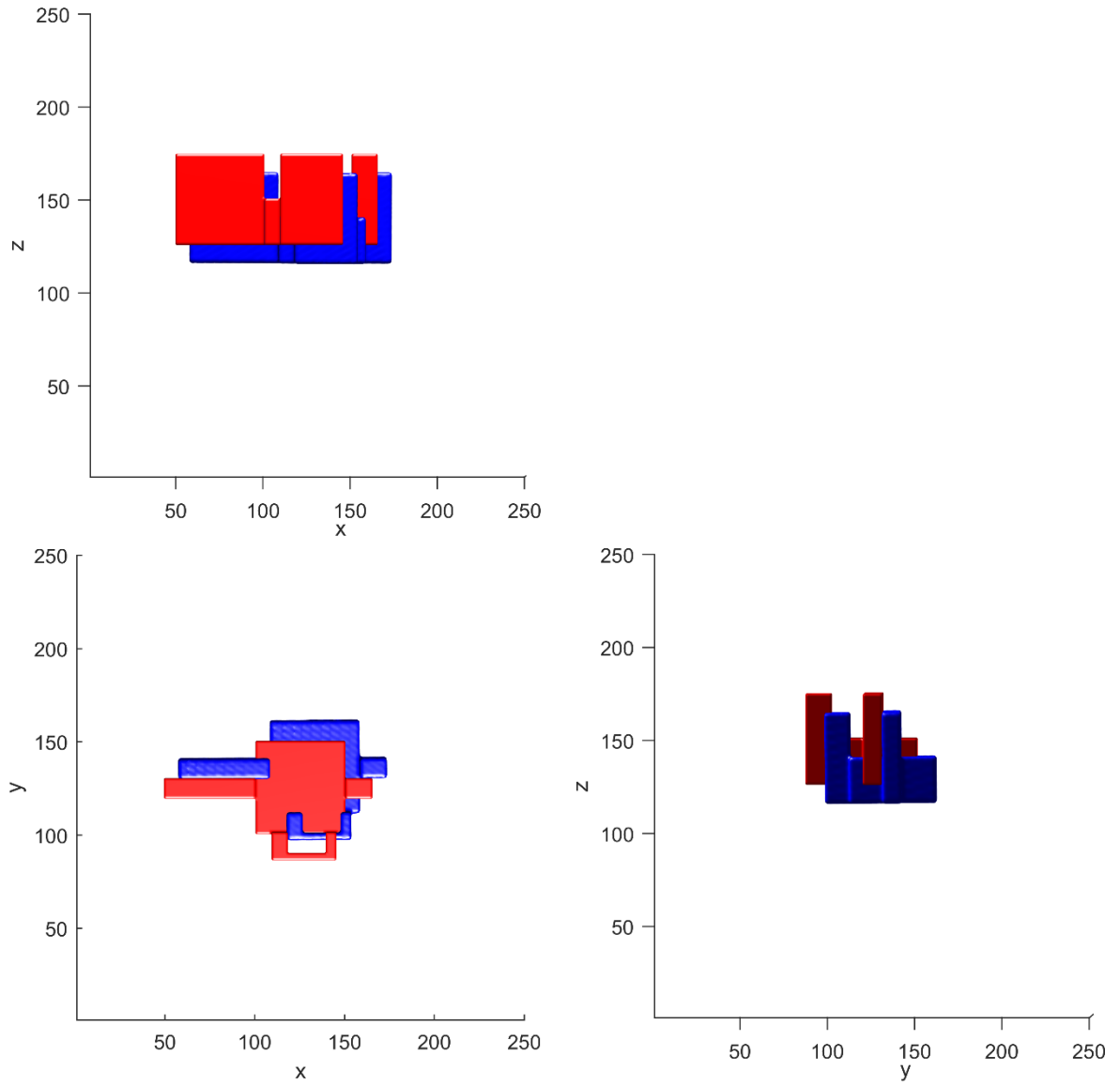


Figure 4-21. The x-axis rotation for the second iteration is -21.6° . This rotation bring the volumes into rotational alignment.

4.5.4 THIRD ITERATION AND TRANSLATION CORRECTION

The third iteration for the rotational correction is zero degrees for all of three axis. All rotations are considered accounted for. The last step that needs to be performed is the translation correction. The translation correction is -9 voxels in x, -12 voxels in y, and lastly 10 voxels in z. The final corrected volumes are shown in figure 4-22.

With the algorithm now complete, this test case has successfully registered the blue volume to the gold-standard red image. The total runtime of the algorithm was

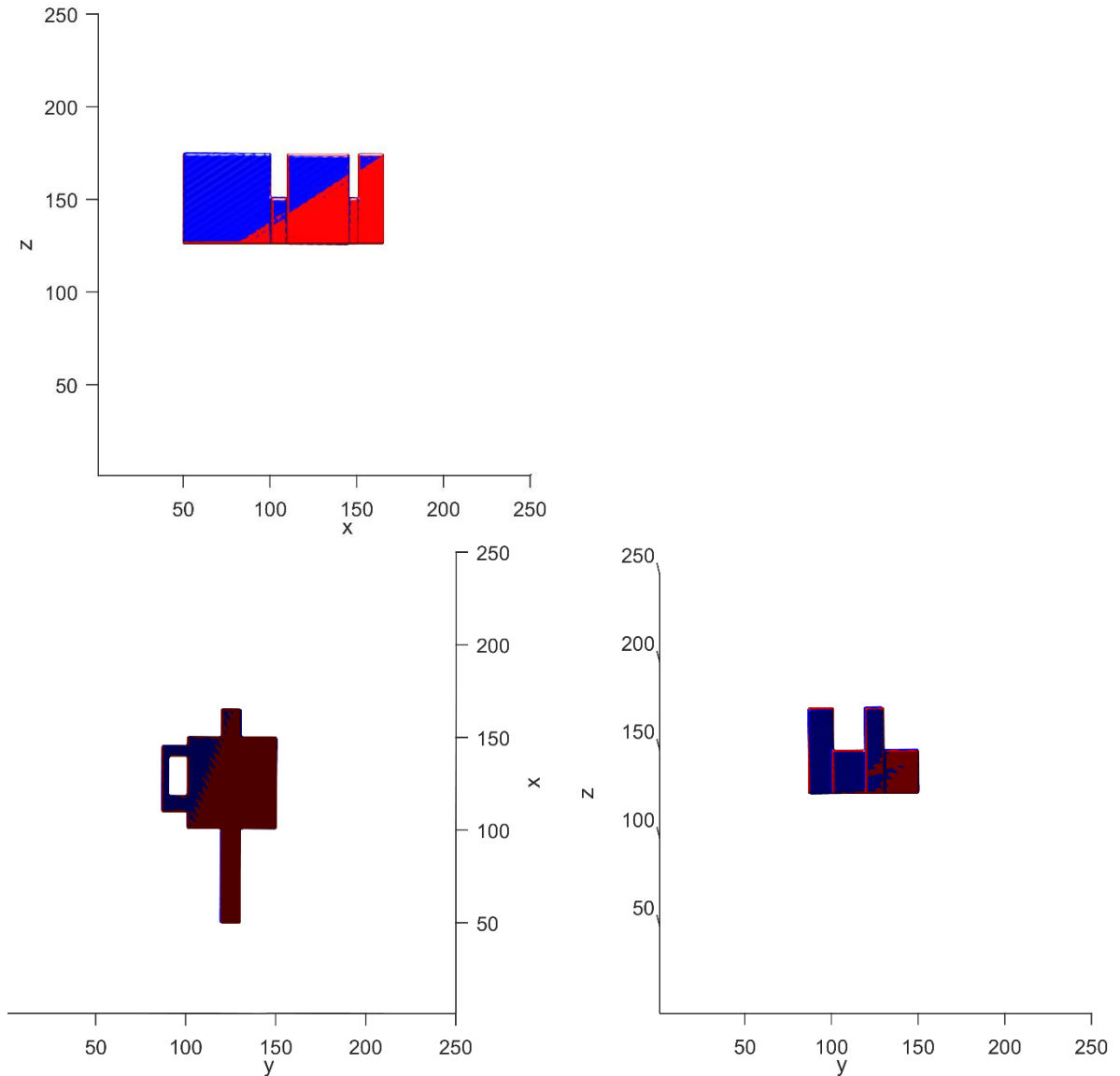


Figure 4-22. The fully corrected volumes are shown. The red and blue volumes are overlapped to be nearly indistinguishable.

4.6 CONCLUSION

Superimposition is an important technique used in orthodontics. Superimposition allows an orthodontist to identify changes that occur in a patient with growth and treatment. This information allows the orthodontist to revise the patient's treatment plan. A new superimposition algorithm is introduced that uses phase correlation and iteration.

This method will have an accuracy limited by the voxel size of the image and the size of the image. The runtime of the algorithm is dependent on image size, the runtime for the sample run in section 4.5 was less than three minutes. The algorithm does not require user input if the registration is being performed using the entire volume, besides selecting the volumes to be used. If only a portion of a volume is to be used for registration, then the only user involvement is selecting the appropriate section of the volume. No landmark selection is required using this superimposition method.

4.7 REFERENCES

1. Barbosa LV. Fourier transform time and frequency domains [image on the internet]. 2013 Feb 23 [cited 2015 Sept 15]. Available from: <http://tinyurl.com/qfkipj44>
2. Minecraft ®/TM & © 2009-2013 Mojang / Notch
3. Osgood B. EE261 The Fourier Transform and its Applications [Internet]. Lecture notes presented at; 2007; Stanford University. [cited 2015 Sept 15]. p. 350-351. Available from: <http://tinyurl.com/pehdbxy>
4. S. Derrode and F. Ghorbel, "Robust and Efficient Fourier–Mellin Transform Approximations for Gray-Level Image Reconstruction and Complete Invariant Description," *Comput. Vis. Image Underst.*, vol. 83, no. 1, pp. 57–78, Jul. 2001.
5. Bican J, Flusser J. 3D Rigid registration by cylindrical phase correlation method. *Pattern Recogn. Lett.* 30, 10 2009 July; 30: 914-921. doi:10.1016/j.patrec.2009.03.015
6. Nakamori, T.; Okabayashi, H.; Kawanaka, A., "3-D Object matching using phase correlation method," in *Signal Processing (ICSP), 2010 IEEE 10th International Conference on*, vol., no., pp.1275-1278, 24-28 Oct. 2010 doi: 10.1109/ICOSP.2010.5656976
7. From Wikipedia. Cylindrical Coordinates [image on the internet]. 2008 Apr 08 [cited 2015 Sept 15]. Available from: <http://tinyurl.com/mn3fno2>
8. Gonzalez, Ruben. "Improving Phase Correlation for Image Registration" in *Image And Vision Computing New Zealand 2011*, 2011 © IEEE. <http://hdl.handle.net/10072/44512>
9. Otsu, Nobuyuki . "A Threshold Selection Method from Gray-Level Histograms," in *Systems, Man and Cybernetics, IEEE Transactions on*, vol.9, no.1, pp.62-66, Jan. 1979 doi: 10.1109/TSMC.1979.4310076

5 ASSESSMENT OF SUPERIMPOSITION ALGORITHM: PATIENT CASE STUDIES

5.1 INTRODUCTION

One of the main tools in an orthodontist's toolbox to assess treatment outcome is pre- and post-image superimposition, also known as registration. Superimposition allows an orthodontist to overlap two images and assess structural changes taken at different times, i.e., time one (T1) and time two (T2). This process can be used to find the efficacy of treatment, and recommend the best possible future treatment option.

Traditionally, superimposition was performed on 2-D x-rays using line sketching and transparencies [1]. An issue that arises with this method is that change can only be measured in a two dimensional plane. With the advent of three dimensional CBCT scans, new methods of superimposition needed to be investigated. In literature, there are currently two main methods in use for superimposition of 3D anatomical structures specific to orthodontics. These are the method of registration using points[2], [3] and maximization of mutual information (MMI) [4], [5]. Both of these registration methods have benefits and weaknesses. The point method is dependent on researcher landmark placement. Even though the method corrects for some researcher error, it can still result in errors in the superimposition of image data. This error is only compounded if the scans are noisy or low quality (e.g. blurring introduced by patient movement). Maximization of mutual information requires a good initial guess for the registration and cannot guarantee convergence to the global minimum, representing the best registration solution.

A new method of superimposition was presented in Chapter 4. This superimposition method is easy to use and requires minimal clinician interaction, while also not relying on a user's ability to select landmarks. Its principal means of calibration only used the cranial base region of the skull; this was selected since it is considered a stable region of growth after age 5. This would allow the registration to be performed on adolescent patients that are still undergoing growth and change in the skull and jaw.

An additional benefit of this method is that the transformation matrix to register the two scans is directly found. This can then be applied to previously measured landmark points to directly compare T1 and T2 landmarks. This registration method uses a technique known as phase correlation that is common in 2D image analysis. Bican and Flusser suggested a similar technique using phase correlation to register MRI data while Nakamori *et al.* suggested a phase correlation based technique for comparing laser scanned face models [6], [7].

This section of the thesis will show the capabilities of the new superimposition method. Testing is performed using patient data given a known error amount. A T1 and T2 patient scan with unknown rotational and translation differences will also be tested to show the superimposition method. This method will be tested against the point method described in [2]. An error of 1mm will be considered clinically significant.

5.2 MATERIALS AND METHODS

There are three steps to testing the superimposition method. The first step is to find the optimal image filtering and blurring parameters, namely, strength of the high-pass filter, represented by a value sigma (σ), and if thresholding and/or windowing should be turned on or off. The second step is testing the optimization on volumes of a cranial base with known errors introduced to find the accuracy and repeatability of the superimposition method. The third step is then to test the method on a patient's T1 and T2 scans. The final step is a comparison of the new method and the 6-point method [2]. All cranial base models will be shown to allow the reader to better understand the organic look and structures that need to be registered, including how the images are cropped down to a smaller size.

The results will be analyzed using MATLAB (MATLAB 2015b, Mathworks Inc., Natick, MA, USA) and visualized using Avizo (AVIZO 8.1, Visualisation Sciences Group, Burlington, MA, USA). The registration method requires that both of the input images are the same size. The run time of the fast Fourier transform (fft) is mainly dependent on volume size. Therefore, all images will be zero padded to a size of 256x256x256 voxels. Zero padding is the process of increasing an images size by adding voxels of value 0 to

each side. A smaller matrix is not used since the potential accuracy of the registration is determined by the size of the input matrices. A larger matrix would increase accuracy of the registration but would require larger memory requirements of the computer and increase runtime.

5.2.1 FINDING THE OPTIMAL PARAMETERS

In Section 4.4 different parameters are shown to improve phase correlation. The parameters are 1) the strength of the filter (σ), 2) thresholding on/off, and 3) windowing on/off. The parameters are selected by running a test in which a model of a cranial base (shown in Figure 5-1) is given a random, known error, and the algorithm is run to find the correction. The images are padded with zeros to be a full size image of 256x256x256 voxels, ensuring that sections of the image being registered are not cut off during rotations. This is done twice with a full set of parameter options, the parameter options are thresholding on/off, windowing on/off, and a full set of sigma values from 1 to 181 in steps of 20. Steps of 20 were chosen for being small enough to find an accurate best value. The max value of 180 was chosen for being large enough to remove most of the non-noise data including vital high frequency information. This means that for the cranial base the test is run 80 times. This is then repeated for another cranial base model from a second patient (Figure 5-2).

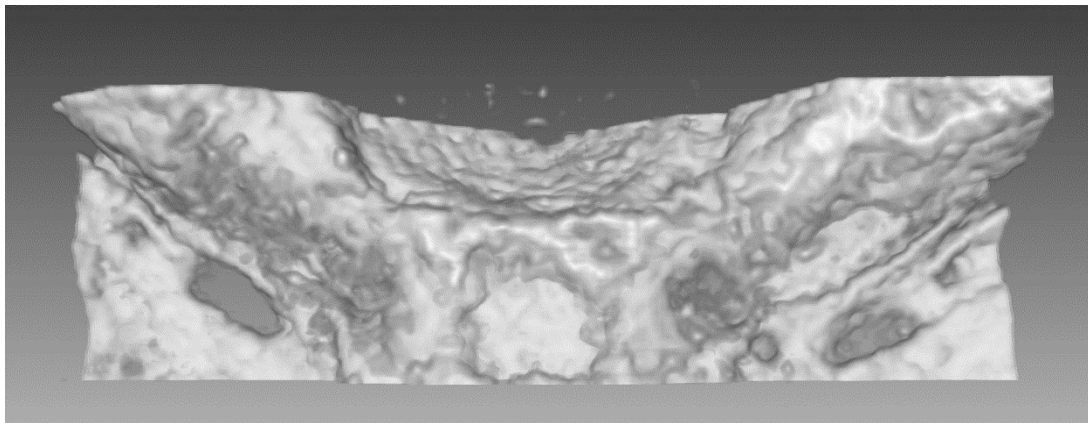


Figure 5-1. View of the transverse plane of cranial base from patient #1, used to find the parameters of the registration algorithm. The view is looking in the inferior direction with the anterior direction being towards the bottom of the page.

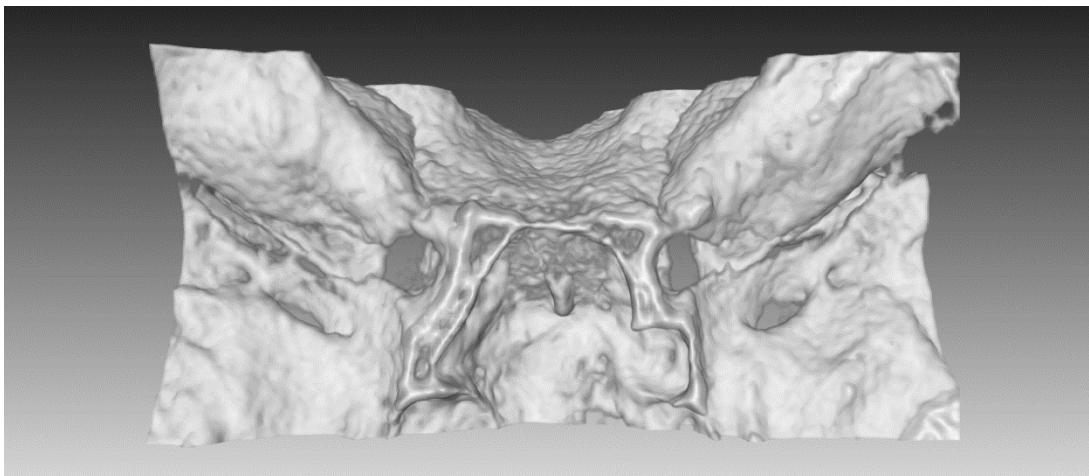


Figure 5-2 View of the transverse plane of cranial base from patient #2, used to find the parameters of the registration algorithm. The view is looking in the inferior direction with the anterior direction being towards the bottom of the page.

The results are first viewed for any failures to converge. A failure to converge means the algorithm could not find a stable solution within seven iterations using the iteration defined in Section 4.1.3, of one x-axis correction, one y-axis correction, one z- axis correction. If any parameters cause a higher convergence failure they will be discounted. Each test has the L2-norm of the registration to the original image computed. This value is used to compare the different scans, a lower value ideally meaning a better registration. It should be noted that this value cannot compare between thresholding and no thresholding, since thresholding changes the voxel values the L2-norm is not a suitable comparison metric. In summary first unsuitable parameters are discounted if they failed to converge, then, L2-norm values are compared to find the best overall settings. The parameter settings found are then used when running the tests described in sections 5.2.2 and 5.2.3.

5.2.2 TESTING ON PATIENT SCANS: INTRODUCTION OF RANDOM ERROR

The algorithm is tested on cranial bases with an introduced random, known, error. This is done for 5 different patient scans with each scan having errors introduced and corrected for 10 times. This results in a total of 50 trials. The random error introduced was between -10 degrees and 10 degrees about each axis and between -15 and 15 voxel shift in each direction. The random error rotation limit was chosen as 10 degrees is a greater rotation than should exist between patient scans if the patient is seated properly during scan acquisition. The registered image is then compared to the original and the L2 norm

between them is computed to find the error. The 5 cranial bases used are shown in Figure 5-1, Figure 5-2, and Figure 5-3 (which contains cranial bases from patients #3-#5). For testing with known rotations and translations 5 patient scans is considered an adequate sample size.

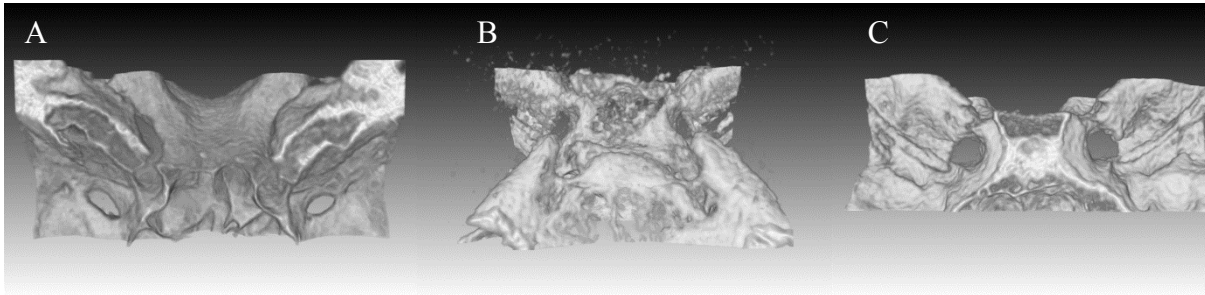


Figure 5-3. Figures A, B, and C are the remaining cranial bases from patients #3, #4 and #5, respectively.

An “allowable” L2 norm is found by performing a Monte Carlo analysis on each cranial base. The cranial base is rotated and translated a random, small, amount and the L2-norm is found between the original and rotated/translated volumes. The maximum change is between -2 and 2 voxels of shift in each dimension and between -2 and 2 degrees of rotation about the center of the cranial base. The translations results in a maximum displacement of approximately 3.5 voxels (found using the Pythagorean Theorem), which is equivalent to a maximum displacement of 1.04mm for the current voxel size of 0.3mm. A rotational change would also introduce error; with a maximum rotation of 2 degrees in a direction this would introduce 1 voxel of error for every 29 voxels past the rotation centre. This is repeated 100 times for each cranial base.

5.2.3 REGISTERING T1 AND T2 PATIENT DATA

The final set of tests performed is running the registration on 10 patients for T1 and T2 and comparing the results to the 6-point method from [2]. Ten patients are used to allow for a strong comparison to the six-point method. One patient (not compared to the 6-point method) is shown for illustration purposes. The error will be quantified by taking the L2-norm of the superimposed image when (1) superimposed using the new method and (2) using the transformation found by the 6-point method. Since it is important to reduce errors from cropping, the gold standard image (T1) will be selected larger than the cranial base

that will register to it (T2). The cranial base image will then be windowed and padded with zeros to equal the same size as T1. When calculating the L2-norm, after registration, the padding with zeros of the T2 scan and the corresponding location T1 voxels are ignored. Figure 5-4 shows anterior (side) and superior (top) views of unregistered images in the same global coordinate system. Appendix A includes Superior views of all ten cranial bases used to compare to the 6-point method [2], and the landmark locations of the points used for the 6-point registration.

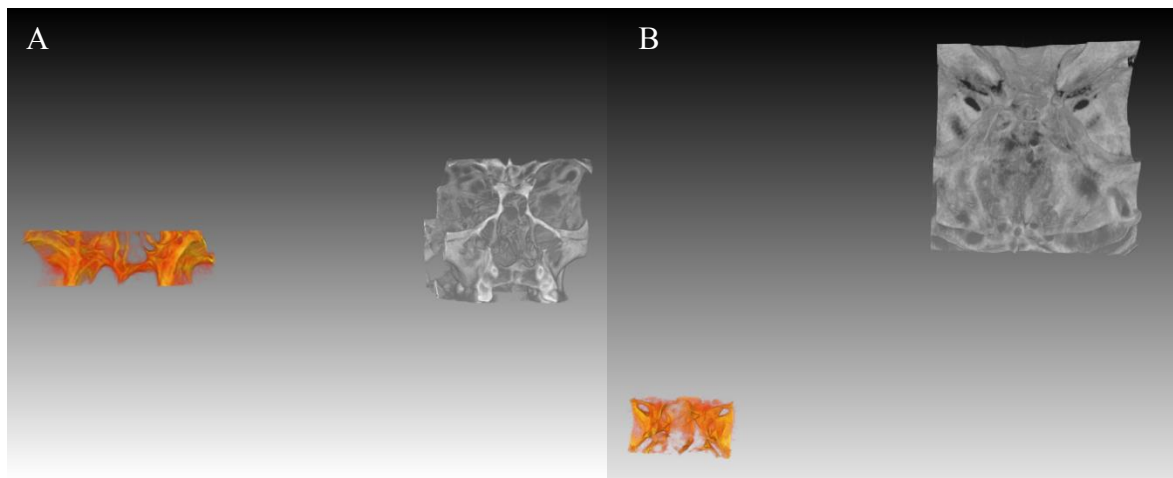


Figure 5-4. (A) An anterior view of the images to be registered. (B) A Superior view of the images to be registered. The red image is registered into the gray image. The gray image is T1 and the red image is T2. The reason the T2 image appears smaller in Figure 5-4B is due to perspective as it is located farther into the page in the global coordinate system.

This technique determines the rotations and translations required for registration. Since the rotation centers (center of the registering image) and the cropped image sections are also obtained, the rotations and translations can be applied to T2 at post-processing using an image analysis program for visualization. The algorithm also outputs the transformation matrix for the registration, allowing for conversion of points measured on T2 in the global coordinate system to be transformed to the equivalent T1 points in the global coordinate system. This is beneficial as previously located landmarks do not need to be re-measured but can be automatically converted for direct comparison. A transformation matrix is laid out in the form of:

$$M = \begin{bmatrix} R_1 & R_2 & R_3 & t_x \\ R_4 & R_5 & R_6 & t_y \\ R_7 & R_8 & R_9 & t_z \\ 0 & 0 & 0 & 1 \end{bmatrix} \quad (5-1)$$

where R_{1-9} represents any rotations that need to be applied to the image and t_x , t_y , t_z correspond to the required translations in the x , y , and z coordinates, in the global coordinate system. The transformation matrix is applied using:

$$\begin{bmatrix} x' \\ y' \\ z' \\ 1 \end{bmatrix} = [M] \begin{bmatrix} x \\ y \\ z \\ 1 \end{bmatrix} \quad (5-2)$$

where x , y , and z are the coordinates of a point in the global coordinate system and x' , y' , and z' are the resulting transformed points in the global coordinate system. Equation (5-2) must be repeated for each point that needs to be transformed.

The algorithm was then also tested to compare with the 6-point method [2]. This was done by registering the T1 and T2 scan using both methods and comparing the L2-norm values of the registered results, using each technique. Ten patients were landmarked by a clinician with experience using the 6-point method.

5.3 RESULTS

5.3.1 OPTIMAL REGISTRATION PARAMETERS

The results of the registration are shown in Table 5-1 for the first cranial base image and Table 5-2 for the second cranial base image. A bolded value of **-1** for the L2-norm means there was no convergence to a solution after seven iterations.

Table 5-1. L2-norm values of parametric test for cranial base one, the settings are the strength of the Gaussian filter (σ), windowing being turned on or off and thresholding being turned on or off

σ value	Windowing on Thresholding on ($\times 10^5$)		Windowing off Thresholding on ($\times 10^5$)		Windowing on Thresholding off ($\times 10^9$)		Windowing off Thresholding off ($\times 10^9$)	
	Trial 1	Trial 2	Trial 1	Trial 2	Trial 1	Trial 2	Trial 1	Trial 2
1	9.7	10.7	5.9	6.4	443.1	455.6	387.8	436.2
21	3.1	8.0	2.7	7.9	26.0	8.5	8.4	154.3
41	10.6	2.1	2.2	1.7	31.3	40.6	33.0	12.9
61	1.9	1.9	1.7	2.1	8.6	19.4	14.7	10.0
81	1.8	6.7	2.5	2.5	7.0	14.1	13.9	17.6
101	-1	2.0	2.2	1.4	8.6	9.0	11.0	19.8
121	1.5	2.6	-1	2.1	52.7	11.3	25.3	27.6
141	2.5	2.4	9.8	1.6	20.8	12.4	22.1	17.0
161	-1	2.2	2.3	1.7	23.3	27.3	16.5	21.6
181	-1	1.8	7.6	1.7	15.3	15.7	8.7	25.4

Table 5-2. L2-norm values of parametric test for cranial base two, the settings are the strength of the Gaussian filter (σ), windowing being turned on or off and thresholding being turned on or off

σ value	Windowing on Thresholding on ($\times 10^4$)		Windowing off Thresholding on ($\times 10^4$)		Windowing on Thresholding off ($\times 10^9$)		Windowing off Thresholding off ($\times 10^9$)	
	Trial 1	Trial 2	Trial 1	Trial 2	Trial 1	Trial 2	Trial 1	Trial 2
1	17.2	25.0	19.2	26.4	1.3	20.7	43.9	52.2
21	15.4	1.9	1.9	2.3	17.8	69.1	12.6	1.9
41	1.8	1.9	2.3	2.2	1.5	2.8	2.7	2.0
61	2.0	-1	1.7	2.2	2.0	1.9	2.0	5.6
81	1.8	1.4	-1	-1	2.7	2.2	2.7	2.6
101	1.5	-1	2.8	1.4	5.8	2.8	1.2	2.1
121	2.1	3.3	-1	2.5	3.0	2.4	1.5	3.7
141	3.2	1.8	2.8	1.7	1.3	2.3	1.1	1.7
161	2.4	2.2	36.6	1.9	2.9	5.5	3.7	4.9
181	1.9	1.6	2.8	2.0	1.3	2.6	2.7	1.9

The results of Table 5-1 and Table 5-2 show that the thresholding parameter should be turned off as it was the only setting that had non-converging results. The two sets of tests without the thresholding methods involved are plotted in Figure 5-5. Notice that the L2-norm results corresponding to sigma values of 1 and 21 are many times larger than the L2-norm results for the other sigma values.

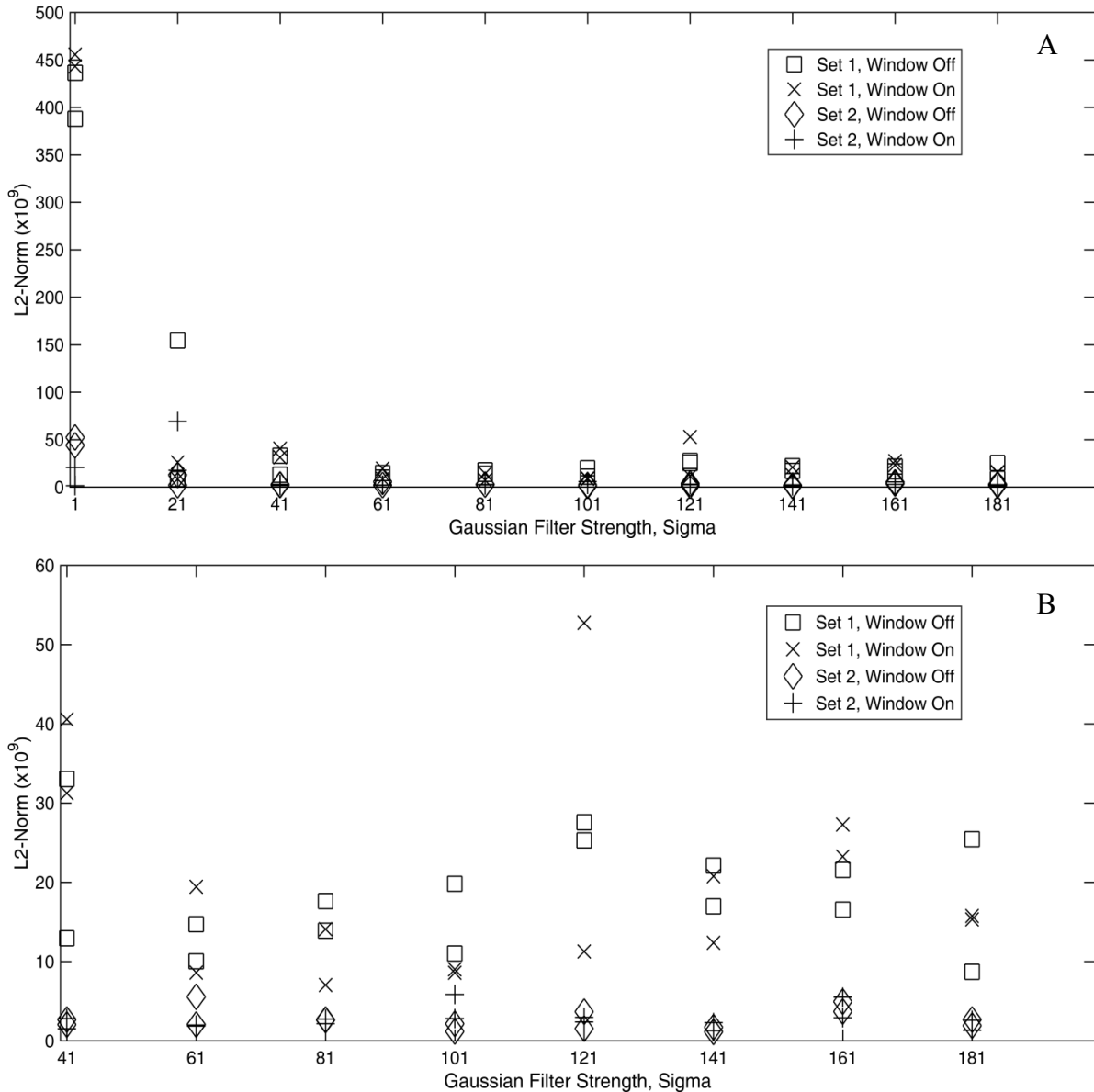


Figure 5-5. The L2-norm values of each of the cranial base tests, excluding tests that involved thresholding. Figure 5-5B has the results for sigma values of 1 and 21 removed. Windowing on means the hamming window is applied to the cranial base during registration, windowing off means the hamming window is not applied during the registration process.

Removing sigma values of 1 and 21 then replotting the data (Figure 5-5B) gives a clearer view of the lower L2-norm values. The results with the lowest L2-norm values occur with a sigma value of 61, 81 or 101. For windowed results, the sigma value of 81 had L2-norm values for set 2 comparable to the other scans, and the lowest L2-norm for a set 1 scan. A

sigma value of 81 also resulted in the windowed results being consistently similar or lower than the non-windowed results.

Based on this study, the parameters used in the remaining of the article are a sigma setting of 80 for the filter, windowing turned on, and thresholding turned off.

5.3.2 TESTING ON CRANIAL BASES WITH KNOWN ERROR

Table 5-3 shows the resulting maximum error and median error found using the Monte Carlo analysis for the 5 cranial bases tested. The full histograms and descriptive statistics from the Monte Carlo analysis are in Appendix A. The maximum error found using the Monte Carlo analysis corresponds to the “allowable” L2-norm discussed in section 5.2.2. Table 5-3 also includes the median error when the Monte Carlo analysis is normalized to the maximum error found. All normalizations are computed according to

$$L2_{\text{normalized}} = \frac{L2}{L2_{\text{maximum}}} \quad (5-3)$$

where $L2$ is the value that is being normalized, and $L2_{\text{maximum}}$ is the largest L2-norm found in the Monte Carlo analysis for the cranial base model.

Table 5-3. The maximum and median values of the Monte Carlo analysis for the 5 cranial bases images. The normalized median is normalized with respect to the corresponding Monte Carlo maximum. The Monte Carlo Maximum becomes the max allowable error for future tests using the corresponding cranial base model.

Test Set	Monte Carlo Maximum (x10 ⁹)	Monte Carlo Median (x10 ⁹)	Normalized Median
1	5.76	4.19	0.73
2	32.9	27.9	0.850
3	31.3	25.8	0.823
4	30.7	24.7	0.803
5	33.4	28.9	0.863

Figure 5-6 shows the results of the ten tests per patient test. The results are normalized using the maximum error found using the Monte Carlo analysis (equation (5-3)). A value of greater than one in Figure 5-6 is an error greater than the allowable error found using the Monte Carlo analysis. None of the trials from test sets 2 or 3 had error greater than found

through the L2-norm. Test sets 1 and 5 each had one trial with error large enough to be considered unsuitably transformed. Lastly trial 4 has multiple scans that resulted in an unacceptable error.

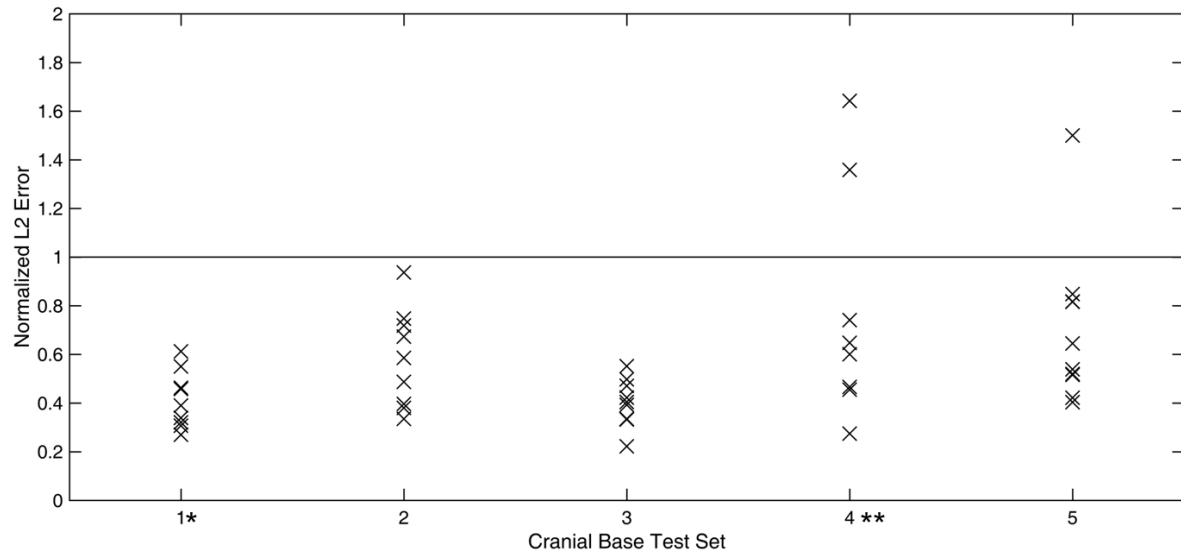


Figure 5-6. The normalized L2-norm results of the cranial base test sets. Each test set consists of 10 trials. The data is normalized with respect to the largest L2-norm value found using the Monte Carlo Analysis. The * shows there was an outlier resulting from non-ideal convergence, resulting in a normalized L2 Error greater than 2. Test set 1 had 1 outlier, while test set 4 had 2 outliers.

5.3.3 REGISTRATION OF PATIENT T1 AND T2 DATA

The algorithm is applied to the registration of patient data. The L2-norm results are shown in Table 5-4. The new method had comparable, or superior, registration results in 4 of the 10 tests. It is assumed that a lower L2-norm means less error in the registration. The L2-norm values cannot be compared quantitatively in depth (e.g. a twice as large L2-norm does not mean there was double the error in registration). The average run-time per registration was 6 minutes using the 6-point method and 2.6 minutes using the new method. The results of the 6-point test, namely, plots showing convergence of the iterations and the registered landmark locations, are available in Appendix A.

Table 5-4. The median L2-norms of the registered images are used to compare between the new method and the six-point method. The bolded value is the lower of the two methods for the scan. If both values are bolded the results are within 10%.

Patient Test	L2-Norm of T1 and T2 scans registered using 6-point method (x10 ³)	L2-Norm of T1 and T2 scans registered using new method (x10 ³)
1	11.31	37.69
2	9.08	23.72
3	16.36	42.8
4	11.36	12.10
5	7.69	74.87
6	5.05	2.23
7	12.90	93.76
8	4.26	18.04
9	13.89	7.92
10	17.32	8.77

Figures 5-7 through 5-16 show the L2-norm error histograms for the new registration method and the 6-point registration method. All sections of the larger time 1 scan that fall outside of the size of the time 2 scan are ignored. Patients 5, 7, and 8, appear to have some skewing in the error, appearing as a hump in the histogram at larger L2-norm voxel errors.

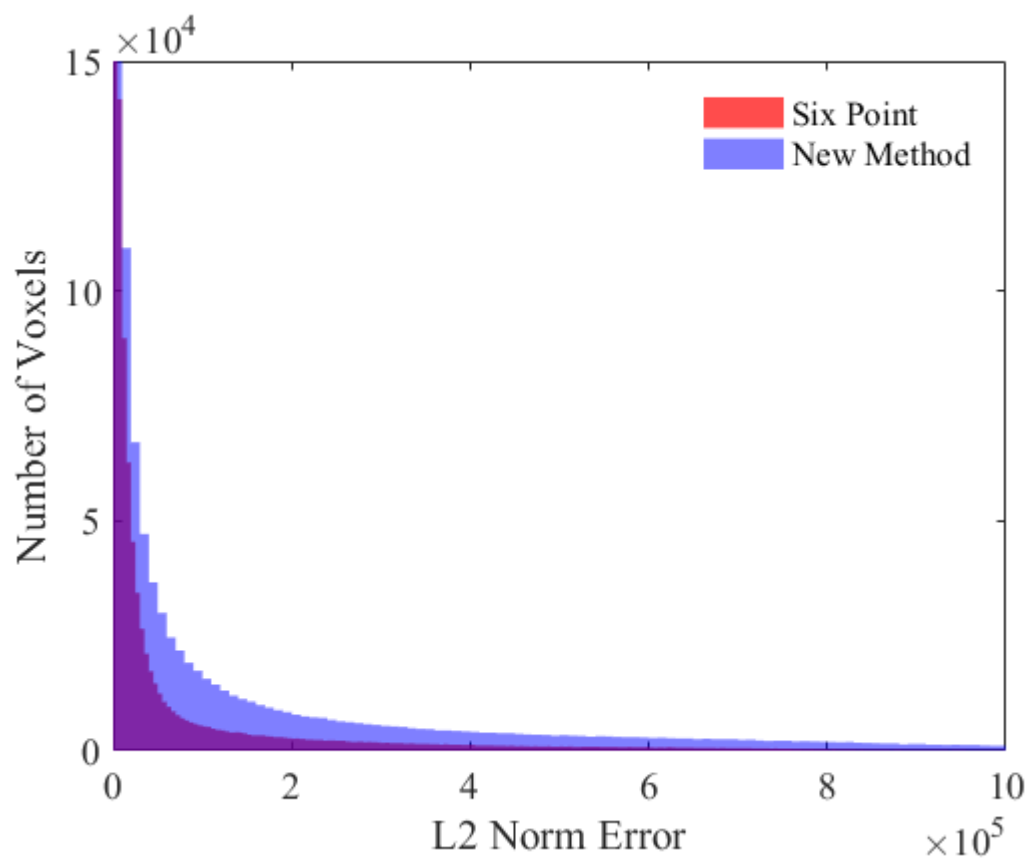


Figure 5-7 Histogram showing the L2-Norm error in registration for the patient 1 time 1 and time 2 scans using the 6-point registration method and the new method. The purple section is where the histograms overlap.

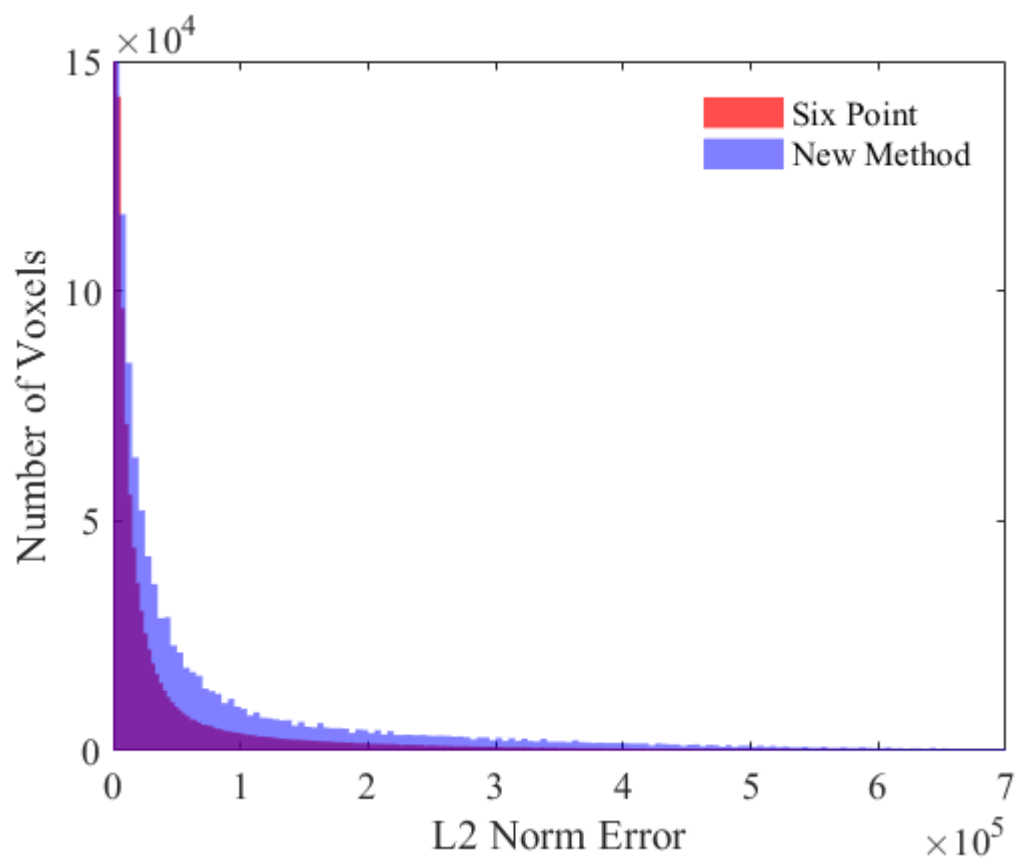


Figure 5-8 Histogram showing the L2-Norm error in registration for the patient 2 time 1 and time 2 scans using the 6-point registration method and the new method. The purple section is where the histograms overlap.

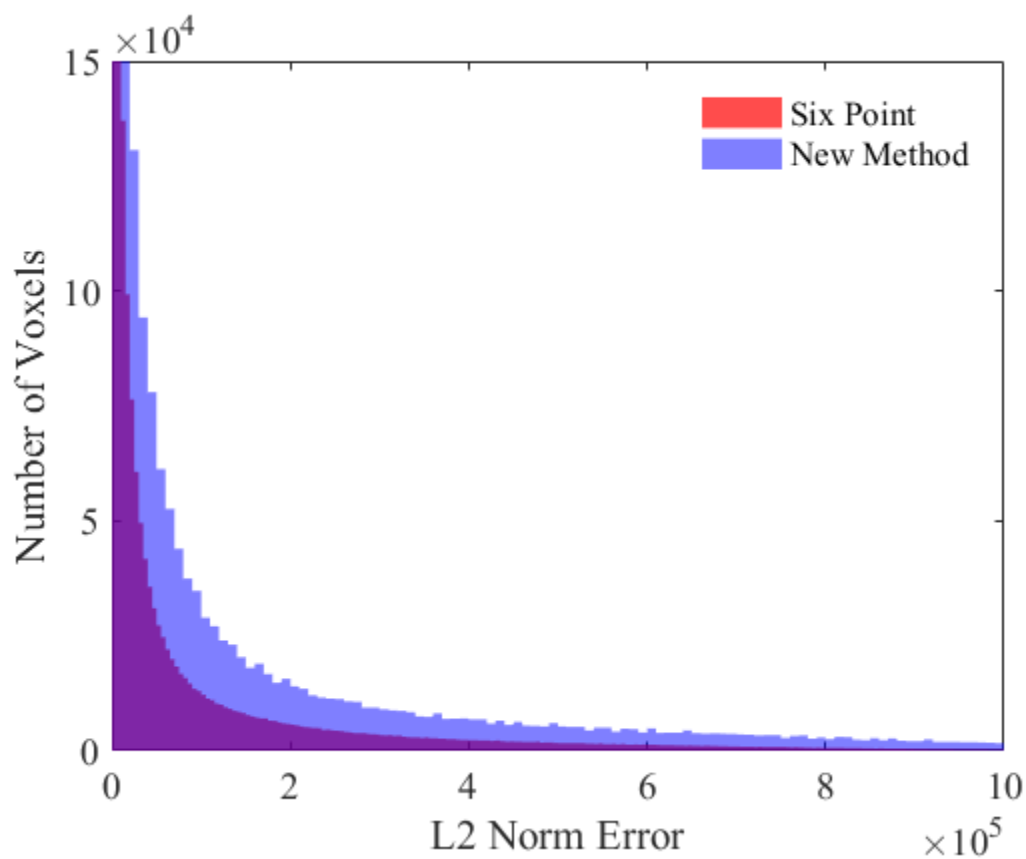


Figure 5-9 Histogram showing the L2-Norm error in registration for the patient 3 time 1 and time 2 scans using the 6-point registration method and the new method. The purple section is where the histograms overlap.

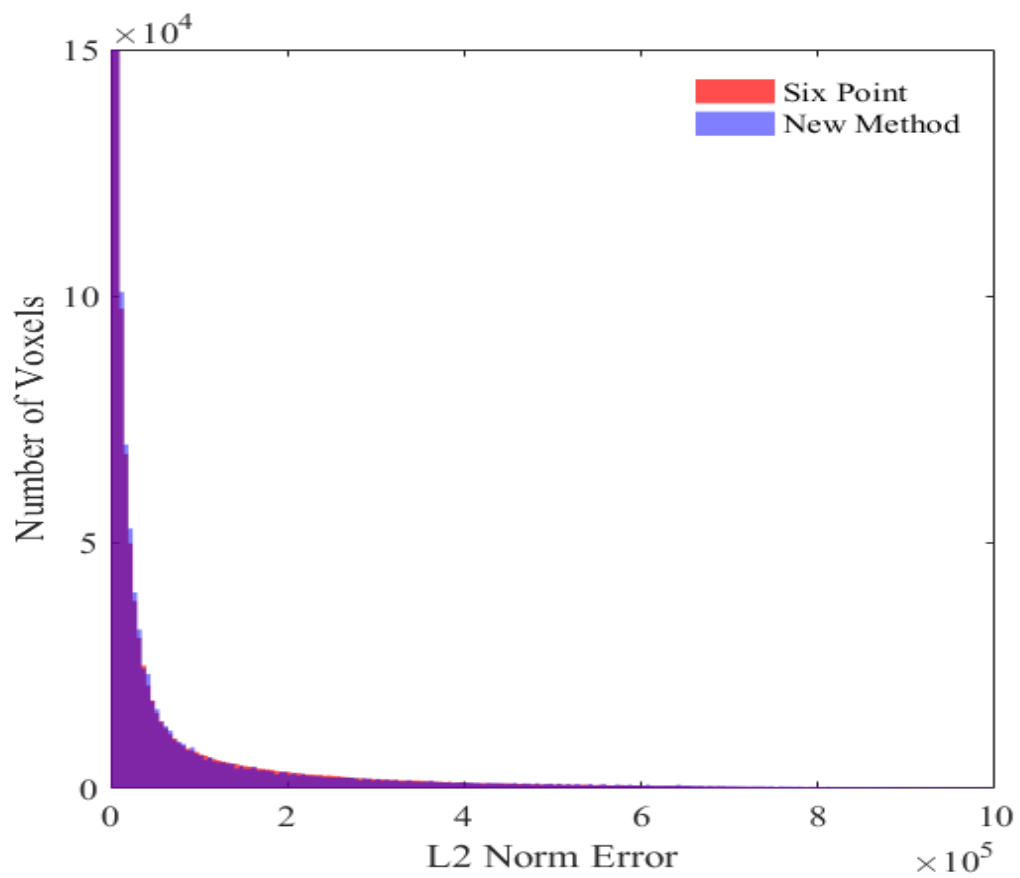


Figure 5-10 Histogram showing the L2-Norm error in registration for the patient 4 time 1 and time 2 scans using the 6-point registration method and the new method. The purple section is where the histograms overlap.

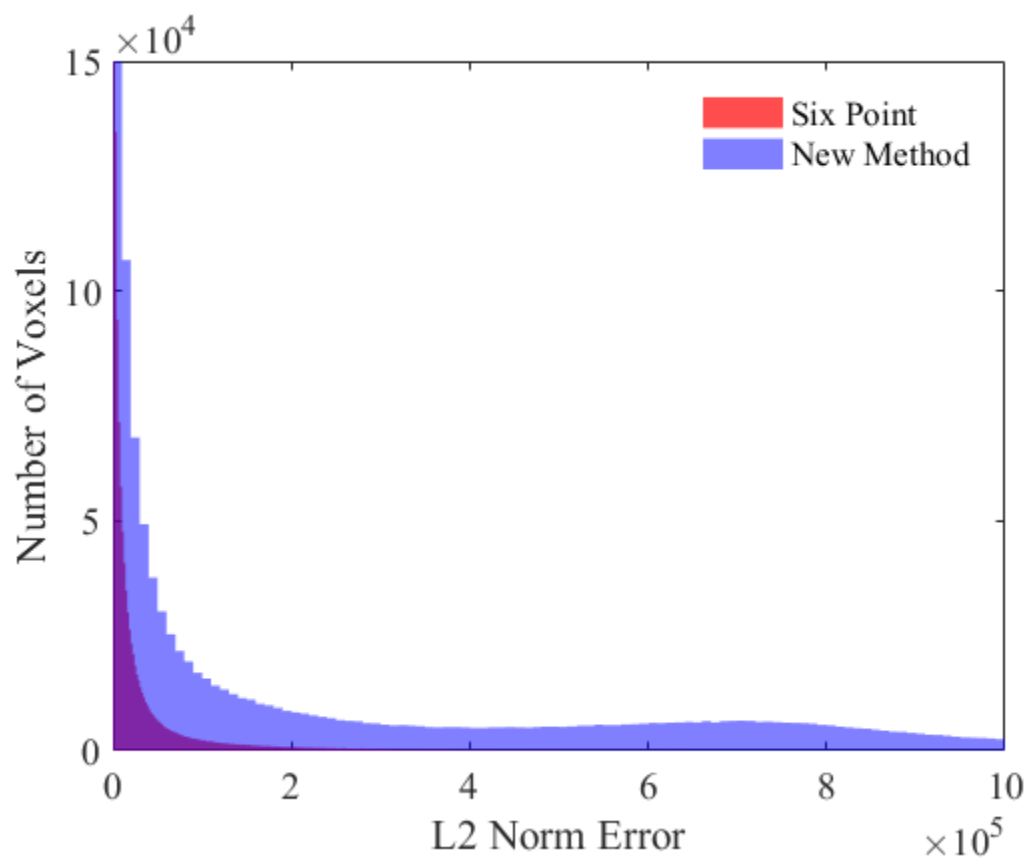


Figure 5-11 Histogram showing the L2-Norm error in registration for the patient 5 time 1 and time 2 scans using the 6-point registration method and the new method. The purple section is where the histograms overlap.

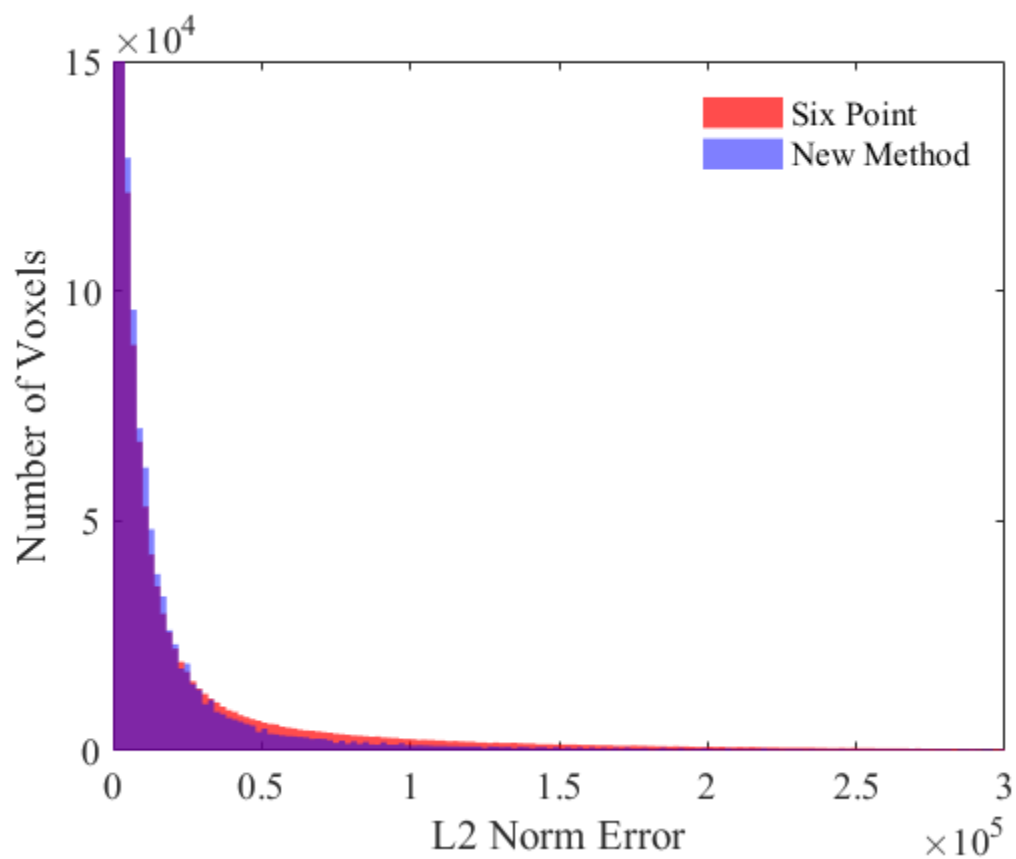


Figure 5-12 Histogram showing the L2-Norm error in registration for the patient 6 time 1 and time 2 scans using the 6-point registration method and the new method. The purple section is where the histograms overlap.

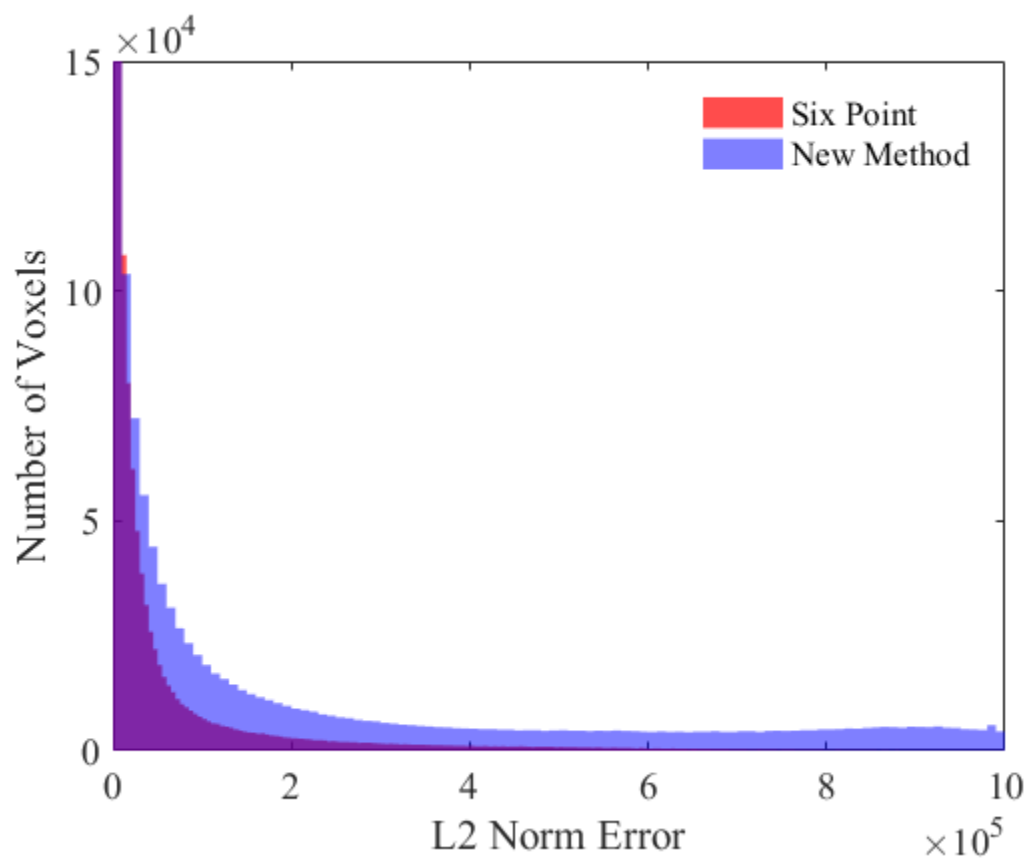


Figure 5-13 Histogram showing the L2-Norm error in registration for the patient 7 time 1 and time 2 scans using the 6-point registration method and the new method. The purple section is where the histograms overlap.

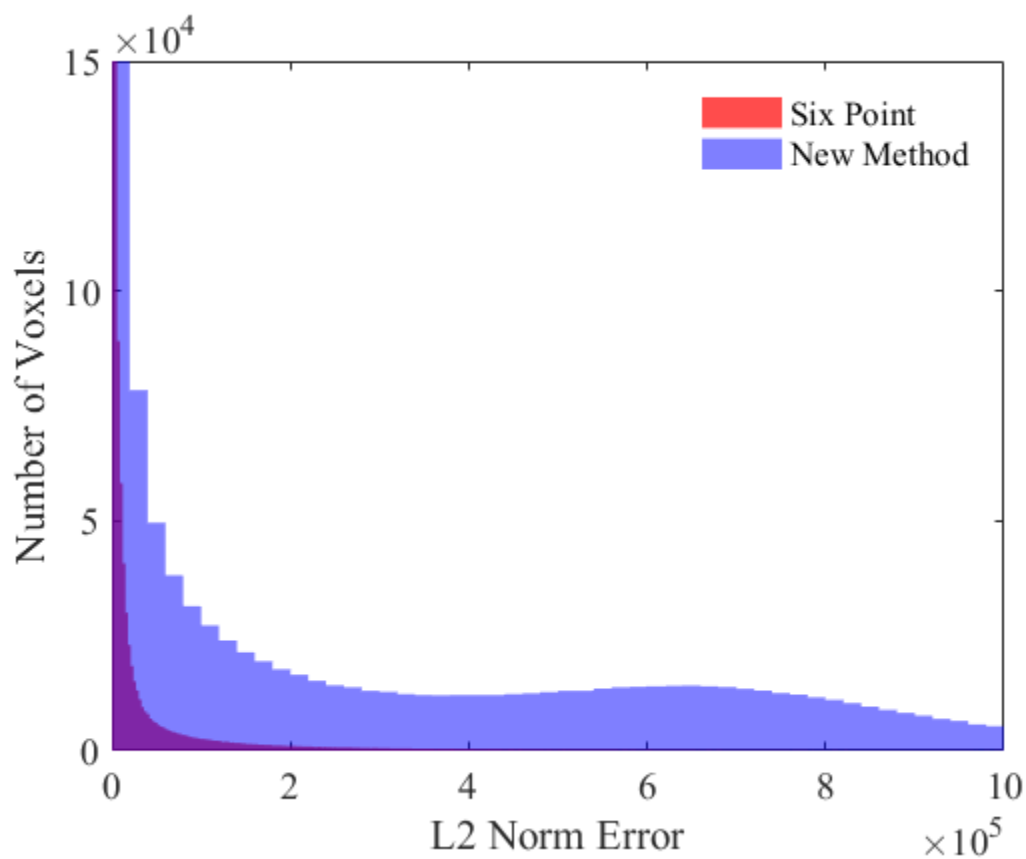


Figure 5-14 Histogram showing the L2-Norm error in registration for the patient 8 time 1 and time 2 scans using the 6-point registration method and the new method. The purple section is where the histograms overlap.

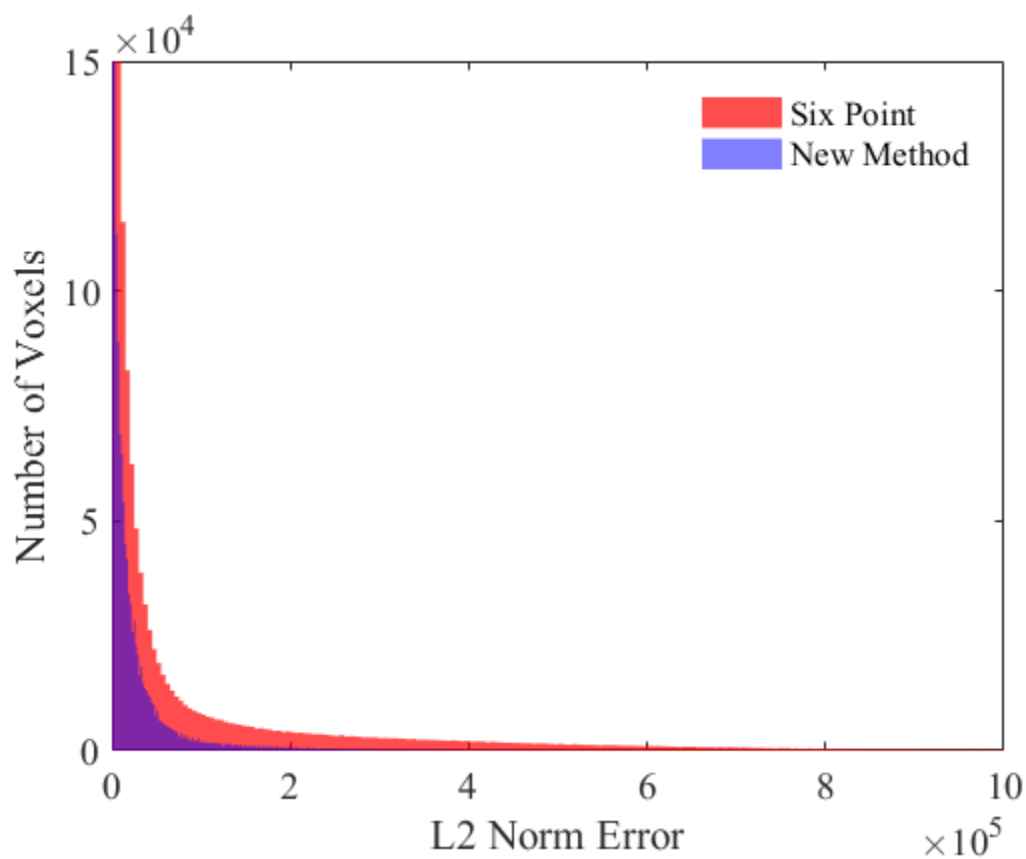


Figure 5-15 Histogram showing the L2-Norm error in registration for the patient 9 time 1 and time 2 scans using the 6-point registration method and the new method. The purple section is where the histograms overlap.

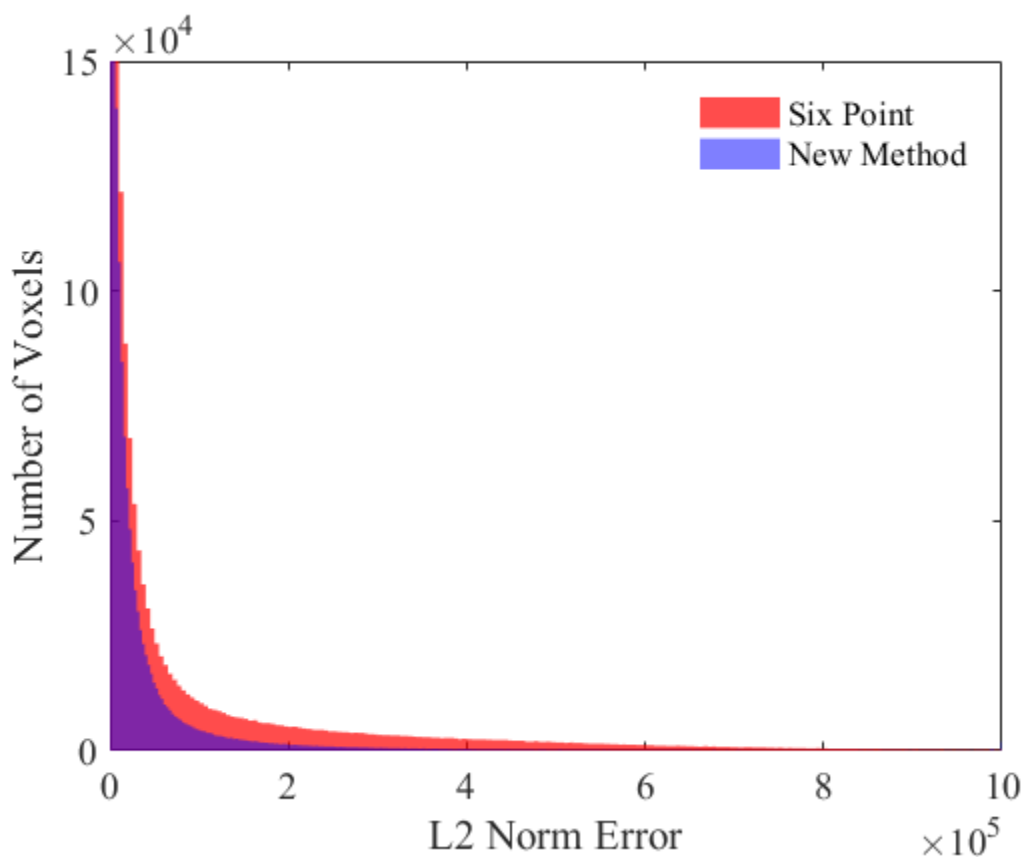


Figure 5-16 Histogram showing the L2-Norm error in registration for the patient 10 time 1 and time 2 scans using the 6-point registration method and the new method. The purple section is where the histograms overlap.

The registered cranial bases for illustration purpose are shown in figure 5-17 and Figure 5-18. It should be noted that there appears to be a small rotation error when viewing top down on the superimposed cranial bases. This error is approximately 1.5 degrees (Figure 5-18) when measured on the images using a protractor (black lines imposed over Figure 5-18). Rotation error is only visible in the transverse plane. This would cause an error in the registration of 1mm for every 38mm of distance from the center of the cranial base. Assuming the cranial base lies midway between the front and back of the human head the distance between the cranial base and the teeth is approximately 10mm [8]. This would result in an error of approximately 2.5mm at the teeth.

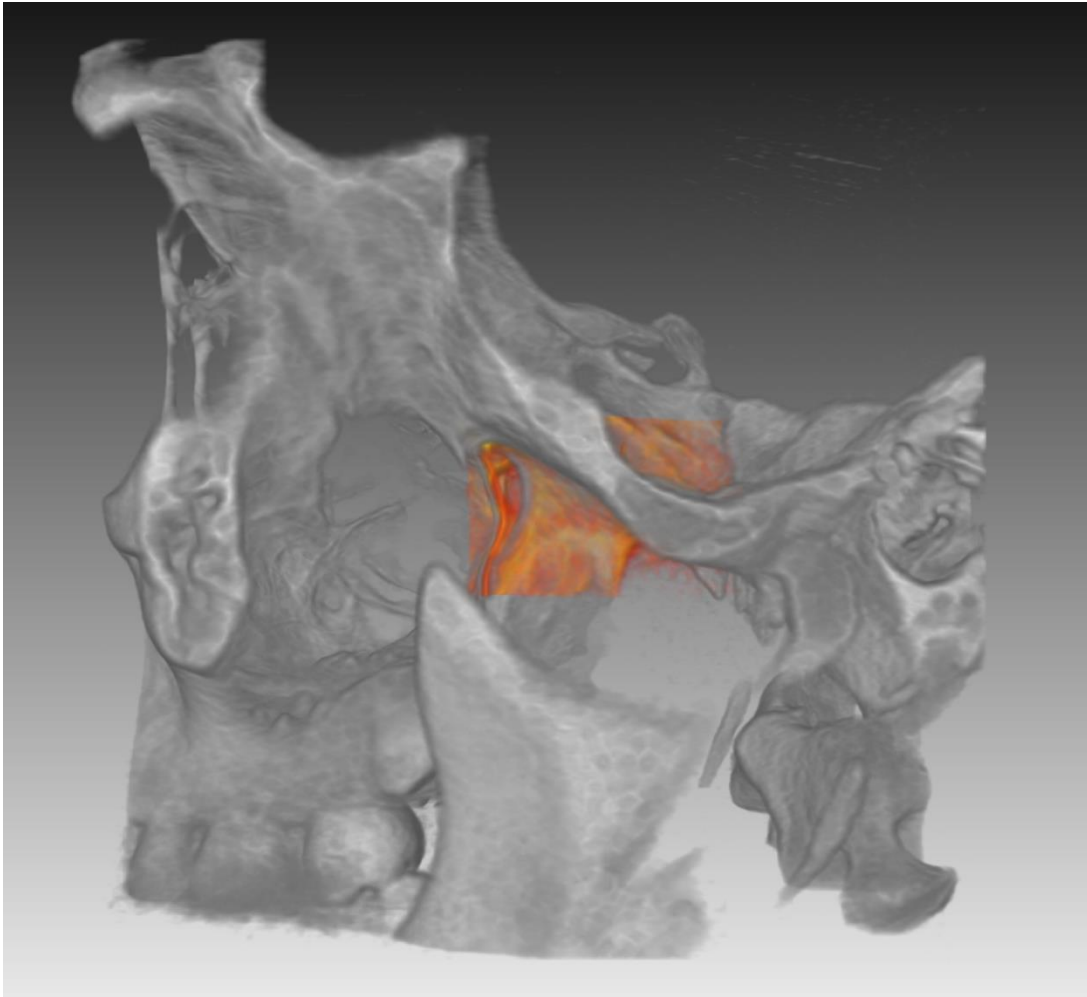


figure 5-17. The cranial base from T2 (red) was successfully aligned with the cranial base (grey) from T1.

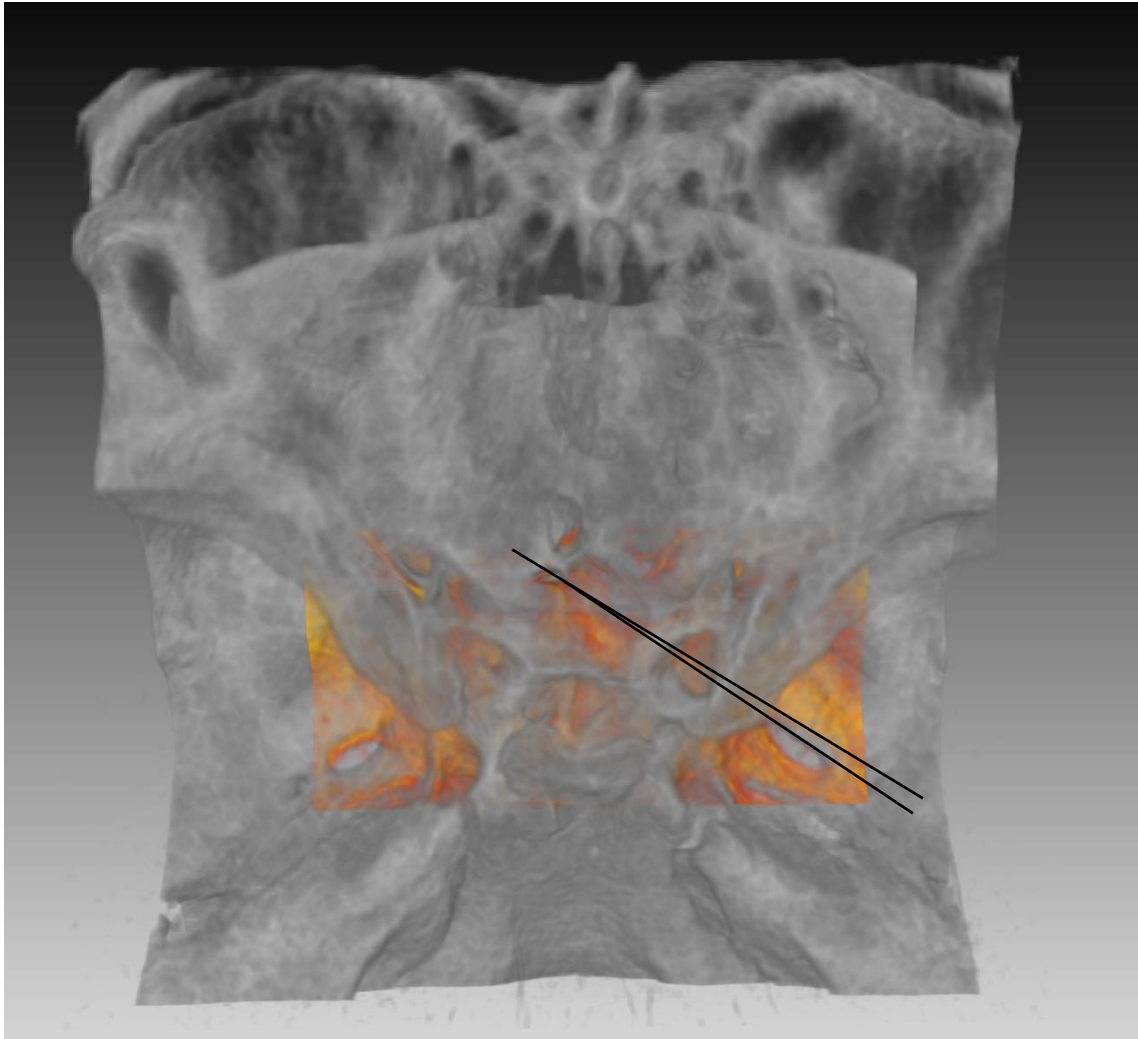


Figure 5-18. A superior view of the registration. The cranial bases have a small error in registration that is visible in this view as a rotation (imposed black lines).

Figure 5-19 shows the fully registered results of the test from the front view with the images thresholded to show the change in facial detail. Figure 5-20 shows the registration with the thresholding set to show the skull and the change in teeth shape and location.

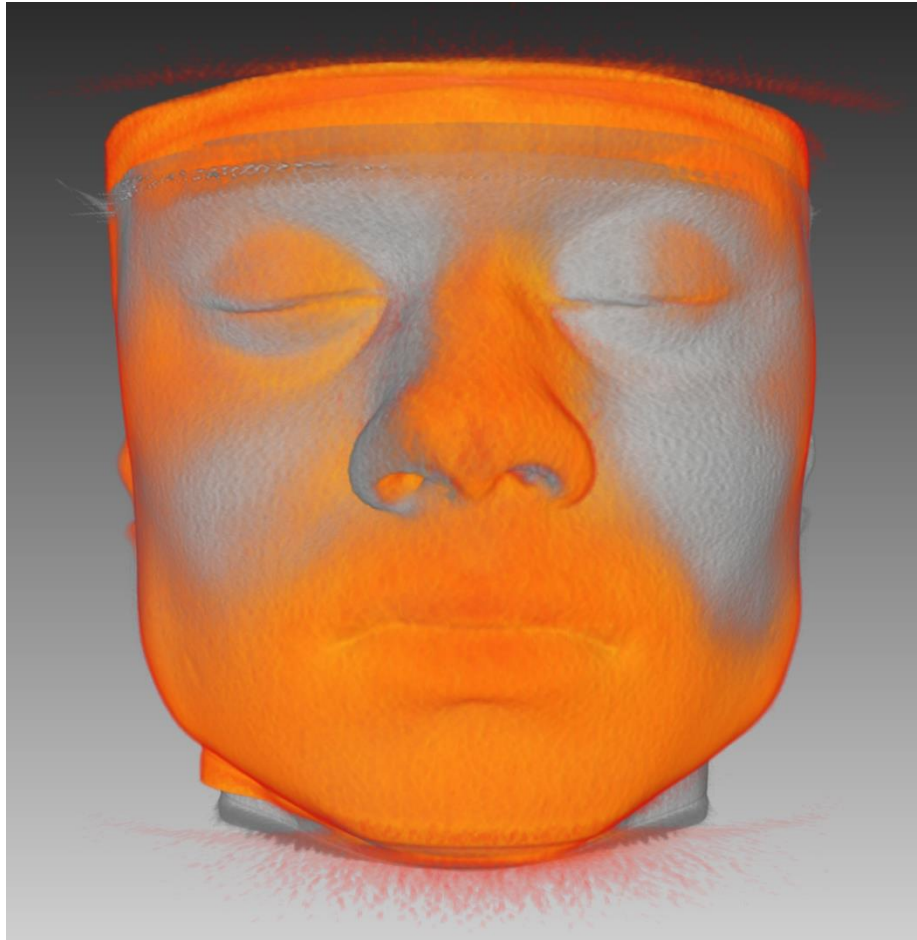


Figure 5-19. The registration is shown on the full patient scans. This scan is thresholded to identify changes in the facial proportions.



Figure 5-20. The registration is shown on the full patient scans. This scan is thresholded to identify changes in the position and skull changes as a result of growth.

The transformation matrix to register T2 to T1 is

$$M = \begin{bmatrix} 1 & 0 & 0 & 168 \\ 0 & 1 & 0 & 155.1 \\ 0 & 0 & 1 & 10.8 \\ 0 & 0 & 0 & 1 \end{bmatrix} \quad (5-4)$$

with the transformation matrix defined as in section 5.2.3 equation (5-1).

5.4 DISCUSSION

The increased use of 3D imaging in orthodontics, due to higher equipment availability and lower radiation dosage of CBCT machines, requires the development of novel image analysis methods. In orthodontics, superimposition, also known as registration, is the method of overlapping two scans of the same patient from different time steps in order to assess the changes that have occurred. This allows the orthodontist to make an informed decision for treatment. In the literature two registration methods are commonly used in orthodontics, MMI [5], [9] and the 6-point method by Lagraverre *et al.*[2], [3]. Both of these methods have benefits as well as detriments to their use. Chapter 2 discusses this in depth. A new registration method is put forward in this thesis.

5.4.1 TESTING ON CRANIAL BASES WITH KNOWN ERROR

The tests on the cranial base with known error used parameter settings of a sigma value of 81, windowing turned on and no thresholding. Each of the 5 cranial bases was registered 10 times (trials), creating 5 test sets (1 for each cranial base model used). The algorithm offered strong results. Only 6 of the 50 trials had an error larger than the maximum allowable error found using a Monte Carlo analysis. The maximum allowable error was found by introducing a small rotation (-2 to 2) per axis and a small translation (-2 to 2 voxels) per direction and finding the largest L2-norm any combination of the small rotations and translations. If the anomalous 4th test set is removed the percentage of trials that converged to the wrong solution drops to 5% (1 fail of 40 trials).

Since all the trials within a test set are the same cranial base image, the only variation is the initial conditions. This means that the initial conditions have an effect on the registration. Since the algorithm will always have identical results to identical input parameters a method of determining failure to converge and then performing a small change to the registering image would be beneficial. By causing a small change in an image set that fails to converge initially it may then converge on subsequent runs. This could be set up using landmarks within the skull. If the distance between landmarks is ever considered too large a small change can be introduced.

The failure to converge to the correct solution was not related to the magnitude of the correction required. If the rotations converged to the appropriate solution the translations will also be corrected for properly.

5.4.2 TESTING ON PATIENT T1 AND T2 DATA

When comparing the new method with the 6-point method, the new method had similar (defined as within 10% L2-norm) or better results in 4 of the 10 patient registrations. This is likely due to the higher potential accuracy of the point method. The point method can be as accurate as the researcher selecting landmarks, if the landmarks are selected by a clinician with experience in selecting landmarks and T1 and T2 of a scan are landmarked in close proximity this allows for highly accurate landmarks. In this study, this was the case, resulting in a strong registration. In orthodontic clinics it is sometimes the case that landmarking can be separated by a long period of time affecting repeatability of landmark placement. If landmarking is done as soon as the T1 scan is taken, and the T2 scan is not be taken for months the repeatability of landmark selection will be lower. This landmark error can be increased even more if different clinicians select the landmarks for T1 and T2 scans. The new method does not require any selection of landmarks.

The new registration method has a limit to the size of errors that can be found. This limit is decided both by the size of the image and the voxel size of the image. This is because the angle of correction required for rotations is computed from the phase correlation using equation (5-5) (from section 4.3.3).

$$\varphi = (S - 1) \frac{360}{N} \quad (5-5)$$

where N is the number of voxels in the φ direction and S is the shift found using the phase correlation. The shift S is always an integer. The precision of the angles that can effectively corrected is

$$\varphi_1 = \frac{360}{N} \quad (5-6)$$

which for a N value of 256 voxels is 1.4 degrees. If a larger image is used, increasing N , then smaller angles can be corrected for.

This is why the rotation in the illustrated example was not corrected for. Since the rotation in Figure 5-18 was approximated to be 1.5 degrees, the registration may not always detect this small angle of rotation. The only way to increase the accuracy of the registration is to increase the initial image size into the algorithm. Increasing the image size however increase the registration run time and increases the required technical specifications of the computer the registration is run on, specifically the memory (also known as RAM). Using a computer with 8GB of ram an image of 256x256x256 images converged in 50 seconds for the illustrated example, when the image size was increased to 360x360x360 voxels the computer ran out of RAM.

The new superimposition algorithm had an average CPU runtime 67% faster than the 6-point registration method, 6 minutes for the 6-point method and 2.6 minutes for the new method. The new superimposition also had less user involvement as only the cranial base had to be selected, and selection did not have to be exact. The only requirement during selection of the cranial base is that the T1 image in 256x256x256 voxels and the T2 image appear to falls entirely within the T1 volume. The 6-point method will also require selection of landmarks which will increase the time required for 6-point method to be used. In discussion with Dr. Lagravere, an expert of the 6-point method, the time required to select the landmarks required for the 6-point method ranges from 5 to 15 minutes depending on the number of points being landmarked and the difficulty in landmarking (Edmonton, 2016). This time does not include uploading or preparing visualization of the software.

The last registration method that sees common use in orthodontics is maximization of mutual information. One of the most common implementations is output by the University of North Carolina (UNC) [4, 5]. Nada *et al.* found in 2011 that registration with a method that “require[s] much less time” than the UNC method still had a time requirement of 30-40 minutes [10]. Cevidanes *et al.* stated in 2011 [11] that the registration procedure was time consuming and computing intensive. It is important to recognize that technological improvements over the past few years may have reduced the total time requirement of the UNC method. Using the results of Chapter 2, the UNC method claims to have sub-voxel registration.

The new registration method is not time consuming as no precise landmarks need to be selected, only the area of the skull containing the cranial base roughly selected. This process takes approximately five minutes for an experienced user (not including the time to upload the images to the computer or prepare the visualizations).

Comparing the 6-point registration, the new method, and the UNC method (using reports from literature as it was not tested in vivo for this comparison) with respect to accuracy, time, and user involvement is show in Table 5-5.

Table 5-5. Comparison of the 6-point registration and the new registration algorithm.

	6-Point Method	New Phase Correlation Algorithm	UNC Registration
Accuracy	Higher	Lower	Highest
Time	Slower	Faster	Slowest
User Involvement	Medium Involvement	Low Involvement	High Involvement

There is no single best registration method. Instead there are multiple methods that can be selected depending on the requirements of the situation. The new algorithm method improves over the 6-point registration in terms of runtime and user involvement. The 6-point algorithm has an improved accuracy.

A secondary technique can be used to allow the new algorithm to get higher accuracy. Since the initial registration from the new algorithm would allow for a general registration, the second registration could be bounded to only allow changes of a few voxels or degrees. This could allow for the new method to match or beat the 6-point method in accuracy. This extra registration would also still allow for retrieval of the transformation matrix.

5.5 CONCLUSION

The registration method performed well and is suitable for registration of patient T1 and T2 scans. The optimal settings for the scans are to filter the images with a Gaussian filter of strength 80. The registration should also be performed with windowing turned on and without thresholding the images.

When the registration was tested on cranial bases with known errors, compared to maximum allowed error calculated using Monte Carlo analysis, the success rate of the algorithm was 88%.

When compared to the 6-point registration technique the 6-point method had higher accuracy in 9 out of 10 cases. The 6-point method used images landmarked by an expert in the field over a short time frame. The new registration algorithm had a quicker runtime, and required less user interaction. In an illustrated patient example, the only error was an approximately 1.5 degree error in rotation due to the image resolution used. This error could potentially be reduced using a more refined image. The small rotation could also be compensated for by running a secondary registration, knowing that the method outlined in this thesis gives a strong initial guess.

5.6 REFERENCES

- [1] J. Huggare, “The handbook of cephalometric superimposition (2011),” *Eur. J. Orthod.*, vol. 34, no. 3, pp. 396–397, Jun. 2012.
- [2] A. DeCesare, M. Secanell, M. O. Lagravère, and J. Carey, “Multiobjective optimization framework for landmark measurement error correction in three-dimensional cephalometric tomography,” *Dento Maxillo Facial Radiol.*, vol. 42, no. 7, p. 20130035, 2013.
- [3] M. O. Lagravère, P. W. Major, and J. Carey, “Sensitivity analysis for plane orientation in three-dimensional cephalometric analysis based on superimposition of serial cone beam computed tomography images,” *Dentomaxillofacial Radiol.*, vol. 39, no. 7, pp. 400–408, Oct. 2010.
- [4] A. AlHadidi, L. H. Cevidanes, B. Paniagua, R. Cook, F. Festy, and D. Tyndall, “3D quantification of mandibular asymmetry using the SPHARM-PDM tool box,” *Int. J. Comput. Assist. Radiol. Surg.*, vol. 7, no. 2, pp. 265–271, Nov. 2011.
- [5] L. Cevidanes, L. Bailey, G. Tucker, M. Styner, A. Mol, C. Phillips, W. Proffit, and T. Turvey, “Superimposition of 3D cone-beam CT models of orthognathic surgery patients,” *Dentomaxillofacial Radiol.*, vol. 34, no. 6, pp. 369–375, Nov. 2005.
- [6] J. Bican and J. Flusser, “3D Rigid registration by cylindrical phase correlation method,” *Pattern Recognit. Lett.*, vol. 30, no. 10, pp. 914–921, Jul. 2009.
- [7] T. Nakamori, H. Okabayashi, and A. Kawanaka, “3-D object matching using phase correlation method,” in *Signal Processing (ICSP), 2010 IEEE 10th International Conference on*, 2010, pp. 1275–1278.
- [8] J. W. Young, “Head and Face Anthropometry of Adult U.S. Civilians,” Jul. 1993.
- [9] A. AlHadidi, L. H. Cevidanes, B. Paniagua, R. Cook, F. Festy, and D. Tyndall, “3D quantification of mandibular asymmetry using the SPHARM-PDM tool box,” *Int. J. Comput. Assist. Radiol. Surg.*, vol. 7, no. 2, pp. 265–271, Nov. 2011.

- [10] R. M. Nada, T. J. J. Maal, K. H. Breuning, S. J. Bergé, Y. A. Mostafa, and A. M. Kuijpers-Jagtman, “Accuracy and reproducibility of voxel based superimposition of cone beam computed tomography models on the anterior cranial base and the zygomatic arches,” *PloS One*, vol. 6, no. 2, p. e16520, 2011.
- [11] L. H. C. Cevidanes, A. E. F. Oliveira, D. Grauer, M. Styner, and W. R. Proffit, “Clinical application of 3D imaging for assessment of treatment outcomes,” *Semin. Orthod.*, vol. 17, no. 1, pp. 72–80, Mar. 2011.

6 CONCLUSIONS AND FUTURE WORK

6.1 CONCLUSION

The objective of this thesis was to develop and assess a new superimposition technique for use in orthodontic clinics. This new method was then tested on artificial data, then patient data. This included comparison to the 6-point registration method. The new method was focused on three factors, the accuracy of the superimposition, the speed of the superimposition, and the clinician involvement in the superimposition. If the technique is not accurate enough, the measurements between registered images will not be useful. If the registration is slow, it will be difficult to use in clinics. Lastly, if the registration algorithm is difficult to use or requires or has a steep learning curve it will be ignored in favour of methods which are easier to use.

A new superimposition method was designed and assessed. This included a review of the methods currently in practice and testing of a Cone-Beam Computed Tomography machine to understand the parameters that will influence superimposition techniques. A full mathematical proof including validation of the method is provided in chapter 4. The superimposition method is tested on patient cranial bases with known error and is also tested on patient scans from two different time steps and compared to the six point registration method.

A review of literature found that the most commonly used superimposition methods in orthodontics are point-based methods and maximization of mutual information (MMI). Both of these methods were reported to be useful and reliable. The point-based methods rely on a clinician to place landmarks on the volumes using specialized software and the inaccuracy in placing landmarks will affect the superimposition. MMI registers two images based off the relationship of greyscale values between them.

Testing of a CBCT machine was performed using a skull model inside a box of water to represent human tissue. Testing revealed that the accuracy of linear measurements is highly reliable, when viewed globally greyscale values are reliable, and when viewed locally grayscale values are not reliable. Unreliable greyscale values in small regions of interest mean that greyscale based superimposition techniques may have difficulty if the region used for the registration is small.

The superimposition algorithm was tested in three different manners. The first test was to find the optimal parameters for the algorithm, the second test found the ability of the algorithm to correct for known errors in patient cranial base scans, the third test compared to the registration algorithm to a point based method. The algorithm was found to have more error than the 6-point method, with the points selected by an expert in the field, in six of ten tests on previously acquired patient scans. The new algorithm performed better than the 6-point method in terms of user involvement, and speed of registration.

The superimposition method was able to register two images together successfully. The method was not able to achieve sub-voxel registration; a secondary superimposition technique will be required for that high a level of accuracy. Instead this superimposition method will allow for an automated method of getting two images in near alignment, allowing for a good starting pose for subsequent specialized registration algorithms.

With sub-voxel registration the algorithm presented in this thesis will be an invaluable tool in orthodontic clinics. It will be easy to use, not requiring any complex steps or selection of points. The results will be accurate, allowing for accurate measurements post registration. This will allow for improved patient treatment planning.

6.2 FUTURE WORK

The future work consists of:

- 1) Programming the algorithm into a new programming language, such as C++. This will allow for the algorithm to take advantage of both object oriented programming and increase its computation speed. This includes creating an easy to use GUI.
- 2) Introduce a secondary registration algorithm to allow for sub-voxel registration. The method introduced in this thesis will allow for a good initial guess to be found. The subsequent registration will be able to find an optimal solution quickly as tight bounds will exist (the allowable translation and rotation can be restricted to only a few voxels or degrees). This will require research and testing of the various registration methods that exist, or implementation of a new registration algorithm modified from methods that currently exist. This would allow for the method to be specialized to Cone-Beam CT acquired scans.

Bibliography

- AlHadidi, Abeer, Lucia H. Cevidanes, Beatriz Paniagua, Richard Cook, Frederic Festy, and Donald Tyndall. "3D Quantification of Mandibular Asymmetry Using the SPHARM-PDM Tool Box." *International Journal of Computer Assisted Radiology and Surgery* 7, no. 2 (November 17, 2011): 265–71. doi:10.1007/s11548-011-0665-2.
- Almukhtar, Anas, Xiangyang Ju, Balvinder Khambay, James McDonald, and Ashraf Ayoub. "Comparison of the Accuracy of Voxel Based Registration and Surface Based Registration for 3D Assessment of Surgical Change Following Orthognathic Surgery." *PLoS ONE* 9, no. 4 (April 2, 2014): e93402. doi:10.1371/journal.pone.0093402.
- Alsufyani, Noura A., Nicholas H. Dietrich, Manuel O. Lagravère, Jason P. Carey, and Paul W. Major. "Cone Beam Computed Tomography Registration for 3-D Airway Analysis Based on Anatomic Landmarks." *Oral Surgery, Oral Medicine, Oral Pathology and Oral Radiology* 118, no. 3 (September 2014): 371–83. doi:10.1016/j.oooo.2014.05.027.
- Baan, Frank, Jeroen Liebrechts, Tong Xi, Ruud Schreurs, Martien de Koning, Stefaan Bergé, and Thomas Maal. "A New 3D Tool for Assessing the Accuracy of Bimaxillary Surgery: The OrthoGnathicAnalyser." *PLoS ONE* 11, no. 2 (February 22, 2016). doi:10.1371/journal.pone.0149625.
- Besl, P. J., and H. D. McKay. "A Method for Registration of 3-D Shapes." *IEEE Transactions on Pattern Analysis and Machine Intelligence* 14, no. 2 (February 1992): 239–56. doi:10.1109/34.121791.
- Bican, Jakub, and Jan Flusser. "3D Rigid Registration by Cylindrical Phase Correlation Method." *Pattern Recognition Letters* 30, no. 10 (July 15, 2009): 914–21. doi:10.1016/j.patrec.2009.03.015.
- Bolanzadeh, N, W Bischof, C Flores-Mir, and P Boulanger. "Multimodal Registration of Three-Dimensional Maxillofacial Cone Beam CT and Photogrammetry Data over Time." *Dentomaxillofacial Radiology* 42, no. 2 (February 1, 2013): 22027087. doi:10.1259/dmfr/22027087.

- Brunetto, Daniel Paludo, Leandro Velasco, Leonardo Koerich, and Mônica Tirre de Souza Araújo. "Prediction of 3-Dimensional Pharyngeal Airway Changes after Orthognathic Surgery: A Preliminary Study." *American Journal of Orthodontics and Dentofacial Orthopedics* 146, no. 3 (September 2014): 299–309. doi:10.1016/j.ajodo.2014.05.024.
- Cevidanes, Lhs, Lj Bailey, Gr Tucker, Ma Styner, A Mol, Cl Phillips, Wr Proffit, and T Turvey. "Superimposition of 3D Cone-Beam CT Models of Orthognathic Surgery Patients." *Dentomaxillofacial Radiology* 34, no. 6 (November 1, 2005): 369–75. doi:10.1259/dmfr/17102411.
- Cevidanes, Lucia H.S., Abeer Alhadidi, Beatriz Paniagua, Martin Styner, John Ludlow, Andre Mol, Timothy Turvey, William R. Proffit, and Paul Emile Rossouw. "3D Quantification of Mandibular Asymmetry through Cone Beam Computed Tomography." *Oral Surgery, Oral Medicine, Oral Pathology, Oral Radiology, and Endodontics* 111, no. 6 (June 2011): 757–70. doi:10.1016/j.tripleo.2011.02.002.
- Cevidanes, Lucia H. S., L'Tanya J. Bailey, Scott F. Tucker, Martin A. Styner, Andre Mol, Ceib L. Phillips, William R. Proffit, and Timothy Turvey. "Three-Dimensional Cone-Beam Computed Tomography for Assessment of Mandibular Changes after Orthognathic Surgery." *American Journal of Orthodontics and Dentofacial Orthopedics : Official Publication of the American Association of Orthodontists, Its Constituent Societies, and the American Board of Orthodontics* 131, no. 1 (January 2007): 44–50. doi:10.1016/j.ajodo.2005.03.029.
- Cevidanes L. H. C., Oliveira, D A. E. F., Grauer, M. Styner, and Proffit W. R., "Clinical application of 3D imaging for assessment of treatment outcomes," *Semin. Orthod.*, vol. 17, no. 1, pp. 72–80, Mar. 2011.
- Cha, Bong Kuen, Jae Yong Lee, Paul-Georg Jost-Brinkmann, and Noriaki Yoshida. "Analysis of Tooth Movement in Extraction Cases Using Three-Dimensional Reverse Engineering Technology." *The European Journal of Orthodontics* 29, no. 4 (August 1, 2007): 325–31. doi:10.1093/ejo/cjm019.

Chang, Hsin-Wen, Hsiu-Hsia Lin, Peerasak Chortrakarnkij, Sun Goo Kim, and Lun-Jou Lo.

“Intraoperative Navigation for Single-Splint Two-Jaw Orthognathic Surgery: From Model to Actual Surgery.” *Journal of Cranio-Maxillofacial Surgery* 43, no. 7 (September 2015): 1119–26. doi:10.1016/j.jcms.2015.06.009.

Chen, Hui, Alan A. Lowe, Fernanda Riberiro de Almeida, Mary Wong, John A. Fleetham, and Bangkang Wang. “Three-Dimensional Computer-Assisted Study Model Analysis of Long-Term Oral-Appliance Wear. Part 1: Methodology.” *American Journal of Orthodontics and Dentofacial Orthopedics* 134, no. 3 (September 2008): 393–407. doi:10.1016/j.ajodo.2006.10.030.

da Motta, Alexandre Trindade Simões, Felipe de Assis Ribeiro Carvalho, Ana Emília Figueiredo Oliveira, Lúcia Helena Soares Cevitanes, and Marco Antonio de Oliveira Almeida. “Superimposition of 3D Cone-Beam CT Models in Orthognathic Surgery.” *Dental Press Journal of Orthodontics* 15, no. 2 (March 1, 2010): 39–41. doi:10.1590/S2176-94512010000200005.

DeCesare, A, M Secanell, Mo Lagravère, and J Carey. “Multiobjective Optimization Framework for Landmark Measurement Error Correction in Three-Dimensional Cephalometric Tomography.” *Dentomaxillofacial Radiology* 42, no. 7 (June 3, 2013): 20130035. doi:10.1259/dmfr.20130035.

S. Derrode and F. Ghorbel, “Robust and Efficient Fourier–Mellin Transform Approximations for Gray-Level Image Reconstruction and Complete Invariant Description,” *Comput. Vis. Image Underst.*, vol. 83, no. 1, pp. 57–78, Jul. 2001.

Essig, Harald, Majeed Rana, Horst Kokemueller, Christoph Zizelmann, Constantin von See, Martin Ruecker, Frank Tavassol, and Nils-Claudius Gellrich. “Referencing of Markerless CT Data Sets with Cone Beam Subvolume Including Registration Markers to Ease Computer-Assisted Surgery - A Clinical and Technical Research.” *The International Journal of Medical Robotics and Computer Assisted Surgery* 9, no. 3 (September 1, 2013): e39–45. doi:10.1002/rcs.1444.

- Farronato, Giampietro, Lucia Giannini, Guido Galbiati, Lucia Pisani, Carmen Mortellaro, and Cinzia Maspero. "Verification of the Reliability of the Three-Dimensional Virtual Presurgical Orthodontic Diagnostic Protocol." *The Journal of Craniofacial Surgery* 25, no. 6 (November 2014): 2013–16. doi:10.1097/SCS.0000000000001046.
- Garrett, Brett J., Joseph M. Caruso, Kitichai Rungcharassaeng, James R. Farrage, Jay S. Kim, and Guy D. Taylor. "Editor's Summary, Q & A, Reviewer's Critique: Skeletal Effects to the Maxilla after Rapid Maxillary Expansion Assessed with Cone-Beam Computed Tomography." *American Journal of Orthodontics and Dentofacial Orthopedics* 134, no. 1 (July 2008): 8–9. doi:10.1016/j.ajodo.2008.06.004.
- Gkantidis, Nikolaos, Michael Schauseil, Pawel Pazera, Berna Zorkun, Christos Katsaros, and Björn Ludwig. "Evaluation of 3-Dimensional Superimposition Techniques on Various Skeletal Structures of the Head Using Surface Models." *PLoS ONE* 10, no. 2 (February 23, 2015). doi:10.1371/journal.pone.0118810.
- Gonzalez, Ruben. "Improving Phase Correlation for Image Registration" in *Image And Vision Computing New Zealand 2011*, 2011 © IEEE. <http://hdl.handle.net/10072/44512>
- Gordon, Chad R., Ryan J. Murphy, Devin Coon, Ehsan Basafa, Yoshito Otake, Mohammed Al Rakan, Erin Rada, et al. "Preliminary Development of a Workstation for Craniomaxillofacial Surgical Procedures: Introducing a Computer-Assisted Planning and Execution System." *The Journal of Craniofacial Surgery* 25, no. 1 (January 2014): 273–83. doi:10.1097/SCS.0000000000000497.
- Grauer, Dan, Lucia S. H. Cevidanes, Martin A. Styner, Inam Heulfe, Eric T. Harmon, Hongtu Zhu, and William R. Proffit. "Accuracy and Landmark Error Calculation Using Cone-Beam Computed Tomography–Generated Cephalograms." *The Angle Orthodontist* 80, no. 2 (November 11, 2009): 286–94. doi:10.2319/030909-135.1.
- Gribel, Bruno Frazão, Marcos Nadler Gribel, Diogo Campos Frazão, James A. McNamara, and Flavio Ricardo Manzi. "Accuracy and Reliability of Craniometric Measurements on Lateral Cephalometry and 3D Measurements on CBCT Scans." *The Angle Orthodontist* 81, no. 1 (October 11, 2010): 26–35. doi:10.2319/032210-166.1.

- Hanzelka, Tomas, Jaroslav Dusek, Filip Ocasek, Josef Kucera, Jiri Sedy, Jiri Benes, Gabriela Pavlikova, and Rene Foltan. "Movement of the Patient and the Cone Beam Computed Tomography Scanner: Objectives and Possible Solutions." *Oral Surgery, Oral Medicine, Oral Pathology and Oral Radiology* 116, no. 6 (December 2013): 769–73.
doi:10.1016/j.oooo.2013.08.010.
- Hartley, Ralph VL. "Transmission of Information." *Bell System Technical Journal* 7.3 (1928): 535–63.
- Hassan, Bassam, Paul van der Stelt, and Gerard Sanderink. "Accuracy of Three-Dimensional Measurements Obtained from Cone Beam Computed Tomography Surface-Rendered Images for Cephalometric Analysis: Influence of Patient Scanning Position." *The European Journal of Orthodontics* 31, no. 2 (April 1, 2009): 129–34.
doi:10.1093/ejo/cjn088.
- Huggare, Jan. "The Handbook of Cephalometric Superimposition (2011)." *The European Journal of Orthodontics* 34, no. 3 (June 1, 2012): 396–97. doi:10.1093/ejo/cjs024.
- Hwang, Jae Joon, Kee-Deog Kim, Hyok Park, Chang Seo Park, and Ho-Gul Jeong. "Factors Influencing Superimposition Error of 3D Cephalometric Landmarks by Plane Orientation Method Using 4 Reference Points: 4 Point Superimposition Error Regression Model." *PLoS ONE* 9, no. 11 (November 5, 2014): e110665. doi:10.1371/journal.pone.0110665.
- Jacquet, W, E Nyssen, P Bottenberg, P de Groen, and B Vande Vannet. "Novel Information Theory Based Method for Superimposition of Lateral Head Radiographs and Cone Beam Computed Tomography Images." *Dentomaxillofacial Radiology* 39, no. 4 (May 2010): 191–98. doi:10.1259/dmfr/58457270.
- Kamburoglu, Kivanç, Sema Murat, Eray Kolsuz, Hakan Kurt, Selcen Yüksel, and Candan Paksoy. "Comparative Assessment of Subjective Image Quality of Cross-Sectional Cone-Beam Computed Tomography Scans." *Journal of Oral Science* 53, no. 4 (2011): 501–8.
doi:10.2334/josnurd.53.501.

- Kang, Sang-Hoon, Moon-Key Kim, Jin-Hong Kim, Hee-Keun Park, Sang-Hwy Lee, and Wonse Park. "The Validity of Marker Registration for an Optimal Integration Method in Mandibular Navigation Surgery." *Journal of Oral and Maxillofacial Surgery* 71, no. 2 (February 2013): 366–75. doi:10.1016/j.joms.2012.03.037.
- Kang, Sang-Hoon, Jae-Won Lee, and Moon-Key Kim. "Use of the Surface-Based Registration Function of Computer-Aided Design/computer-Aided Manufacturing Software in Medical Simulation Software for Three-Dimensional Simulation of Orthognathic Surgery." *Journal of the Korean Association of Oral and Maxillofacial Surgeons* 39, no. 4 (August 2013): 197–99. doi:10.5125/jkaoms.2013.39.4.197.
- Lagravère, Manuel O., Jason Carey, Roger W. Toogood, and Paul W. Major. "Three-Dimensional Accuracy of Measurements Made with Software on Cone-Beam Computed Tomography Images." *American Journal of Orthodontics and Dentofacial Orthopedics* 134, no. 1 (July 2008): 112–16. doi:10.1016/j.ajodo.2006.08.024.
- Lagravère, Manuel O., Jillian M. Gordon, Carlos Flores-Mir, Jason Carey, Giseon Heo, and Paul W. Major. "Cranial Base Foramen Location Accuracy and Reliability in Cone-Beam Computerized Tomography." *American Journal of Orthodontics and Dentofacial Orthopedics* 139, no. 3 (March 2011): e203–10. doi:10.1016/j.ajodo.2009.06.027.
- Lagravère, M O, P W Major, and J Carey. "Sensitivity Analysis for Plane Orientation in Three-Dimensional Cephalometric Analysis Based on Superimposition of Serial Cone Beam Computed Tomography Images." *Dentomaxillofacial Radiology* 39, no. 7 (October 1, 2010): 400–408. doi:10.1259/dmfr/17319459.
- Lee, Robert J., Andre Weissheimer, John Pham, Leslie Go, Luciane Macedo de Menezes, W. Ronald Redmond, James F. Loos, Glenn T. Sameshima, and Hongsheng Tong. "Three-Dimensional Monitoring of Root Movement during Orthodontic Treatment." *American Journal of Orthodontics and Dentofacial Orthopedics* 147, no. 1 (January 2015): 132–42. doi:10.1016/j.ajodo.2014.10.010.

- Lemieux, Genevieve, Jason P. Carey, Carlos Flores-Mir, Marc Secanell, Adam Hart, Nicholas Dietrich, and Manuel O. Lagravère-Vich. "Three-Dimensional Cephalometric Superimposition of the Nasomaxillary Complex." *American Journal of Orthodontics and Dentofacial Orthopedics* 146, no. 6 (December 2014): 758–64. doi:10.1016/j.ajodo.2014.08.014.
- Li, Gang. "Patient Radiation Dose and Protection from Cone-Beam Computed Tomography." *Imaging Science in Dentistry* 43, no. 2 (June 2013): 63–69. doi:10.5624/isd.2013.43.2.63.
- Lin, X., T. Chen, J. Liu, T. Jiang, D. Yu, and S. G. F. Shen. "Point-Based Superimposition of a Digital Dental Model on to a Three-Dimensional Computed Tomographic Skull: An Accuracy Study in Vitro." *British Journal of Oral and Maxillofacial Surgery* 53, no. 1 (January 2015): 28–33. doi:10.1016/j.bjoms.2014.09.007.
- Liu, Yi, Raphael Olszewski, Emanuel Stefan Alexandroni, Reyes Enciso, Tianmin Xu, and James K. Mah. "The Validity of In Vivo Tooth Volume Determinations From Cone-Beam Computed Tomography." *The Angle Orthodontist* 80, no. 1 (October 5, 2009): 160–66. doi:10.2319/121608-639.1.
- Ludlow, John B., and Cameron Walker. "Assessment of Phantom Dosimetry and Image Quality of I-CAT FLX Cone-Beam Computed Tomography." *American Journal of Orthodontics and Dentofacial Orthopedics* 144, no. 6 (December 2013): 802–17. doi:10.1016/j.ajodo.2013.07.013.
- Magnusson, Anders, Krister Bjerklin, Hyungmin Kim, Peter Nilsson, and Agneta Marcusson. "Three-Dimensional Assessment of Transverse Skeletal Changes after Surgically Assisted Rapid Maxillary Expansion and Orthodontic Treatment: A Prospective Computerized Tomography Study." *American Journal of Orthodontics and Dentofacial Orthopedics* 142, no. 6 (December 2012): 825–33. doi:10.1016/j.ajodo.2012.08.015.

- Magnusson, Anders, Krister Bjerklin, Hyungmin Kim, Peter Nilsson, and Agneta Marcusson. "Three-Dimensional Computed Tomographic Analysis of Changes to the External Features of the Nose after Surgically Assisted Rapid Maxillary Expansion and Orthodontic Treatment: A Prospective Longitudinal Study." *American Journal of Orthodontics and Dentofacial Orthopedics* 144, no. 3 (September 2013): 404–13. doi:10.1016/j.ajodo.2013.04.013.
- Nada R. M., Maal T. J. J., Breuning K. H., Bergé S. J., Mostafa Y. A., and Kuijpers-Jagtman A. M., "Accuracy and reproducibility of voxel based superimposition of cone beam computed tomography models on the anterior cranial base and the zygomatic arches," *PloS One*, vol. 6, no. 2, p. e16520, 2011.
- Nadjmi, Nasser, Ellen Defrancq, Wouter Mollemans, Geert Van Hemelen, and Stefaan Bergé. "Quantitative Validation of a Computer-Aided Maxillofacial Planning System, Focusing on Soft Tissue Deformations." *Annals of Maxillofacial Surgery* 4, no. 2 (2014): 171–75. doi:10.4103/2231-0746.147112.
- Naji, Pegah, Noura A. Alsufyani, and Manuel O. Lagravère. "Reliability of Anatomic Structures as Landmarks in Three-Dimensional Cephalometric Analysis Using CBCT." *The Angle Orthodontist* 84, no. 5 (December 23, 2013): 762–72. doi:10.2319/090413-652.1.
- Nakamori, T., H. Okabayashi, and A. Kawanaka. "3-D Object Matching Using Phase Correlation Method." In *2010 IEEE 10th International Conference on Signal Processing (ICSP)*, 1275–78, 2010. doi:10.1109/ICOSP.2010.5656976.
- Osgood B. EE261 The Fourier Transform and its Applications [Internet]. Lecture notes presented at; 2007; Stanford University. [cited 2015 Sept 15]. p. 350-351. Available from: <http://tinyurl.com/pehdbxy>
- Othman, Asem Awaad, Amr Ragab El-Beialy, Sahar Ali Fawzy, Ahmed Hisham Kandil, Ahmed Mohammed El-Bialy, and Yehya Ahmed Mostafa. "Methods for Managing 3-Dimensional Volumes." *American Journal of Orthodontics and Dentofacial Orthopedics* 137, no. 2 (February 2010): 266–73. doi:10.1016/j.ajodo.2009.01.024.

- Otsu, Nobuyuki . "A Threshold Selection Method from Gray-Level Histograms," in *Systems, Man and Cybernetics, IEEE Transactions on* , vol.9, no.1, pp.62-66, Jan. 1979 doi: 10.1109/TSMC.1979.4310076
- Pangrazio-Kulbersh, Valmy, Paul Wine, Mariana Haughey, Brynn Pajtas, and Richard Kaczynski. "Cone Beam Computed Tomography Evaluation of Changes in the Naso-Maxillary Complex Associated with Two Types of Maxillary Expanders." *The Angle Orthodontist* 82, no. 3 (October 27, 2011): 448–57. doi:10.2319/072211-464.1.
- Park, Seongjin, Ho Chul Kang, Jeongjin Lee, Juneseuk Shin, and Yeong Gil Shin. "An Enhanced Method for Registration of Dental Surfaces Partially Scanned by a 3D Dental Laser Scanning." *Computer Methods and Programs in Biomedicine* 118, no. 1 (January 2015): 11–22. doi:10.1016/j.cmpb.2014.09.007.
- Park, Soo-Byung, Jong-Kyoon Yoon, Yong-Il Kim, Dae-Seok Hwang, Bong-Hae Cho, and Woo-Sung Son. "The Evaluation of the Nasal Morphologic Changes after Bimaxillary Surgery in Skeletal Class III Malocclusion by Using the Superimposition of Cone-Beam Computed Tomography (CBCT) Volumes." *Journal of Cranio-Maxillofacial Surgery* 40, no. 4 (June 2012): e87–92. doi:10.1016/j.jcms.2011.05.008.
- Park, Tae-Joon, Sang-Hyun Lee, and Ki-Soo Lee. "A Method for Mandibular Dental Arch Superimposition Using 3D Cone Beam CT and Orthodontic 3D Digital Model." *Korean Journal of Orthodontics* 42, no. 4 (August 2012): 169–81. doi:10.4041/kjod.2012.42.4.169.
- Periago, Danielle R., William C. Scarfe, Mazyar Moshiri, James P. Scheetz, Anibal M. Silveira, and Allan G. Farman. "Linear Accuracy and Reliability of Cone Beam CT Derived 3-Dimensional Images Constructed Using an Orthodontic Volumetric Rendering Program." *The Angle Orthodontist* 78, no. 3 (May 1, 2008): 387–95. doi:10.2319/122106-52.1.
- Pluim, J. P. W., J. B. A. Maintz, and M. A. Viergever. "Mutual-Information-Based Registration of Medical Images: A Survey." *IEEE Transactions on Medical Imaging* 22, no. 8 (August 2003): 986–1004. doi:10.1109/TMI.2003.815867.
- Prince, Jerry L., and Jonathan M. Links. *Medical Imaging Signals and Systems*. Pearson Education, 2014.

- Rino Neto, José, Fernando Penteado Lopes da Silva, Israel Chilvarquer, João Batista de Paiva, and Angélica Maria Hernandez. "Hausdorff Distance Evaluation of Orthodontic Accessories' Streaking Artifacts in 3D Model Superimposition." *Brazilian Oral Research* 26, no. 5 (October 2012): 450–56. doi:10.1590/S1806-83242012000500012.
- Rogers, Sheelagh A., Nicholas Drage, and Peter Durning. "Incidental Findings Arising with Cone Beam Computed Tomography Imaging of the Orthodontic Patient." *The Angle Orthodontist* 81, no. 2 (January 5, 2011): 350–55. doi:10.2319/032210-165.1.
- Romero-Delmastro, Alejandro, Onur Kadioglu, G. Frans Currier, and Tanner Cook. "Digital Tooth-Based Superimposition Method for Assessment of Alveolar Bone Levels on Cone-Beam Computed Tomography Images." *American Journal of Orthodontics and Dentofacial Orthopedics* 146, no. 2 (August 2014): 255–63. doi:10.1016/j.ajodo.2014.05.001.
- Rusinkiewicz, S., and M. Levoy. "Efficient Variants of the ICP Algorithm." In *Third International Conference on 3-D Digital Imaging and Modeling, 2001. Proceedings*, 145–52, 2001. doi:10.1109/IM.2001.924423.
- Scarfe, William C., and Allan G. Farman. "What Is Cone-Beam CT and How Does It Work?" *Dental Clinics of North America, Contemporary Dental and Maxillofacial Imaging*, 52, no. 4 (October 2008): 707–30. doi:10.1016/j.cden.2008.05.005.
- Shafi, M. I., A. Ayoub, X. Ju, and B. Khambay. "The Accuracy of Three-Dimensional Prediction Planning for the Surgical Correction of Facial Deformities Using Maxilim." *International Journal of Oral and Maxillofacial Surgery* 42, no. 7 (July 2013): 801–6. doi:10.1016/j.ijom.2013.01.015.
- Shannon, C. E. "A Mathematical Theory of Communication." *SIGMOBILE Mob. Comput. Commun. Rev.* 5, no. 1 (January 2001): 3–55. doi:10.1145/584091.584093.
- Spin-Neto, R, E Gotfredsen, and A Wenzel. "Variation in Voxel Value Distribution and Effect of Time between Exposures in Six CBCT Units." *Dentomaxillofacial Radiology* 43, no. 4 (February 3, 2014): 20130376. doi:10.1259/dmfr.20130376.

- Sun, Yi, Heinz-Theo Luebbbers, and Constantinus Politis. "Three-Dimensional Virtual Model Surgery to Fabricate the Digital Intermediate Splint." *Journal of Craniofacial Surgery* 24, no. 2 (March 2013): 563–65. doi:10.1097/SCS.0b013e3182700e4f.
- Swennen, G. R. J., E. -L. Barth, C. Eulzer, and F. Schutyser. "The Use of a New 3D Splint and Double CT Scan Procedure to Obtain an Accurate Anatomic Virtual Augmented Model of the Skull." *International Journal of Oral and Maxillofacial Surgery* 36, no. 2 (February 2007): 146–52. doi:10.1016/j.ijom.2006.09.019.
- Swennen, G. R. J., M. Y. Mommaerts, J. Abeloos, C. De Clercq, P. Lamoral, N. Neyt, J. Casselman, and F. Schutyser. "A Cone-Beam CT Based Technique to Augment the 3D Virtual Skull Model with a Detailed Dental Surface." *International Journal of Oral and Maxillofacial Surgery* 38, no. 1 (January 2009): 48–57. doi:10.1016/j.ijom.2008.11.006.
- Swennen, Gwen R. J., Wouter Mollemans, Calix De Clercq, Johan Abeloos, Philippe Lamoral, Frank Lippens, Nathalie Neyt, Jan Casselman, and Filip Schutyser. "A Cone-Beam Computed Tomography Triple Scan Procedure to Obtain a Three-Dimensional Augmented Virtual Skull Model Appropriate for Orthognathic Surgery Planning." *Journal of Craniofacial Surgery* 20, no. 2 (March 2009): 297–307. doi:10.1097/SCS.0b013e3181996803.
- Swennen, Gwen R. J., Maurice Y. Mommaerts, Johan Abeloos, Calix De Clercq, Philippe Lamoral, Nathalie Neyt, Jan Casselman, and Filip Schutyser. "The Use of a Wax Bite Wafer and a Double Computed Tomography Scan Procedure to Obtain a Three-Dimensional Augmented Virtual Skull Model." *Journal of Craniofacial Surgery* 18, no. 3 (May 2007): 533–39. doi:10.1097/scs.0b013e31805343df.
- Uechi, J., Y. Tsuji, M. Konno, K. Hayashi, T. Shibata, E. Nakayama, and I. Mizoguchi. "Generation of Virtual Models for Planning Orthognathic Surgery Using a Modified Multimodal Image Fusion Technique." *International Journal of Oral and Maxillofacial Surgery* 44, no. 4 (April 2015): 462–69. doi:10.1016/j.ijom.2014.11.007.

- Uechi, Jun, Miki Okayama, Takanori Shibata, Takeshi Muguruma, Kazuo Hayashi, Kazuhiko Endo, and Itaru Mizoguchi. "A Novel Method for the 3-Dimensional Simulation of Orthognathic Surgery by Using a Multimodal Image-Fusion Technique." *American Journal of Orthodontics and Dentofacial Orthopedics* 130, no. 6 (December 2006): 786–98. doi:10.1016/j.ajodo.2006.03.025.
- Viola, P., and W. M. Wells. "Alignment by Maximization of Mutual Information." In , *Fifth International Conference on Computer Vision, 1995. Proceedings*, 16–23, 1995. doi:10.1109/ICCV.1995.466930.
- Weissheimer, A., L. M. Menezes, L. Koerich, J. Pham, and L. H. S. Cevidanés. "Fast Three-Dimensional Superimposition of Cone Beam Computed Tomography for Orthopaedics and Orthognathic Surgery Evaluation." *International Journal of Oral and Maxillofacial Surgery* 44, no. 9 (September 2015): 1188–96. doi:10.1016/j.ijom.2015.04.001.
- Young, Joseph W. "Head and Face Anthropometry of Adult U.S. Civilians," July 1993.
- Zizelmann, Christoph, Beat Hammer, Nils-Claudius Gellrich, Rainer Schwestka-Polly, Majeed Rana, and Peter Bucher. "An Evaluation of Face-Bow Transfer for the Planning of Orthognathic Surgery." *Journal of Oral and Maxillofacial Surgery* 70, no. 8 (August 2012): 1944–50. doi:10.1016/j.joms.2011.08.025.

Appendix A – Supplemental Results and Data from the Testing of the Registration Algorithm

A.1 PLOTS AND STATISTICS OF THE MONTE CARLO ANALYSIS

Figure A. 1 through Figure A. 5 display the histograms resulting from the Monte Carlo analysis in section 5.3.1. The 100 results of the Monte Carlo analysis are divided into 20 bins. The 100 tests for each cranial base were created by taking a cranial base image then introducing a small skew of up to $\pm 2^\circ$ per axis and ± 2 voxels shift per a direction. The L2-norm was then computed between the original and skewed cranial base volumes. Table A. 1 Descriptive statistics of the Monte Carlo analysis for each cranial base shows the descriptive statistics for each of the 5 cranial base Monte Carlo results.

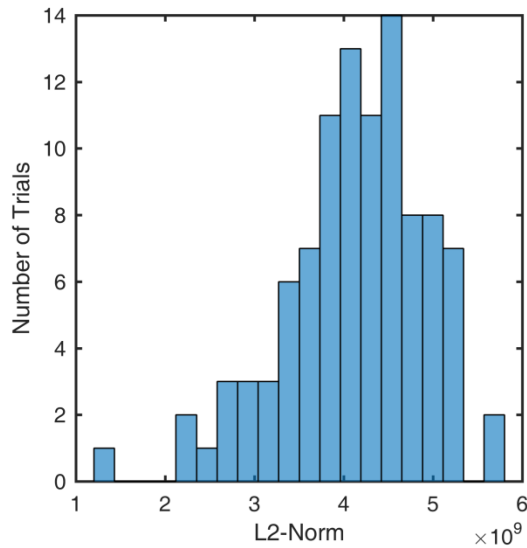


Figure A. 1 Histogram of Monte Carlo results for cranial base #1

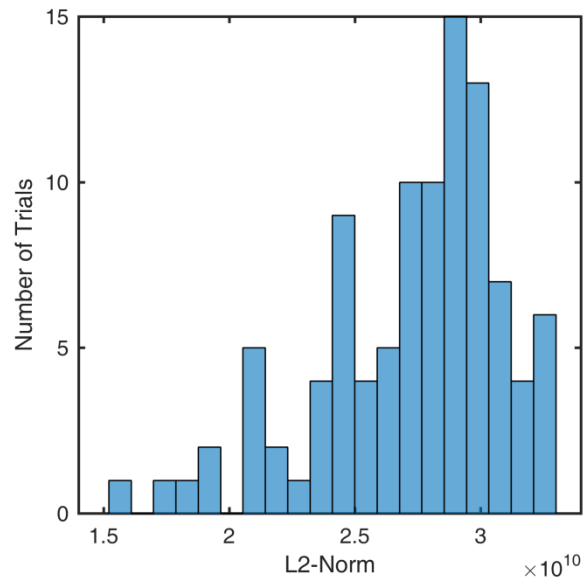


Figure A. 2 Histogram of Monte Carlo results for cranial base #2

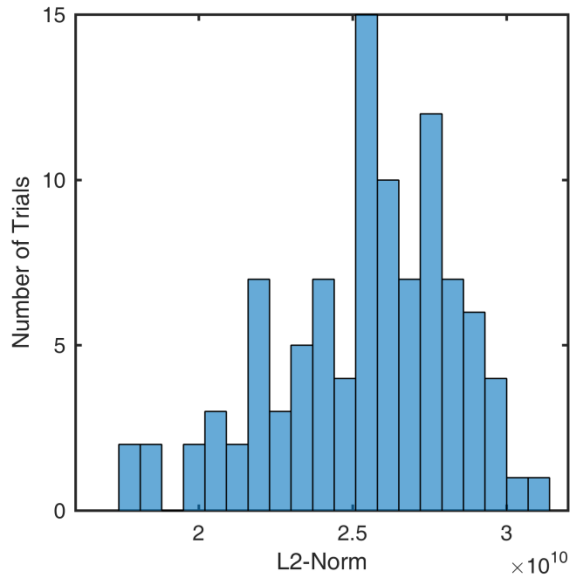


Figure A. 3 Histogram of Monte Carlo results for cranial base #3

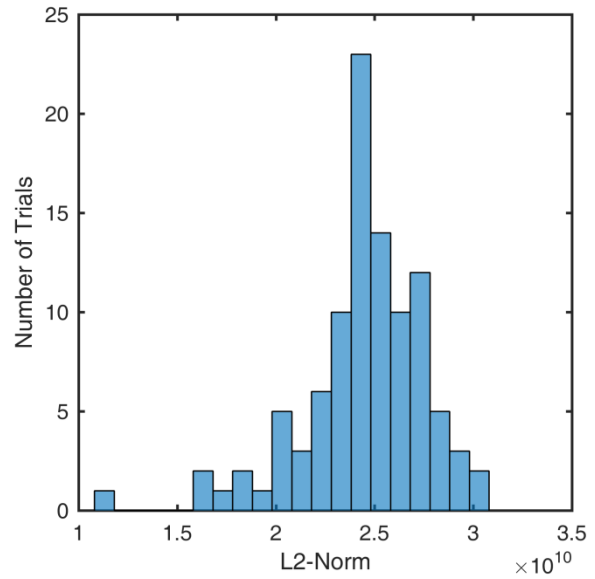


Figure A. 4 Histogram of Monte Carlo results for cranial base #4

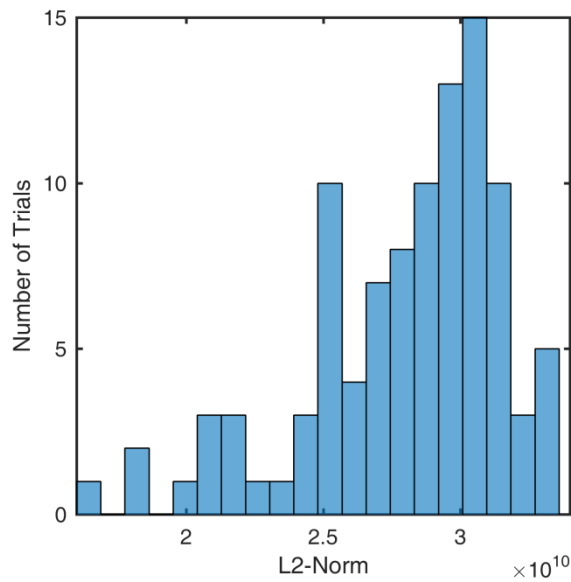


Figure A. 5 Histogram of Monte Carlo Analysis Results for Cranial Base #5

Table A. 1 Descriptive statistics of the Monte Carlo analysis for each cranial base

Cranial Base	Average ($\times 10^9$)	Median ($\times 10^9$)	Standard Deviation ($\times 10^9$)
1	4.13	4.19	0.797
2	27.3	27.9	3.67
3	25.4	25.8	2.94
4	24.5	24.7	3.12
5	28.0	28.9	3.55

A.2 CRANIAL BASE MODELS USED TO TEST NEW METHOD VS 6-POINT METHOD.

The cranial base models used for testing the new algorithm versus the 6-point method in section 5.3.3 are shown in a superior view in Figure A. 6 through Figure A. 25. The time 1 cranial bases are size 256x256x256, the time 2 cranial bases are an arbitrary smaller size. Time 1 is always the gold standard image, time 2 is registered to match time 1.



Figure A. 6. Cranial Base for Patient 1 Time 1

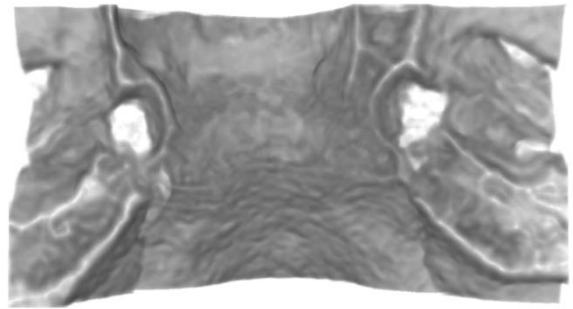


Figure A. 7. Cranial Base for Patient 1 Time 2



Figure A. 8. Cranial Base for Patient 2 Time 1

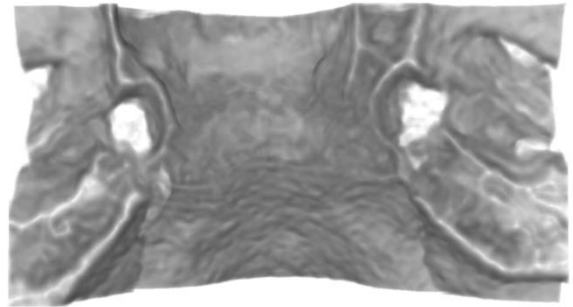


Figure A. 9. Cranial Base for Patient 2 Time 2

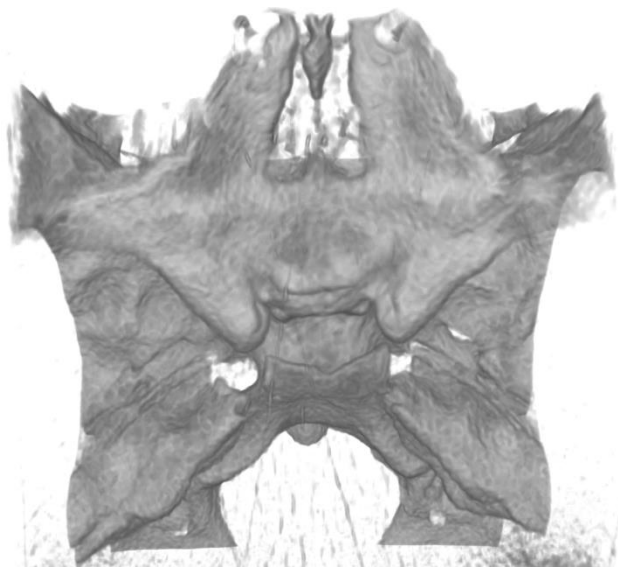


Figure A. 10. Cranial Base for Patient 3 Time 1

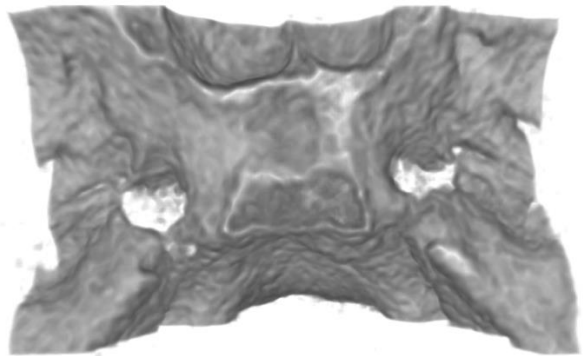


Figure A. 11. Cranial Base for Patient 3 Time 2

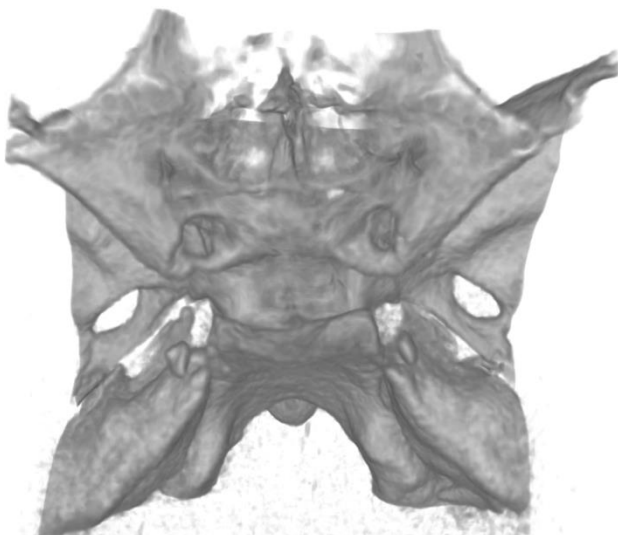


Figure A. 12. Cranial Base for Patient 4 Time 1

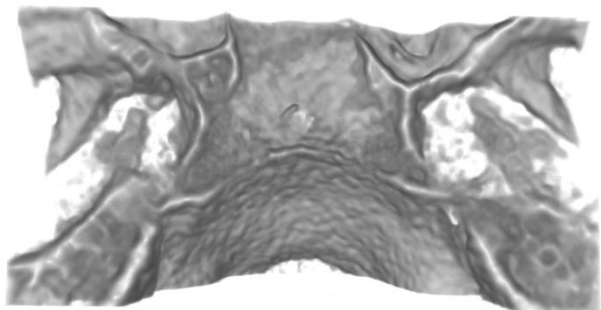


Figure A. 13. Cranial Base for Patient 4 Time 2

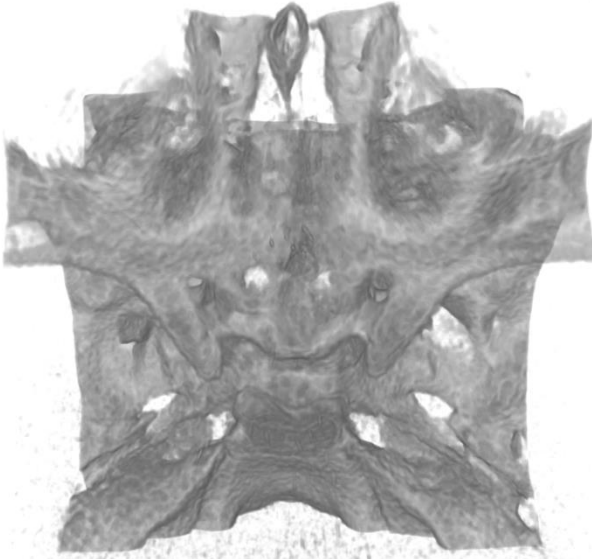


Figure A. 14. Cranial Base for Patient 5 Time 1

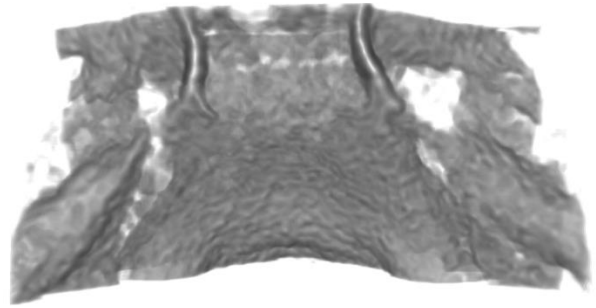


Figure A. 15. Cranial Base for Patient 5 Time 2

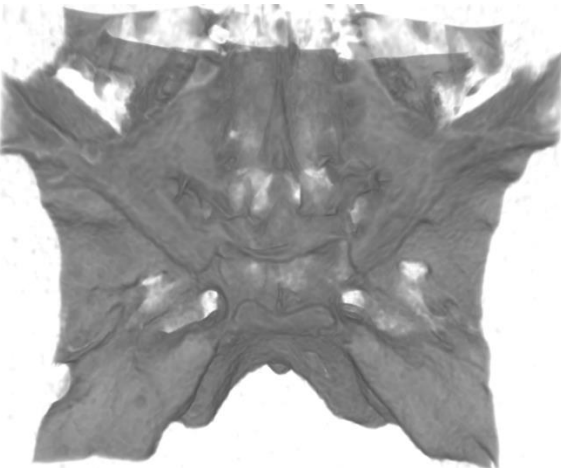


Figure A. 16. Cranial Base for Patient 6 Time 1

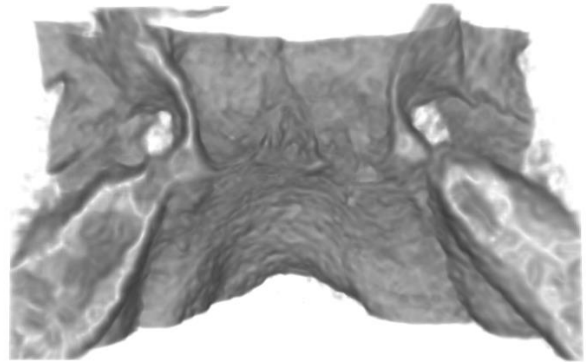


Figure A. 17. Cranial Base for Patient 6 Time 2

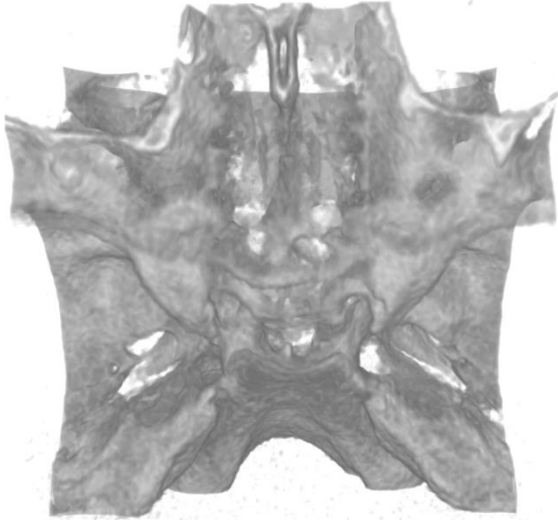


Figure A. 18. Cranial Base for Patient 7 Time 1

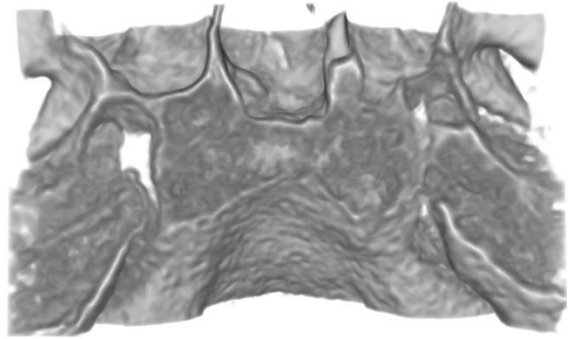


Figure A. 19. Cranial Base for Patient 7 Time 2

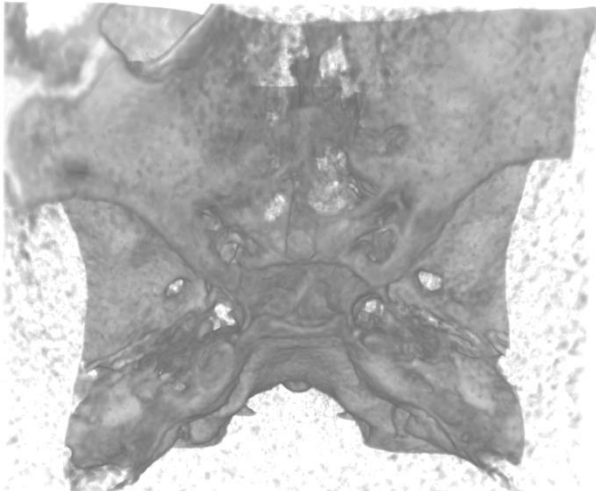


Figure A. 20. Cranial Base for Patient 8 Time 1

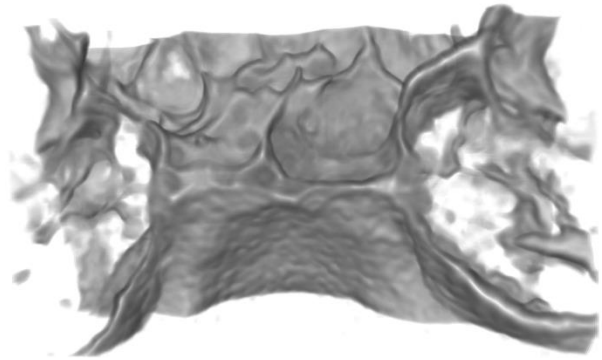


Figure A. 21. Cranial Base for Patient 8 Time 2

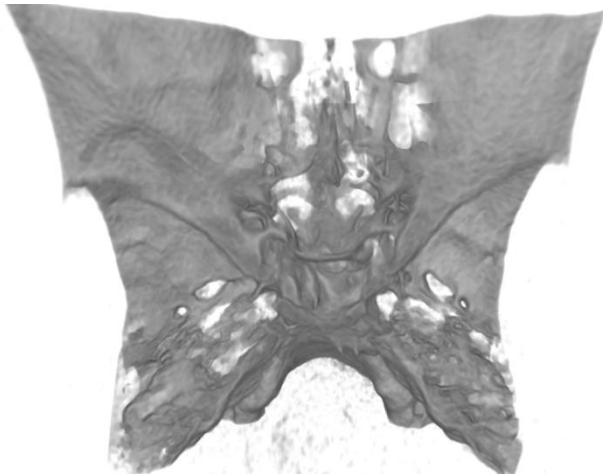


Figure A. 22. Cranial Base for Patient 9 Time 1

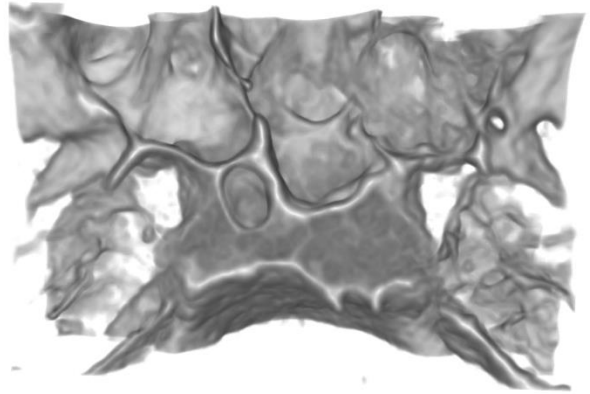


Figure A. 23. Cranial Base for Patient 9 Time 2

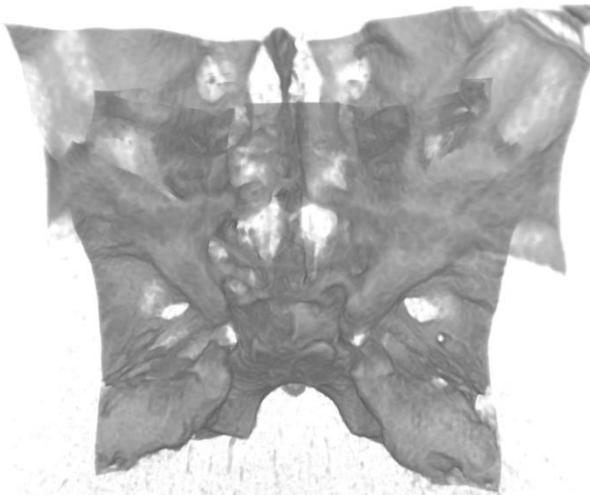


Figure A. 24. Cranial Base for Patient 10 Time 1

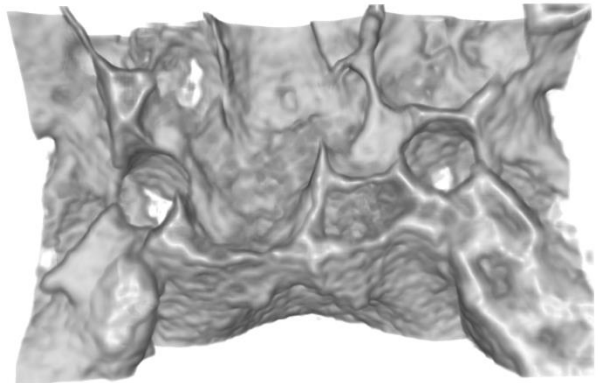


Figure A. 25. Cranial Base for Patient 10 Time 2

A.3 INPUT DATA FOR THE 6-POINT REGISTRATION METHOD

The 6-point registration method only uses points to register two images as opposed to the actual CBCT scans. The points must be measured in an external software program. The points used in the 6-point registration method have been validated in [1]. The 6-point method reduces the landmark placement error due to human bias and accuracy. The landmark coordinates are also converted to the anatomical coordinate system defined in [2]. The points used for the registration are:

- ELSA – defined as the midpoint between the left and right foramen spinosum
- Left and right auditory external meatus (AEML and AEMR respectively)
- Medial Foramen Magnum (MFM)
- Left and right Foramen Ovale (FOL and FOR respectively)

The measured coordinates, in millimetres, in the global coordinate system (x,y,z) are shown in Table A. 2 for all ten patients, T1 and T2.

Table A. 2 Global coordinates of all the landmarks used in the 6-point optimization

Patient	Landmark Name	Landmark Number	x_1 (mm)	y_1 (mm)	z_1 (mm)	x_2 (mm)	y_2 (mm)	z_2 (mm)
1	ELSA	1	-21.13	-2.64	44.80	-192.77	-151.54	68.50
1	FOR	2	-42.87	-5.42	45.70	-213.64	-156.64	70.00
1	FOL	3	0.96	-5.35	46.90	-169.66	-153.69	68.80
1	MFM	4	-20.09	12.73	23.80	-192.98	-134.11	49.30
1	AEMR	5	-66.01	11.54	47.17	-240.90	-141.49	76.81
1	AEML	6	22.62	11.54	48.67	-142.98	-135.80	72.32
2	ELSA	1	-267.72	-276.70	32.95	-191.13	-168.78	66.25
2	FOR	2	-292.45	-279.77	34.30	-216.39	-172.49	67.60
2	FOL	3	-241.91	-279.03	32.50	-165.22	-169.90	66.40
2	MFM	4	-268.42	-258.92	18.10	-192.14	-153.42	48.70
2	AEMR	5	-320.33	-258.61	42.65	-248.39	-153.16	70.82
2	AEML	6	-211.57	-260.71	31.87	-139.69	-148.97	68.43

3	ELSA	1	-21.79	5.18	57.10	-192.09	-162.61	72.25
3	FOR	2	-48.53	-0.27	57.40	-219.50	-170.30	72.10
3	FOL	3	4.54	1.78	58.00	-166.17	-165.24	71.50
3	MFM	4	-21.15	14.85	36.40	-193.38	-149.29	53.20
3	AEMR	5	-74.40	20.22	54.36	-248.69	-150.47	75.31
3	AEML	6	30.70	22.92	56.75	-139.99	-142.98	72.32
4	ELSA	1	-21.72	2.94	62.75	-189.66	-150.81	59.05
4	FOR	2	-46.71	-5.77	66.50	-215.31	-159.18	63.70
4	FOL	3	5.45	0.39	63.25	-161.47	-155.30	60.40
4	MFM	4	-21.93	14.39	46.75	-189.18	-141.09	42.40
4	AEMR	5	-77.66	14.70	67.44	-248.09	-138.19	61.84
4	AEML	6	28.42	26.93	64.44	-139.09	-130.11	60.64
5	ELSA	1	-19.26	7.95	57.55	-191.47	-146.40	60.10
5	FOR	2	-42.47	4.25	57.40	-214.76	-152.32	60.70
5	FOL	3	5.72	3.43	60.10	-165.81	-149.88	61.90
5	MFM	4	-16.53	23.55	43.60	-190.23	-129.90	46.00
5	AEMR	5	-68.71	27.71	61.84	-243.00	-130.11	66.63
5	AEML	6	35.50	25.02	63.34	-138.79	-127.41	66.63

6	ELSA	1	-191.77	-147.33	66.55	-192.68	-148.65	53.20
6	FOR	2	-215.40	-154.95	65.80	-216.54	-155.91	52.00
6	FOL	3	-166.01	-152.34	67.60	-167.46	-152.86	55.00
6	MFM	4	-190.73	-132.45	47.80	-191.43	-132.56	34.60
6	AEMR	5	-245.09	-134.90	70.22	-248.39	-137.89	55.85
6	AEML	6	-137.29	-131.60	68.73	-139.99	-132.20	57.64
7	ELSA	1	-20.87	-1.63	57.70	-190.87	-155.16	73.60
7	FOR	2	-47.20	-7.70	59.20	-217.13	-162.41	73.00
7	FOL	3	4.38	-6.81	61.30	-165.07	-159.31	77.20
7	MFM	4	-19.41	12.43	43.00	-189.10	-137.90	61.60
7	AEMR	5	-74.70	12.44	59.44	-248.99	-143.88	75.01
7	AEML	6	36.09	14.83	59.44	-133.70	-137.89	79.50
8	ELSA	1	-185.40	-163.23	57.55	-188.77	-154.13	54.25
8	FOR	2	-210.32	-168.05	56.20	-213.46	-159.11	53.50
8	FOL	3	-162.00	-165.65	59.20	-164.73	-156.80	55.30
8	MFM	4	-184.36	-146.00	41.50	-187.57	-135.86	39.10
8	AEMR	5	-239.40	-151.37	57.35	-241.20	-141.19	55.85
8	AEML	6	-133.70	-145.98	61.24	-136.40	-136.99	57.35

9	ELSA	1	-269.84	-279.97	33.10	-189.34	-165.36	71.35
9	FOR	2	-294.42	-285.44	34.30	-213.26	-171.45	72.10
9	FOL	3	-247.37	-284.48	34.60	-166.54	-169.66	73.00
9	MFM	4	-270.90	-264.89	13.90	-189.95	-150.77	52.00
9	AEMR	5	-321.83	-263.71	36.66	-242.40	-151.67	73.21
9	AEML	6	-219.36	-262.51	35.16	-138.79	-145.68	73.81
10	ELSA	1	-24.76	0.23	49.00	-194.13	-155.38	61.30
10	FOR	2	-49.55	-4.27	53.20	-219.01	-161.85	65.20
10	FOL	3	-0.71	-3.80	46.90	-169.34	-159.23	59.80
10	MFM	4	-26.06	14.32	27.70	-196.35	-141.25	40.60
10	AEMR	5	-75.30	17.23	55.55	-248.99	-143.58	67.53
10	AEML	6	31.60	13.04	45.68	-135.50	-139.09	58.56

A.4 SIX-POINT METHOD PLOTS OF CONVERGENCE.

Figure A. 26 through Figure A. 35 show the reduction in the objective function for each of the 6-point tests [1] from section 5.3.3. The objective function is [1]

$$\text{Minimize: } \frac{1}{9} \sum_{i=1}^9 w_{f,i} * f_i + \frac{1}{12} \sum_{j=1}^{12} w_{g,j} * g_j \quad (\text{A-1})$$

where f_i is the primary objective of the optimization, matching the angles and distances between the four main points of the optimization, ELSA, AEMR, AEML, and DFM. $w_{f,i}$ is the weight function applied to primary objectives of the minimization, the weight used in this study is the same weight function validated in [1], as the landmarks used for the optimization are the same as used in [1]. g_j is the secondary objective of the optimization. This consists of matching the angles and distances the main four points make with two secondary points (FOR, FOL). $w_{g,j}$ is the weight function applied to secondary objectives of the minimization, the weight used in this study is the same weight function validated in [1]. A full explanation of the weight functions and the optimization process, including calculating f_i and g_j can be found in [1]. Both the secondary and primary objectives are met by moving the locations of the AEMR, AEML, and DFM. The objective function is minimized using a genetic algorithm to reduce the chance of finding only local minima. The landmarks from T1 are considered the gold-standard, with the T2 landmarks being registered to them.

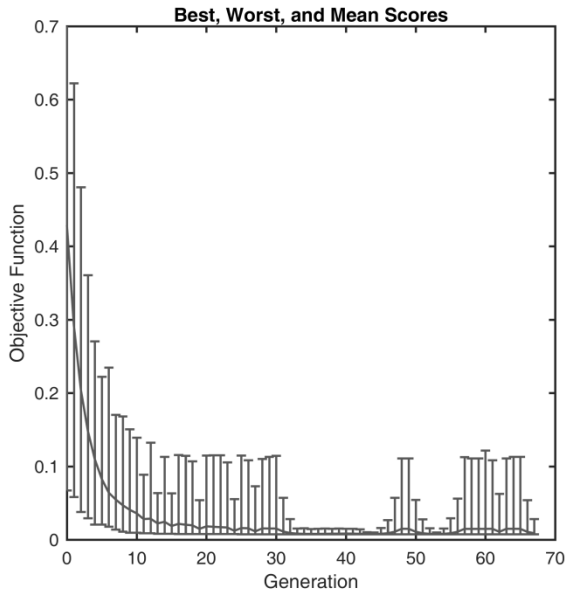


Figure A. 26.Change in objective function with generation of genetic algorithm for test 1 using 6 point method

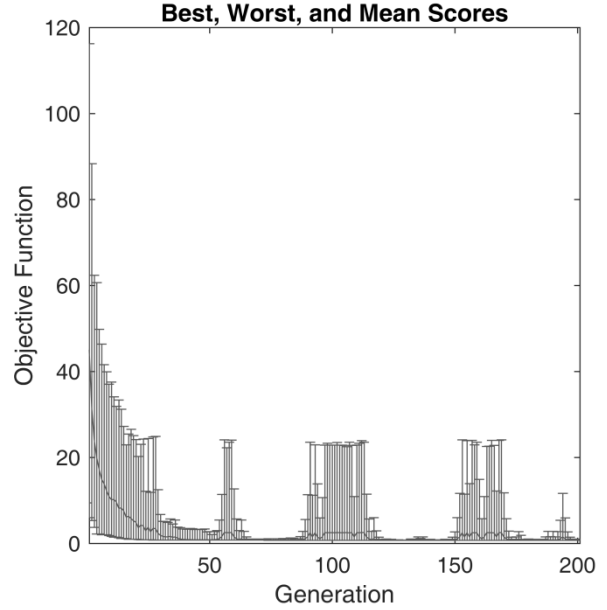


Figure A. 27.Change in objective function with generation of genetic algorithm for test 2 using 6 point method

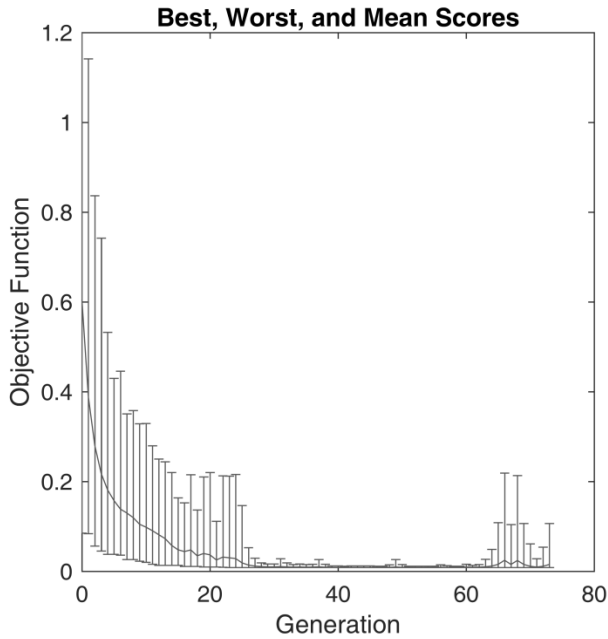


Figure A. 28.Change in objective function with generation of genetic algorithm for test 3 using 6 point method

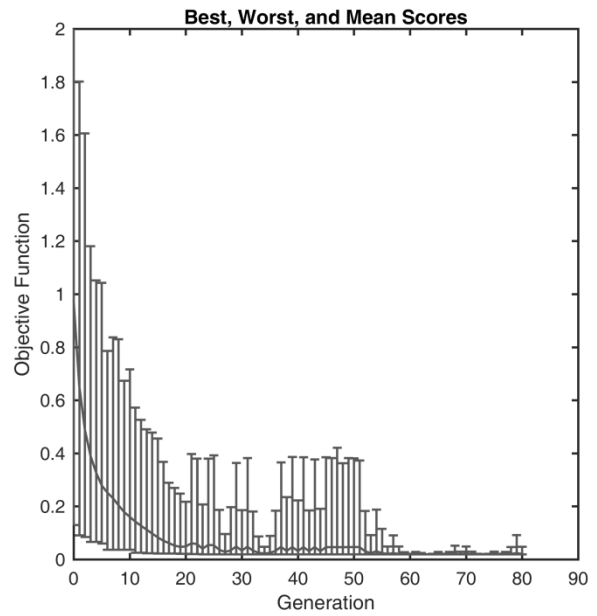


Figure A. 29.Change in objective function with generation of genetic algorithm for test 4 using 6 point method

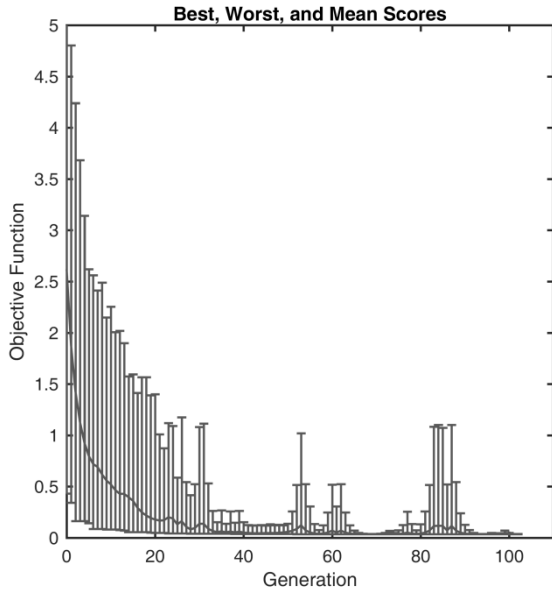


Figure A. 30.Change in objective function with generation of genetic algorithm for test 5 using 6 point method

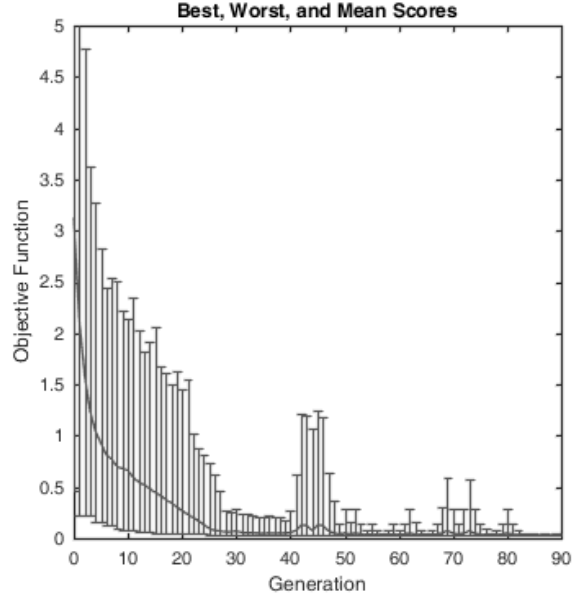


Figure A. 31.Change in objective function with generation of genetic algorithm for test 6 using 6 point method

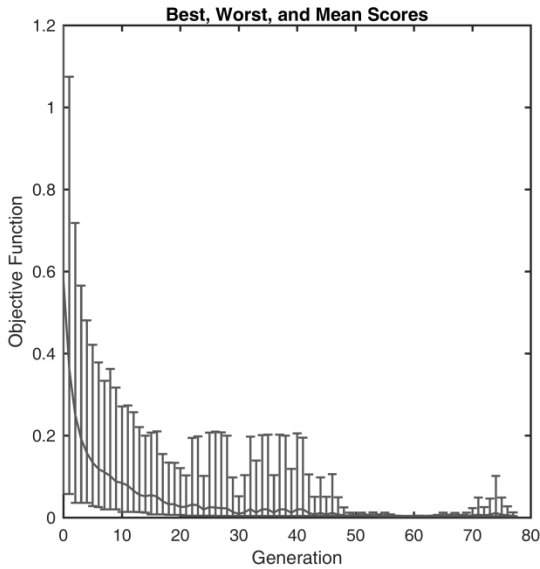


Figure A. 32.Change in objective function with generation of genetic algorithm for test 7 using 6 point method

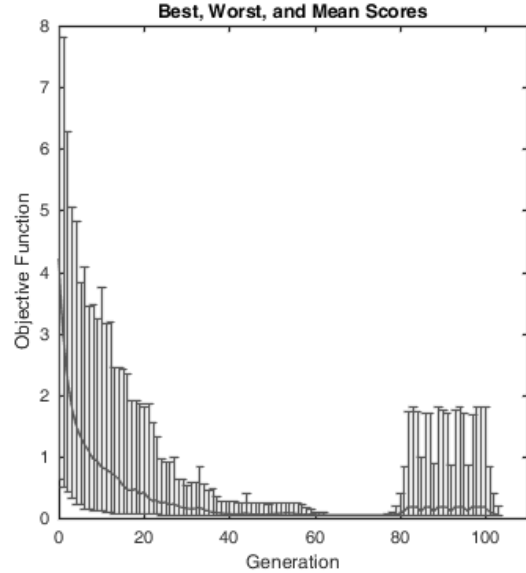


Figure A. 33.Change in objective function with generation of genetic algorithm for test 8 using 6 point method

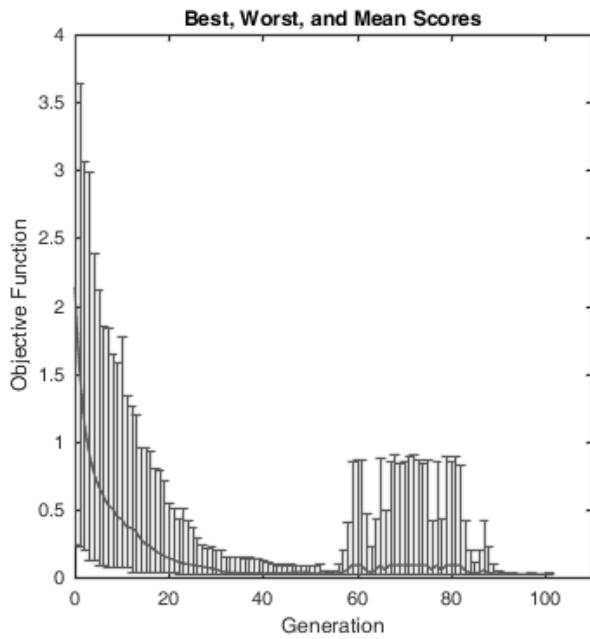


Figure A. 34. Change in objective function with generation of genetic algorithm for test 9 using 6 point method

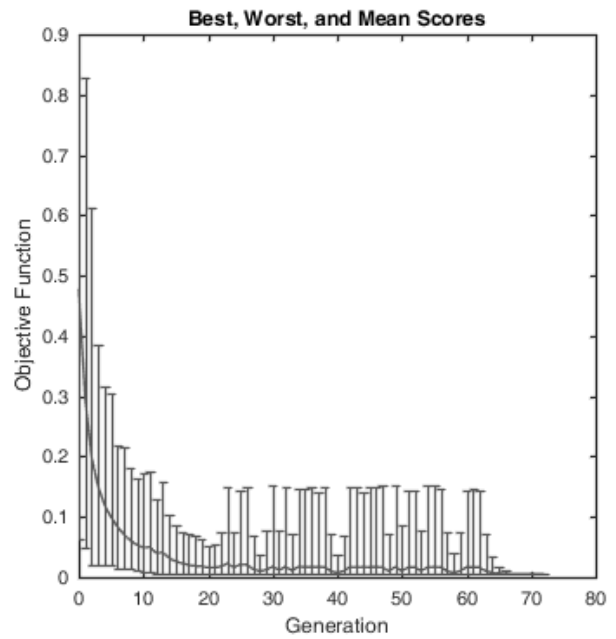


Figure A. 35. Change in objective function with generation of genetic algorithm for test 10 using 6 point method

A.5 LOCATION OF LANDMARKS FROM 6-POINT METHOD FOLLOWING REGISTRATION

Following the 6-point superimposition the new landmark coordinates are output. These landmarks are in the ELSA based coordinate system [2]. The new landmark coordinates are shown in Table A. 3 in mm. The ELSA landmark will always be at location (0, 0, 0) as it is defined as the origin of the coordinate system.

Table A. 3 Post registration coordinates of all the landmarks used in the 6-point optimization

Patient	Landmark Name	Landmark Number	x_1 (mm)	y_1 (mm)	z_1 (mm)	x_2 (mm)	y_2 (mm)	z_2 (mm)
1	ELSA	1	0	0	0	0	0	0
1	FOR	2	-21.51	-3.86	1.84	-20.56	-6.39	0.40
1	FOL	3	22.22	-0.81	2.27	23.07	-0.40	2.50
1	MFM	4	0.00	10.50	-23.83	0.00	10.49	-23.84
1	AEMR	5	-45.69	11.55	0.00	-45.69	11.53	0.00
1	AEML	6	42.77	17.37	0.00	42.74	17.50	0.00
2	ELSA	1	0	0	0	0	0	0
2	FOR	2	-24.55	-4.48	-0.17	-25.12	-4.68	-0.83
2	FOL	3	25.79	-0.43	2.49	25.75	0.14	3.07
2	MFM	4	0.00	13.46	-18.86	0.00	13.46	-18.87
2	AEMR	5	-54.18	15.93	0.00	-54.18	15.95	0.00
2	AEML	6	55.07	19.39	0.00	55.07	19.39	0.00

3	ELSA	1	0	0	0	0	0	0
3	FOR	2	-26.66	-5.82	0.46	-27.52	-7.09	-1.85
3	FOL	3	26.39	-3.12	-0.08	25.87	-3.14	0.32
3	MFM	4	0.00	11.57	-19.71	0.00	11.56	-19.71
3	AEMR	5	-52.82	14.52	0.00	-52.82	14.53	0.00
3	AEML	6	52.27	18.39	0.00	52.28	18.34	0.00
4	ELSA	1	0	0	0	0	0	0
4	FOR	2	-24.57	-9.76	3.98	-24.79	-11.17	3.18
4	FOL	3	27.19	-0.46	2.20	28.45	-1.70	2.15
4	MFM	4	0.00	8.62	-17.69	0.00	8.59	-17.70
4	AEMR	5	-56.75	8.30	0.00	-56.75	8.20	0.00
4	AEML	6	48.34	27.50	0.00	48.32	27.51	0.00
5	ELSA	1	0	0	0	0	0	0
5	FOR	2	-21.98	-8.25	1.30	-22.23	-9.08	1.03
5	FOL	3	25.28	1.46	3.13	25.70	0.91	3.53
5	MFM	4	0.00	11.66	-17.59	0.00	11.64	-17.59
5	AEMR	5	-52.53	9.73	0.00	-52.53	9.70	0.00
5	AEML	6	49.97	28.73	0.00	49.97	28.73	0.00

6	ELSA	1	0	0	0	0	0	0
6	FOR	2	-22.38	-10.75	0.35	-22.69	-10.42	-0.34
6	FOL	3	26.12	-1.17	2.56	25.46	-0.51	2.93
6	MFM	4	0.00	10.83	-21.37	0.00	10.85	-21.36
6	AEMR	5	-54.59	5.57	0.00	-54.59	5.66	0.00
6	AEML	6	51.84	23.07	0.00	51.87	23.02	0.00
7	ELSA	1	0	0	0	0	0	0
7	FOR	2	-25.42	-9.02	2.12	-25.60	-9.31	1.00
7	FOL	3	25.63	-1.63	4.23	26.12	-1.66	3.31
7	MFM	4	0.00	12.38	-16.20	0.00	12.38	-16.20
7	AEMR	5	-55.15	7.52	0.00	-55.15	7.53	0.00
7	AEML	6	54.53	23.35	0.00	54.53	23.39	0.00
8	ELSA	1	0	0	0	0	0	0
8	FOR	2	-24.75	-5.77	0.00	-24.59	-5.54	0.47
8	FOL	3	23.51	-1.42	1.22	24.11	-2.10	0.17
8	MFM	4	0.00	15.17	-18.04	0.00	15.16	-18.04
8	AEMR	5	-54.38	9.95	0.00	-54.38	9.94	0.00
8	AEML	6	51.12	19.27	0.00	51.12	19.28	0.00

9	ELSA	1	0	0	0	0	0	0
9	FOR	2	-24.88	-3.69	1.68	-24.35	-3.80	1.70
9	FOL	3	22.13	-5.56	2.58	22.35	-6.29	1.36
9	MFM	4	0.00	11.75	-21.42	0.00	11.76	-21.42
9	AEMR	5	-50.89	19.76	0.00	-50.90	19.71	0.00
9	AEML	6	51.46	14.45	0.00	51.45	14.47	0.00
10	ELSA	1	0	0	0	0	0	0
10	FOR	2	-24.82	-5.47	2.57	-25.17	-6.45	1.06
10	FOL	3	24.32	-2.79	0.50	24.80	-4.02	0.50
10	MFM	4	0.00	11.35	-22.91	0.00	11.34	-22.92
10	AEMR	5	-51.70	14.56	0.00	-51.70	14.53	0.00
10	AEML	6	55.73	15.72	0.00	55.73	15.69	0.00

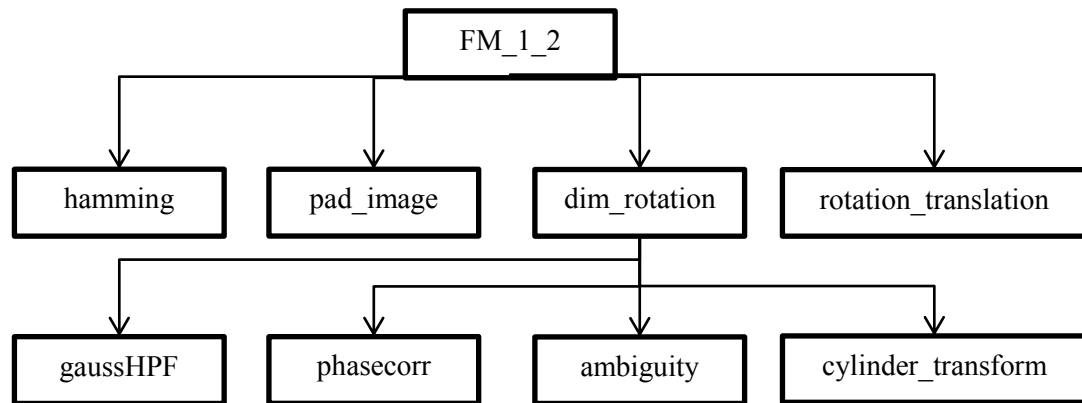
A.6 REFERENCES

- [1] A. DeCesare, M. Secanell, M. O. Lagravère, and J. Carey, “Multiobjective optimization framework for landmark measurement error correction in three-dimensional cephalometric tomography,” *Dento Maxillo Facial Radiol.*, vol. 42, no. 7, p. 20130035, 2013.

- [2] M. O. Lagravère, P. W. Major, and J. Carey, “Sensitivity analysis for plane orientation in three-dimensional cephalometric analysis based on superimposition of serial cone beam computed tomography images,” *Dentomaxillofacial Radiol.*, vol. 39, no. 7, pp. 400–408, Oct. 2010.

Appendix B – Matlab Code of Superimposition Method

The code is programmed in the Matlab language. The figure below is a flow chart of the code showing dependencies. Any function shown is dependant and requires the functions under it links to.



B.1 - FM_1_2 Function

```
function [FinalV2, total_rotation] = FM_1_2(V1,V2)
%FM_1_1 Rev 1.2 of 3D Fourier Mellin
% Read in two volumes then outputs the 2nd volume registered to the first
% The update to revision one applies the mask only to the unpadded
% section of the image. This should increase the accuracy of the
% results. The strength of the filter is set to 80 as found is best for
% cranial bases. The second iteration (.2) updates the translation to no
% longer be performed using circshift but instead has the rotation
% performed using the tform array, then a second phasecorr is performed
% that will correct for any extra changes

%TO-DO
%-----
%-----

tic;
%%Main
%create the mask
pad_size = size(V1); %this is the size you want the matrix padded too
V1_orig = (single(V1));
V1 = V1_orig;
V2_orig = ((single(V2))); %Save a copy of the second image for below
V2 = V2_orig;
mask_V1 = hamming(V1); %This creates the masks for the images
mask_V2 = hamming(V2);
V1 = V1.*mask_V1;
V2 = V2.*mask_V2;
V2_orig = pad_image(V2_orig,pad_size);
V2_orig_mask = pad_image(mask_V2,pad_size);
V2 = pad_image(V2,pad_size);
rot_storage = [1 1 1];
iter = 1;
while norm(rot_storage) > 0
    if iter == 7;
        break;
    end
    disp(['iteration ' num2str(iter)]);
    for i = 0:2
        if i > 0
            V1 = shiftdim(V1,1);
            V2 = shiftdim(V2,1);
        end
        angle = dim_rotation((V1), (V2));
        V2 = rotation_translation(V2,angle,[0 0 0]);
        rot_storage(i+1)= angle;
        if i == 2
            V1 = shiftdim(V1,1);
            V2 = shiftdim(V2,1);
        end
    end
end

disp(['Rotations (x,y,z) are: ' ...
    num2str(rot_storage(2)) ', ' ...
    num2str(rot_storage(3)) ', ' ...
    num2str(rot_storage(1))])
```

```

    % All the rotations will now be saved in order to apply later
    iter_rotation(:, :, iter) = [1 0 0 0; 0 1 0 0; 0 0 1 0; -size(V2,2)/2 -size(V2,1)/2 -size(V
2,3)/2 1]* ...
        [cosd(rot_storage(1)) -sind(rot_storage(1)) 0 0; sind(rot_storage(1)) cosd(rot_storag
e(1)) 0 0; 0 0 1 0; 0 0 0 1]* ...
        [1 0 0 0; 0 cosd(rot_storage(2)) -sind(rot_storage(2)) 0; 0 sind(rot_storage(2)) cosd
(rot_storage(2)) 0; 0 0 0 1]* ...
        [cosd(rot_storage(3)) 0 sind(rot_storage(3)) 0; 0 1 0 0; -sind(rot_storage(3)) 0 cosd
(rot_storage(3)) 0; 0 0 0 1]* ...
        [1 0 0 0; 0 1 0 0; 0 0 1 0; size(V2,2)/2 size(V2,1)/2 size(V2,3)/2 1];

    iter = iter + 1;

end
%Before we do the tranlation step we will do all the rotations in a single
%step to reduce rotation errors
total_rotation = [1 0 0 0; 0 1 0 0; 0 0 1 0; 0 0 0 1];
for i = 1:iter-1
    total_rotation = total_rotation*iter_rotation(:, :, i);
end
%Perform the final rotation in one go in order to reduce errors
tform = maketform('affine', total_rotation);
R = makesampler('linear', 'replicate');
V2 = tformarray(V2_orig.*V2_orig_mask, tform, R, [1 2 3], [1 2 3], size(V2_orig), [], []);

[dim1_trans, dim2_trans, dim3_trans, str] = phasecorr(ifftn(ifftshift(gaussHPF(fftshift(fftn(V1_
orig.*mask_V1))))), ...
    ifftn(ifftshift(gaussHPF(fftshift(fftn(V2))))));
disp(str);
% make sure if the translations are above half size of the image it turns
% into a -translation
if dim1_trans >= size(V2_orig,1)/2
    dim1_trans = dim1_trans-257;
end
if dim2_trans >= size(V2_orig,2)/2
    dim2_trans = dim2_trans-257;
end
if dim3_trans >= size(V2_orig,3)/2
    dim3_trans = dim3_trans-257;
end

disp(['Translations 1 (x,y,z) are: ' ...
    num2str(dim2_trans) ', ' ...
    num2str(dim1_trans) ', ' ...
    num2str(dim3_trans)])

% update total rotation to include the translations
total_rotation = total_rotation * ...
    [1 0 0 0; 0 1 0 0; 0 0 1 0; dim1_trans dim2_trans dim3_trans 1];
% perform the rotations AND translations to the original in one step
tform = maketform('affine', total_rotation);
V2 = tformarray(V2_orig.*V2_orig_mask, tform, R, [1 2 3], [1 2 3], size(V2_orig), [], []);

% check the phase corr again to see if any more rotations need to be done

```

```

% this does not need to be iterated rather it is just a single check
[dim1_trans,dim2_trans,dim3_trans,str] = phasecorr(ifftn(iffshift(gaussHPF(fftshift(fft(V1_
orig.*mask_V1))))), ...
    ifftn(iffshift(gaussHPF(fftshift(fft(V2))))));
disp(str);
if dim1_trans >= size(V2_orig,1)/2
    dim1_trans = dim1_trans-257;
end
if dim2_trans >= size(V2_orig,2)/2
    dim2_trans = dim2_trans-257;
end
if dim3_trans >= size(V2_orig,3)/2
    dim3_trans = dim3_trans-257;
end
disp(['Translations 2 (x,y,z) are: ' ...
    num2str(dim2_trans) ', ' ...
    num2str(dim1_trans) ', ' ...
    num2str(dim3_trans)])

if (dim1_trans^2+dim2_trans^2+dim3_trans^2) > 0
    total_rotation = total_rotation * ...
        [1 0 0 0;0 1 0 0; 0 0 1 0; dim1_trans dim2_trans dim3_trans 1];
    tform = maketform('affine',total_rotation);
    FinalV2 = tformarray(V2_orig, tform, R, [1 2 3], [1 2 3], size(V2_orig), [], []);
else
    FinalV2 = V2;
end

%D3Visualizer(V1_orig,FinalV2)
%Take the L2 norm
if iter >=7
    L2_norm = -1;
else
    V1_orig(FinalV2 == 0) = 0;
    L2_norm = sum(sum(sum((FinalV2-V1_orig).^2)))
end

toc

```

B.2 - hamming Function

```
function mask = hamming(V1)
imSize_i = size(V1,1);
imSize_j = size(V1,2);
imSize_k = size(V1,3);
alpha = 0.53836;
beta = 0.46164;
n_i = 1:imSize_i;
n_j = 1:imSize_j;
n_k = 1:imSize_k;
w_i = alpha - beta*cos(2*pi*n_i/(imSize_i-1));
w_j = alpha - beta*cos(2*pi*n_j/(imSize_j-1));
w_k = alpha - beta*cos(2*pi*n_k/(imSize_k-1));
mask = zeros(size(V1));
for i = 1:imSize_i
    for j = 1:imSize_j
        for k = 1:imSize_k
            mask(i,j,k) = w_i(i).*w_j(j).*w_k(k);
        end
    end
end
```

B.3 - pad_image Function

```
function [V_Padded] = pad_image(V,pad_size)
%pad_image(V,pad_size) Pads 3D array V to pad_size x pad_size x pad_size
% The image is padded and must be a 3d array. Will error if any of the
% dimensions of V are larger than padsize

%make sure the padding is larger than the original image
size_V = size(V);

%pad the image
padding = floor((pad_size-size_V)/2);
V_Padded = padarray(V,padding);

if ndims(V_Padded) == 3
    %check for any dimensions being pad_size -1
    for i = 1:3
        switch i
            case 1
                if size(V_Padded,1) == pad_size(1)-1
                    V_Padded(pad_size(1),:,:) = 0;
                end
            case 2
                if size(V_Padded,2) == pad_size(2)-1
                    V_Padded(:,pad_size(2),:) = 0;
                end
            case 3
                if size(V_Padded,3) == pad_size(3)-1
                    V_Padded(:,:,pad_size(3)) = 0;
                end
            end
        end
    end

elseif ismatrix(V_Padded) == 1
    for i = 1:2
        switch i
            case 1
                if size(V_Padded,1) == pad_size(1)-1
                    V_Padded(pad_size(1),:,:) = 0;
                end
            case 2
                if size(V_Padded,2) == pad_size(2)-1
                    V_Padded(:,pad_size(2),:) = 0;
                end
            end
        end
    end
else
    error('Error in pad_image function, image to be padded is not 2 or 3 dimension');
end
```

B.4 - dim_rotation Function

```
function theta = dim_rotation(V1,V2)
%theta = dim_rotation(V1,V2)
%Returns Angle of diffence, z direction
% dim_rotation returns the angle of difference between two objects about
% the z-axis using Fourier transforms and cylindrical transforms

%Take the FFT
V1_fft = fftshift(fftn(V1));
V2_fft = fftshift(fftn(V2));

%apply a Gaussian Hi-pass filter to the images
V1_fft_filter = gaussHPF(abs(V1_fft));
V2_fft_filter = gaussHPF(abs(V2_fft));

%Perform a cylindrical coordinate conversion
V1cylinder = cylinder_transform(V1_fft_filter);
V2cylinder = cylinder_transform(V2_fft_filter);

%Phasecorr time
[~,thetashift,~,~] = phasecorr((V1cylinder),(V2cylinder));
theta = (thetashift)*(360)/size(V1cylinder,1);

%Ambiguity Check
theta = ambiguity(theta);
```

B.5 - gaussHPF Function

```
function V_filtered = gaussHPF(image)
%This is the hi-pass filter function, it is a gaussian filter
if ndims(image) == 3
    M = size(image,2);
    N = size(image,1);
    P = size(image,3);
    u = (0:(M-1));
    v = (0:(N-1));
    w = (0:(P-1));
    idx = find(u > M/2);
    u(idx) = u(idx) - M;
    idy = find(v > N/2);
    v(idy) = v(idy) - N;
    idz = find(w > P/2);
    w(idz) = w(idz)-P;
    [U,V,W] = meshgrid(u,v,w);
    D = sqrt(U.^2 + V.^2 + W.^2);
    H = fftshift(1-exp(-(D.^2)./(2*(80^2))));
    V_filtered = H.*(image);
elseif ismatrix(image) == 1
    M = size(image,2);
    N = size(image,1);
    u = (0:(M-1));
    v = (0:(N-1));
    idx = find(u > M/2);
    u(idx) = u(idx) - M;
    idy = find(v > N/2);
    v(idy) = v(idy) - N;
    [U,V] = meshgrid(u,v);
    D = sqrt(U.^2 + V.^2);
    H = fftshift(1-exp(-(D.^2)./(2*(80^2))));
    V_filtered = H.*(image);
else
    error('image sent to gaussHPF is not 2D or 3D')
end
```

B.6 - cylinder_transform Function

```
function V_cylinder = cylinder_transform(V)
%Converts a cartesian volume to cylindrical
% The input is a 3D image. The output is the 3D image in cylindrical
% Output Dim1 is r, Dim2 is theta, dim3 is z
if ndims(V) == 3
    u = size(V,1);
    theta = linspace(0,2*pi,u+1); theta(end) = []; %remove last element of theta last bracket
    is theta <= 2pi
    z = linspace(0,u-1,u); %physics representation therefor phi is azimuth (within xy plane)
    d = u - ceil(u/2)-1; %In case of an even size matrix far right coloum plane, bottom row
    plane, back plane are ignored
    rho = linspace(0,d,u);

    %The new cylindrical coordinate system we have just defined now needs to have a
    %cartesian representation
    [theta,rho,z] = meshgrid(theta,rho,z);
    [xx,yy,zz] = pol2cart(theta,rho,z); %phi is azimuth (i.e. in xy plane)
    %center the new coordinate setup
    lxx = xx+u/2;
    lyy = yy+u/2;
    V_cylinder = interp3(V,lxx,lyy,zz,'linear',0);

elseif ismatrix(V) == 1
    u = size(V,1);
    theta = linspace(0,2*pi,u+1); theta(end) = []; %remove last element of theta last bracket
    is theta <= 2pi
    d = u - ceil(u/2)-1; %In the case of an even size matrix far right coloum plane, bottom r
    ow plane are ignored
    rho = linspace(0,d,u);
    [theta,rho] = meshgrid(theta,rho);
    [xx,yy] = pol2cart(theta,rho); %phi is azimuth (i.e. in xy plane)
    %center the new coordinate setup
    lxx = xx+u/2;
    lyy = yy+u/2;
    V_cylinder = interp2(V,lxx,lyy,'linear',0);
else
    error('Input to cylinder transform is not 2D or 3D');
end
```

B.7 - phase_corr Function

```
function [dim1_shift,dim2_shift,dim3_shift,maxval] = phasecorr(ga,gb)
%Performs phase correlation to find shift
% Inputs are two volumes, outputs are shifts in 3 directions
% Already accounts for index 1 Matlab
% Output is amount that b must shift to reach a
% Method assumes that the shift is a circularshift
Ga = (fftshift(fftn(ga)))+1;
Gb = (fftshift(fftn(gb)))+1;
R = (Ga.*conj(Gb))./(abs(Ga.*conj(Gb)));
if ndims(ga) == 3
    r = ifftn(R);
    [maxval,ind] = max(abs(r(:)));
    [dim1shift,dim2shift,dim3shift] = ind2sub(size(r),ind);
    dim1_shift = (dim1shift-1);
    dim2_shift = (dim2shift-1);
    dim3_shift = (dim3shift-1);

elseif ismatrix(ga)==1
    r = ifftn(R,size(R).*4);
    [maxval,ind] = max(abs(r(:)));
    [dim1shift,dim2shift,dim3shift] = ind2sub(size(r),ind);
    dim1_shift = (dim1shift-1)/2;
    dim2_shift = (dim2shift-1)/2;
    dim3_shift = (dim3shift-1)/2;

else
    error('Error input to phasecor function is neither 2D or 3D');
end
```

B.8 - ambiguity Function

```
function [theta] = ambiguity(theta)
%ambiguity Returns proper rotation angle
% Input arguments are the "gold standard" the, the image to be
% registered, and the angle of rotation found using phase correlation.
% Due to the nature of phase correlation the angle of rotation found
% could be shifted by 180 degrees. Thisfunction tests to find rather the
% found angle or the 180 shifted angle gives the proper registration.

%Take the angle find and subtract 90 intul it lies between -15 and 15
%degrees then do an ambiguity check on it.

%lets get theta to be +-15 degrees
%VESTIGIAL CODE-----
% iter = 1;
% while (sign(theta) == 1) && (theta > 45) && (iter <= 5)
%
%     theta = theta - 90;
%     iter = iter+1;
% end
% iter = 1;
% while (sign(theta) == -1) && (theta < -45) && (iter <= 5)
%
%     theta = theta + 90;
%     iter = iter+1;
% end
%-----

if (theta > 165) && (theta <195)
    theta = theta-180;
elseif (theta < 105) && (theta > 75)
    theta = theta - 90;
elseif (theta < 15) || (theta > 345)
else theta = 0;
end
```

B.9 - rotation_translation Function

```
function V2 = rotation_translation(V2,rotation,trans)
%V2 = rotation_translation(V2,rotation,trans)
%Rotates and Translates a Volume
% The function takes an input of a volume, angle and translation
% Rotates about center of image about z-axis
% Translates the amount listed trans

%First step is to translate center to origin
T1 = [1 0 0 0; 0 1 0 0; 0 0 1 0; -size(V2,2)/2 -size(V2,1)/2 -size(V2,3)/2 1];
%create all the matrices for rotations about x,y,z

%rotate about x
T_rot = [cosd(rotation) -sind(rotation) 0 0; ...
         sind(rotation) cosd(rotation) 0 0; ...
         0 0 1 0; ...
         0 0 0 1];

%Return center to center of image
T2 = [1 0 0 0; 0 1 0 0; 0 0 1 0; size(V2,2)/2 size(V2,1)/2 size(V2,3)/2 1];
Ttrans = [1 0 0 0; 0 1 0 0; 0 0 1 0; 0 0 0 1];
%create the resampler and interpolator structures
tform = maketform('affine',T1*T_rot*T2*Ttrans);
R = makesampler('linear', 'replicate');
V2 = tformarray(V2, tform, R, [1 2 3], [1 2 3], size(V2), [], []);
for i=1:3
V2 = circshift(V2,trans(i),i);
end
```